Carbon Nanotube Based Electrochemical Supercapacitors

A Dissertation
Presented to
The Academic Faculty

By

Chongfu Zhou

In Partial Fulfillment
of the Requirements for the Degree
Doctor of Philosophy in the
School of Polymer, Textile and Fiber Engineering

Georgia Institute of Technology

December, 2006

Carbon Nanotube Based Eelectrochemical Supercapacitors

Approved by:

Dr. Satish Kumar, Advisor
School of Polymer, Textile, and Fiber Engineering
Georgia Institute of Technology

Dr. Lawrence A. Bottomley
School of Chemistry and Biochemistry
Georgia Institute of Technology

Dr. W. Brent Carter
School of Materials Science and Engineering
Georgia Institute of Technology

Dr. Fred L. Cook
School of Polymer, Textile, and Fiber Engineering
Georgia Institute of Technology

Dr. William J. Koros
School of Chemical and Biomolecular Engineering
Georgia Institute of Technology

Date approved: July 28, 2006

ACKNOWLEDGEMENTS

I would like to express my deep and sincere gratitude to many people who made this PhD thesis possible. Special thanks are due to my supervisor Professor Satish Kumar for his insight resolving many of the problems encountered throughout research and thesis writing, for his inspiring and encouraging way to guide me to a deeper understanding of research, and his invaluable comments during my graduate study.

I am highly indebted to my committee members Professors Lawrence A. Bottomley, W. Brent Carter, Fred L. Cook, and William J. Koros. Many thanks are due to Dr. Runqing Ou, Dr. Tao Liu, Dr. James M. Tour, Dr. Wallace W. Carr, Dr. Hongming Dong and my group members.

I also owe my loving thanks to my grandparents, my parents, my uncle, my aunts, my sisters and my wife. They have lost a lot due to my research abroad. Without their encouragement and understanding it would have been impossible for me to finish this work.

TABLE OF CONTENTS

LIST OF TABLES

LIST OF FIGURES

SUMMARY

Several approaches have been used to develop carbon nanotube (CNT) based electrochemical supercapacitors. These approaches include the following: (a) stabilization and carbonization of ternary composites of polyacrylonitrile (PAN), poly (styrene–co-acrylonitrile) (SAN) copolymer, and single wall carbon nanotubes (SWNTs); (b) SWNT membranes functionalized with aryl chloride, sodium sulfonate, aryl sulfonic acid, bis(3,5-di-tert-butylphenyl)5-aminobenzene-1,3-dioate, and 4,4'-methylenedianiline; and (c) pyrrole treated SWNTs. In addition nitric acid functionalized and heat-treated SWNT membranes have been studied. The electrochemical supercapacitor behavior of these membrane electrodes has been characterized by cyclic voltammetry, constant current charging-discharging, and impedance analysis in aqueous and ionic liquid electrolytes. Long term performance of selected electrodes has been evaluated. The surface area and pore size distribution was quantified by N_2 gas adsorption/desorption and correlated with capacitance performance. The surface functional groups have been characterized by X-ray photoelectron spectroscopy. CNT electrode/electrolyte interaction has been characterized using contact angle measurements. Electrolyte absorption by the electrodes has also been characterized.

Carbonized PAN/SAN/SWNT ternary composites exhibit double layer capacity of over 200 $\mu F/cm^2$. By comparison, the double layer capacity of classical meso-porous carbons is in the range of 10-50 $\mu F/cm^2$. The capacitance of functionalized SWNTs is up to 2 times that of the control bucky paper made from unfunctionalized SWNTs.

Energy density of functionalized electrodes when evaluated in an ionic liquid is as high as 28 kJ/kg. High capacitance (up to 350 F/g) was obtained for pyrrole-treated functionalized SWNT membranes in 6 M KOH. This value is almost seven times that of the control bucky paper. Correlating the capacitance with surface area and pore size distribution, it was observed that macropores (pore width greater than 50 nm) play an important role for achieving high capacitance.

CHAPTER 1

INTRODUCTION

1.1 Historical Background

Supercapacitor, also known as electrical double layer capacitor, ultracapacitor, or electrochemical capacitor, is an electrical energy storage device. The first patent on supercapacitor was granted to Becker at General Electric Corp. in 1957,[1] in which he proposed a capacitor based on porous carbon material with high surface area. In 1969, SOHIO first attempted to market such energy storage device using high surface area carbon materials with tetraalkylammonium salt electrolyte.[2] In late 70's and 80's, Conway and coworkers made a great contribution to the capacitor research work based on RuO_2, which has high specific capacitance and low internal resistance.[3] In the 90's, supercapacitors received much attention in the context of hybrid electric vehicles. Large numbers of supercapacitor patents have been granted as cited by Sarangapani in 1996.[4] All these studies triggered U.S. Department of Energy to initiate a 1998-2003 short-term and an after-2003 long-term supercapacitor development programs.[5]

Commercial productions of electrochemical supercapacitors in the current markets are based on the high surface area porous carbon materials as well as based on noble metal dioxide systems.[6] For example, Matsushita Electric Industrial (Panansonic, Japan) developed Gold capacitors,[6] and Pinnacle Research (USA)[6] especially made high performance supercapacitors for military applications. These

commercial supercapacitors are widely used as power sources for activators,[6] or as elements for long time constant circuits,[6] or standby power for random access memory devices, and telephone equipments, etc. A comparison of the properties and performance between battery, capacitor, and supercapacitor is given in Table 1.1.

Table 1.1. Comparison of Capacitor, Supercapacitor and Battery[7]

Parameters	**Capacitor**	**Supercapacitor**	**Battery**
Charge Time	10^{-6} ~ 10^{-3} sec	1 ~ 30 sec	0.3 ~ 3 hrs
Discharge Time	10^{-6} ~ 10^{-3} sec	1 ~ 30 sec	1 ~ 5 hrs
Energy Density (Wh/kg)	< 0.1	1 ~ 10	20 ~ 100
Power Density (W/kg)	> 10,000	1,000 ~ 2,000	50 ~ 200
Cycle Life	> 500,000	> 100,000	500 ~ 2,000
Charge/Discharge Efficiency	~ 1.0	0.90 ~ 0.95	0.7 ~ 0.85

Batteries are typically low power devices compared to capacitors, which have power densities as high as 10^6 W/kg, but low energy densities. From this point of view, supercapacitors combine the properties of high power density and higher energy density, and also have long life cycles due to the absence of chemical reactions. A comprehensive review of the historical background, properties, and principles of capacitors has been given by Conway.[6]

1.2 Principle of Supercapacitor

Supercapacitors have two electrodes immersed in an electrolyte solution, with one separator between them, and two current collectors. The process of energy storage is associated with buildup and separation of electrical charge accumulated on two conducting plates spaced some distance apart as shown in Figure 1.1.

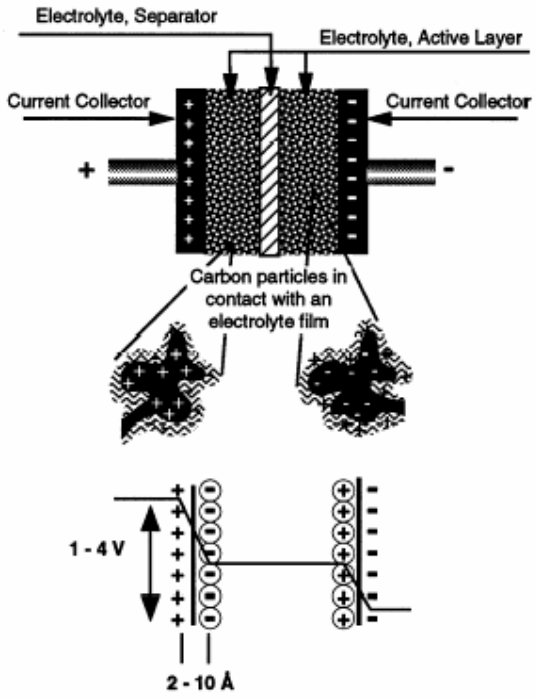

Figure 1.1. Schematic diagram of mechanism of electric double layer capacitor and illustration of the potential drop at interface of electrolyte and electrode.[8]

In a plane capacitor with a pair of plates of equal area, A, in parallel configuration and separated by a distance, d, in vacuum, the capacitance, C, is given by equation (1).

$$C = \frac{A}{4\pi d} \tag{1}$$

If the plates are separated by a dielectric medium, ε , the capacitance is given by equation (2).

$$C = \frac{A\varepsilon}{4\pi d} \tag{2}$$

Electrical double layer capacitor stores energy in the similar way, but the charge does not accumulate on two conductors separated by a dielectric. Instead, the charge accumulates in the electric double layer at the interface between the surface of a conductor and an electrolyte solution. When charged, the negative ions in the electrolytes will diffuse to the positive electrode, while the positive ions will diffuse to the negative electrodes. In this case, it creates two separate layers of capacitive storage, so the maximum energy density, *W*, stored in the capacitor is given by equation (3).

$$W = \frac{1}{2}CV^2 \tag{3}$$

where *C* is the specific capacitance, and *V* is voltage.

The double layer capacitor does not involve chemical reactions, thus supercapacitors have long life cycles of charge and discharge. Besides the capacitance contribution from the separation of charge in the double layer, capacitance associated with reactions on the surface of the electrode, are also important. During these reactions, electron transfer does take place across the double layer, with consequence of oxidation state change. Thus the capacitance from the faradaic process is referred to as pseudocapacitance. Detailed discussion about the fundamental differences between double-layer capacitance and pseudocapacitance is given in the following paragraphs.

1.2.1 Electrical Double Layer[9]

Electrical double layer results from strong interactions between the ions/molecules in the solution and the electrode surface. At a metal-solution interface, there is a thin layer of charge on the metal surface, which results from an excess or deficiency of electrons. On the other hand, in the vicinity of the electrode surface, there is an opposite charge in solution due to an excess of either cations or anions. Thus the electrical double layer is made up of the whole array of charged species and oriented dipoles existing at the metal-solution interface.[9] The double layer capacitance is generally a function of potential, which is different from a standard capacitor. Several models, such as Helmholtz model,[10] Gouy-Chapman model,[11] and Gouy-Chapman-Stern model,[12] and Grahame model[13] have been proposed to explain the behavior observed for electrodes under potentiostatic control in solution.

The electrical double layer can be characterized by several layers as shown in Figure 1.2a.[9] The inner layer closest to the electrode, also called compact, Helmholtz, or Stern layer, consists of the solvent molecules and sometimes other specifically adsorbed ions or molecules. The inner layer can be divided into inner Helmholtz plane (IHP) and outer Helmholtz plane (OHP). The IHP is at a distance x_1, where the electrical centers of the specifically adsorbed ions are located, while the OHP is at a distance x_2, which represents the closest distance that the solvated ions can approach metal or starting point of diffuse layer. These solvated ions are nonspecifically adsorbed since the interaction between the solvated ions and charged metals involves

only long-range electrostatic forces, and is not dependent on the chemical properties of the ions.

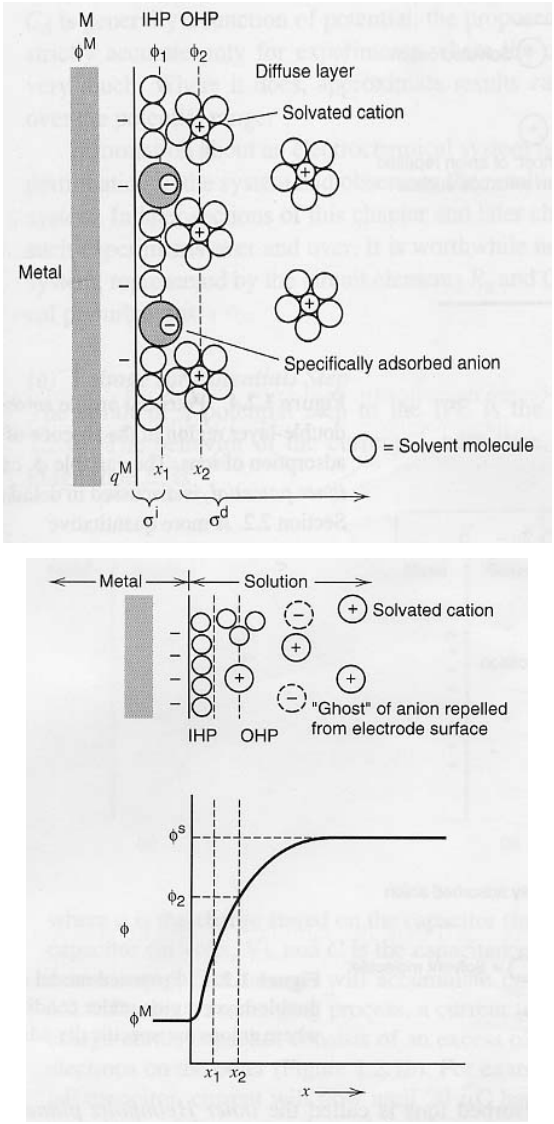

Figure 1.2. (a) Proposed model of the double layer region under conditions where anions are specifically adsorbed. (b) Potential profile across the double layer region in the absence of specific adsorption of ions. In the figure, IHP is inner Helmholtz plane, OHP is outer Helmholtz plane, M metal, Φ_2 potential at the OHP with respect to bulk solution, Φ_1 potential at IHP, Φ^M the electrostatic potential of metal, Φ^S the electrostatic potential of solution, q^M charge on the metal electrode, χ_1 the distance of IHP from metal, χ_2 the distance of OHP from metal, σ^i the total charge density in the inner layer, σ^d the excess charge density in the diffuse layer. [9]

Due to thermal agitation of the solution, the nonspecifically adsorbed ions are distributed from the OHP into the bulk of the solution and form a three dimensional diffuse layer, whose thickness is determined by the total ionic concentration in the solution. In a double layer, the total charge density on the solution is made up of the total charge density from specifically adsorbed ions in the inner layer, and the total excess charge density in the diffuse layer.[9] Hence the capacitance of the double layer includes Helmholtz type compact double layer capacitance C_H and diffuse region of the double layer capacitance C_{diff}, and the total double layer capacitance is given by equation (4).[3]

$$\frac{1}{C_{dl}} = \frac{1}{C_H} + \frac{1}{C_{diff}} \tag{4}$$

The potential in these two layers is much different, and a potential profile of the double layer is shown in Figure 1.2b. The electrical double layer can be affected by many factors, such as the structure of the electrodes and electrolyte. A substantial amount of work has been reported on the graphite carbon electrodes.[14,15,16,17,18,19,20,21]

1.2.2 Pseudocapacitance

Pseudocapacitance is faradaic in origin, and quite different from the classical electrostatic capacitance observed in the double layer. In the case of the pseudocapacitance, charge will transfer across the double layer, similar to discharging and charging in a battery, thus the capacitance can be calculated by using the extent of charge stored (Δq) and the change of the potential (ΔV). The relationship between them can be described by equation (5).

$$C = \frac{\partial(\Delta q)}{\partial(\Delta V)} \tag{5}$$

Generally in a double layer carbon capacitor, there is about 1-5% pseudocapacitance due to the functional groups on the surface, but there is also about 5-10% double layer capacitance in a battery.[6] Pseudocapacitance can be caused by electrosorption of H or metal atoms, and redox reactions of electroactive species, which strongly rely on the chemical affinity of the surface to ions in the electrolyte. On the one hand, pseudocapacitance can remarkably enhance the capacitance of supercapacitors, on the other hand, it also deteriorates other properties, such as life cycle. Several types of materials with significant pseudocapacitance behavior have been investigated:[6] 1) electroactive oxide or hydrous oxide films of transition metals, such as MnO_2, IrO_2, RuO_2, MoO_3, WO_3, Co_3O_4; 2) films of conductiving polymers, e.g. polypyrrole, polythiophene, polyaniline, and their derivatives; 3) electrosorbed H at Pt metals.

1.3 Types of Supercapacitor

In terms of the chemical composition, several types of supercapacitor electrode materials have been investigated intensively, which include electrically conducting metal oxides, e.g., RuO_2,[22] IrO_2,[23] MnO_2,[24] conducting polymers, e.g., polythiophene,[25,26,27,28] polypyrrole,[29] polyaniline (PANI)[30,31,32] and their derivatives, and different type of carbon materials, e.g., carbon aerogel,[33] activated carbon,[34] and carbon nanotubes.[35,36,37]

1.3.1 Carbon Based Supercapacitor

Carbon is the most common and economical material for supercapactior electrodes. Different carbon material electrodes have been intensively studied.[34,38,39] Carbon materials generally have high surface area, 1000 ~ 2000 m^2/g, e.g., activated carbon, carbon cloth, and carbon aerogels. The capacity of the basal plane and edge plane of graphite carbon are about 10-40 μF/cm^2 and 50-70 μF/cm^2,[40] respectively. High surface area and porosities can be achieved by carbonization, physical or chemical activation,[41,42,43] phase separation,[44] gelation,[44] emulsification,[45,46] aerogel-xerogel formation,[47] replication,[48] or burning carbon composites with controllable sizes and volume fractions of open pores which involves adding raw polymer particles, e.g. poly(methyl methacrylate) (PMMA) spheres,[3] silica sol and silica gel as templates.[49,50,51] Generally activated carbon is a powder, so some processing is necessary to transform these materials into solid compact electrodes. These methods include permanent pressure[34] and adding binders such as polytetrafluoroethylene (PTFE),[52,53] poly(vinylidene fluoride-hexafluoropropylene),[54] methylcellulose,[53] and aqueous dispersions of polystyrene, styrene/butadiene copolymer and ethylene/acrylic acid copolymer,[55] etc. Theoretically, the specific capacitance of carbon materials should increase with surface area. However, Shi et al.[34,39] studied several activated carbon materials with different surface area, pore size, pore size distribution and pore volume, and correlated these parameters with electrochemical capacitance and found that the hypothesis is not necessarily true in practical cases.

Frackowiak et al.[33] reported that porous texture of the carbon determines the ionic conductivity, which is related to the mobility of ions inside the pores. The rate of electrochemical accessibility is determined by the mobility of ions inside the pores, which is different from that in bulk electrolytes. Therefore, a resistor network was suggested to be considered in the equivalent circuit model instead of one resistor due to the uneven resistance throughout the whole materials.

Carbon aerogels are monolithic three-dimentional mesoporous network of carbon nanoparticles, which are obtained from the pyrolysis of organic aerogels based on resorcinol-formaldehyde or phenol-furthural precursors via a sol-gel process. While carbon xerogels[56,57] are obtained from a precursor prepared by conventional drying, and not by supercritical method in CO_2. Carbon aerogel and xerogels are considered as promising materials for supercapacitors, because they have high surface area, low density, good electrical conductivity, and require no additional binding materials. In order to improve the capacitance of carbon materials, functional groups are introduced into the carbon materials because the functional groups are related to the pseudocapacitance, which is a very effective method of increasing the capacitance. Chu et al.[58] investigated the effects of pretreatment and surface modification on the electrical double-layer capacitance of various carbon electrodes, and the surface modification of carbon electrodes compromise electrochemical and chemical techniques such as oxidation/reduction and preadsorption of various surface functional groups. The methods and the effects are summarized in Table 1.2. The

capacitance of the surface-treated carbon electrodes was measured by cyclic voltammetry and found to improve to various degrees.

Table 1.2. Modifications and effects of carbon materials on electrode[58]

Methods	**Results**
Liquid or gas-phase oxidation	Increase in surface area and porosity, lower density, increase in concentration of surface functional groups
Plasma treatment (e.g.atomic oxygen)	Increase in surface area and porosity, improvement in wettability, increase in concentration of surface functional groups, decrease in electrical resistance, increase in electrocatalytic activity for oxygen reduction
Heat treatment in inert environment (e.g. N_2)	Decrease in surface area and porosity, higher density, more graphitic surface structure, decrease in concentration of surface functional groups

Firsich[59] and Jurewicz et al.[60] also used similar methods to modify carbon materials and attempted to improve the energy storage capability. Unfortunately, the available high surface area carbons, such as activated carbon and carbon fiber, always have a wide pore size distribution ranging from the micropores (< 2 nm) to macropores (> 50 nm). A new technique has been reported to produce nanostructured carbon electrodes.[61] In this method, the nanostructured carbon films were grown by supersonic cluster beam deposition, so the films have highly

accessible surface area needed for supercapacitors due to the structure based on the nanotube embryos and porosity with grain size of a few tens of nanometers. Specific capacitance, power density and energy density of these nanostructured carbon electrodes in a quaternary ammonium salt in the propylene carbonate electrolyte are about 75 F/g, 506 kW/kg, and 76 Wh/kg, respectively. Another promising carbon material for supercapacitors is carbon nanotubes, which are reviewed in a separate section.

1.3.2 Metal Oxide Based Supercapacitor

Besides the carbon material electrodes, metal oxide electrodes are very important in electrical storage devices. Trasatti et al.[62] first used RuO_2 as supercapacitor electrodes. The RuO_2 electrode, also called dimensionally stable anodes (DSA), is prepared thermochemically from $RuCl_3$ or $(NH_4)_3RuCl_6$ painted on Ti substrates between 350 ˚C and 550 ˚C, with the addition of titanium isopropoxide or $TiCl_3$. The RuO_2-aqueous system has been extensively studied,[6,63] and the specific capacitance was reported to be as high as 720 F/g with H_2SO_4 electrolyte.[63] However, the metal used is very expensive. Recently, other metal oxides for supercapacitor have also been investigated, such as IrO_2,[23] MnO_2,[24] NiO,[64] SnO_2,[65] Fe_3O_4.[66] The capacitance of Fe_3O_4 in Na_2SO_3 aqueous solution is also very encouraging, from a few tens to 510 F/g, and depends on the state of dispersion of the oxide crystallites.[66]

1.3.3 Conducting Polymer Based Supercapacitor

Conducting polymers, such as polyaniline, polypyrrole, polythiophenes, polyacetylene, and poly[bis(phenylamino)disulfide],[67] comprise a large degree of π-orbital conjugations that lead to electronic conductivity, and can be oxidized or reduced electrochemically by withdrawal or injection of electrons, respectively. The charge storage mechanism in conducting polymers is illustrated in Figure 1.3. Recently, Prasad et al.[68] coated the PANI on the stainless steel by a potentiodynamic method from an acidic electrolyte and obtained very high specific capacitance, up to 450 F/g.

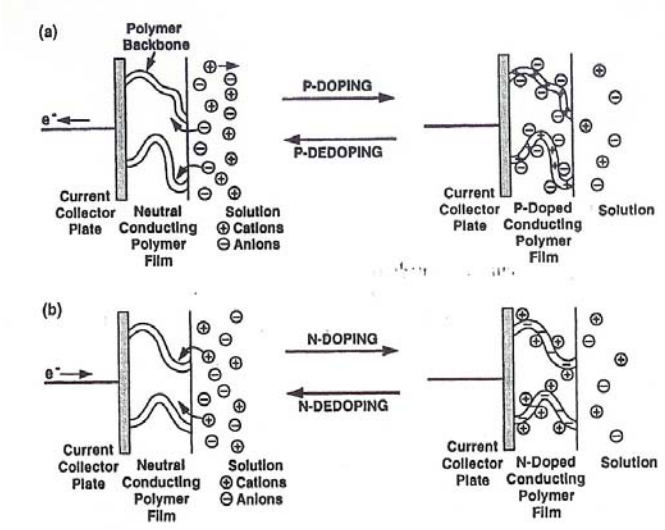

Figure 1.3. Development of a quasi-linear double layer at a charged conducting polymer chain.[6]

As discussed above, different electrode materials have different strong points and drawbacks. In order to take full advantage of different electrode materials,

composite supercapacitor electrodes made from metal oxide/conducting polymer,[69] conducting polymer/carbon nanotube,[70,71,72] activated carbon/conducting polymer,[73] activated carbon/carbon nanotube,[74] metal oxide/activated carbon,[75,76] and metal oxide/carbon nanotube[77] have been studied.

1.4 Carbon Nanotube

Carbon nanotubes are very attractive both for industrial and academic research due to their unique properties, as has been reviewed by Baughman et al.[78] and Popov.[79] In 1991, Iijima[80] first observed the multi-walled carbon nanotubes (MWNT). In 1993, Iijima and Ichihashi[81] and Bethune et al.[82] reported the observation of single wall carbon nanotube (SWNT) almost at the same time. Synthesis techniques of carbon nanotube include arc discharge,[80,81,82] laser-ablation,[83] and chemical vapor decomposition (catalytic growth),[84] and High-pressure CO disproportionation (HiPco).[85,86]

The mechanical properties, electronic conductivity, thermal conductivity and optical properties of carbon nanotubes are very impressive. The tensile strength and Young's modulus of individual SWNT can be as high as 37 GPa[87,88] and 640 GPa.[89] Electrical conductivity of SWNT is of the order of 10^6 S/m at room temperature,[90] and 5000 S/m for aligned MWNT film along the tube axis.[91] Some SWNTs with small diameter also exhibit superconductivity at low temperature, such as 1.4-nm-diameter SWNT with transition temperature at 0.55 K,[92] and 0.5-nm-diameter SWNT grown in zeolites with transition temperature at 5 K.[93]

Thermal conductivity of individual MWNT (> 3000 W/m.K)[78] is higher than that of the natural diamond and that of the basal plane of graphite (2000 W/m.K), but lower than that of the isolated SWNT (6600 W/m.K)[94] at room temperature, which is comparable to the thermal conductivity of a hypothetical isolated graphene monolayer. Optical properties of SWNT have been analyzed in detail, and the mean diameter and diameter distribution in bulk SWNT samples can be accurately determined from a combined study of optical absorption, high-resolution electron energy-loss spectroscopy in transmission, and tight-binding calculations.[95]

The specific surface areas of individual carbon nanotubes and bundles of carbon nanotubes have been calculated as a function of tube diameter, the number of walls and the number of carbon nanotubes in a bundle.[96] The specific surface area of an individual tube with 1 nm diameter can be as high as 1315 m^2/g, while 400 m^2/g for the bundles of 7 nm diameter (for SWNT of 1 nm diameter).

Based on these properties, numerous applications or potential applications have been reported for carbon nanotubes,[78,79] such as conductive and high-strength composites, hydrogen storage media, energy storage and energy conversion devices, field emission displays, and radiation sources, and nanometered-sized semiconductor devices, sensors, probes, interconnects, field-effect transistors, single electron transistors, rectifying diodes.

1.5 Carbon Nanotube Based Supercapacitor

The reported specific capacitance values of the carbon nanotubes range from 20 F/g to > 300 F/g. The supercapacitor electrodes prepared from MWNT were first reported by Niu et al.[35] with specific capacitance, power density and energy density of values of 113 F/g, 8 kW/kg and 0.56 Wh/kg, respectively, when 38 wt% H_2SO_4 aqueous solution was used as electrolyte. Ma et al.[36] also reported MWNT supercapacitor electrodes, which have relatively low specific capacitance values of 15-25 F/g also in 38 wt% H_2SO_4 solution. The SWNT electrodes in the form of bucky paper give a specific capacitance value of 40 F/g in 6 M KOH aqueous solution,[29] and 20-40 F/g in NaCl aqueous electrolyte.[97,98,99] Similar results were also reported in 1.0 M $LiClO_4$/propylene carbonate electrolytes by Shiraishi et al.[100] However, Liu et al.[101] reported that the specific capacitance of SWNTs in acetonitrile electrolyte containing 0.1 M tetra-n-butylammonium hexafluorophosphate is around 280 F/g.

Physical and chemical activation are general practices for producing large specific surface area activated carbon (~2000 m^2/g).[41,42,43] This approach was also used for the treatment of carbon nanotube based electrodes to improve the specific surface area by introducing micropores to enhance the capacitance performance. Physically activated[102] and chemically activated[103,104] carbon nanotube electrodes were reported to have significantly higher specific surface area as well as the specific capacitance over non-activated electrodes. Besides pore structures and specific surface area, the wetting capability of the electrode materials is also an important property that affects the capacitance behavior. For this reason, hot nitric acid,[33,70,105]

fluorine,[106] or ammonia plasma[107] functionalized carbon nanotube electrodes have been tested for capacitance performance. However, the pseudofaradaic reactions induced by the surface functional groups lead to unstable capacitance and increased current leakage.[33,104,105]

Conducting polymers, such as polyacetylene, polypyrrole, polyaniline, polythiophene, and their derivatives are also common electrode materials for supercapacitors.[108,109,110] The modification of CNTs with conducting polymers is one way to increase the capacitance of the composite resulting from redox contribution of the conducting polymers.[29] In the CNT/conducting polymer composite, CNTs are electron acceptors, while the conducting polymer serves as an electron donor. A charge-transfer complex is formed between CNTs in their ground state and aniline monomer.[111] A number of CNT/conducting polymer composite studies for electrochemical capacitor application have been reported.[112,116,126]

The CNT/conducting polymer composite prepared by polymerization of pyrrole on the nanotubes with ammonium persulfate as an oxidant exhibited capacitance value up to 180 F/g,[112] while SWNT/polypyrrole composite exhibited capacitance value up to 260 F/g.[113] In two separate studies, it was shown that the capacitance of an unoriented MWNT/polypyrrole composite was at least two times higher than that of either component.[72,114] Supercapacitor behavior of aligned arrays of CNTs coated with polypyrrole has also been reported.[115] Negatively charged MWNTs/polypyrrole layers were further investigated by co-deposition via electrochemical oxidation of pyrrole. Electrochemical quartz crystal microbalance (EQCM) confirmed the redox pseudocapacitance response of the polypyrrole with a mechanism involving rigid intercalation/deintercalation of counter ions into the polymer layer.[116] The capacitance of the layer composite was reported to be more

than 200 F/g in potassium chloride and tetrabutylammonium bromide solutions.[116] CNT matrices can provide a mesoporous scaffold, on which a porous layer of polypyrrole can be electrodeposited, hence a high charge dynamics during supercapacitor performance can be achieved.[117] A MWNT/poly(3-methylthyl-thiophene) composite based supercapacitor was evaluated in 1 M $LiClO_4$ acetonitrile solution, and its specific capacitance was about 80 F/g.[118] A MWNT/poly(3,4-ethylenedioxythiophene) composite, prepared by chemical or electrochemical polymerization, when evaluated in 1 M H_2SO_4, 6 M KOH, or 1 M tetraethylammonium tetrafluoroborate ($TEABF_4$) in acetonitrile, exhibited good cycling performance, and moderate capacitance values in the range from 60 to 160 F/g.[110] The capacitance of SWNT/polyaniline (PANI) composite fabricated by in-situ electrochemical polymerization was 310 F/g, higher than that of pure PANI, because the complex structure in this composite offered more active sites for Faradaic reactions.[119]

Among the carbon nanotube based supercapacitor electrodes, recently reported approaches using high temperature carbonization and/or CO_2 physical activation of carbon nanotube/polymer binary composite precursors[120,121] show very promising results. The pellet electrodes made from carbonized SWNT/poly(vinyldene chloride) (7:3) composites evaluated in 7.5 M KOH electrolytes give values of 180 F/g specific capacitance, 20 kW/kg power density and 7 Wh/kg energy density respectively.[120] SWNT/polyacrylonitrile (60:40) composite film[121] provides a unique handle on the pore structure and surface area to result in high performance.

1.6 Electrical Double Layer Model[122]

It is well known that pores with suitable size can greatly increase the surface

area and electrical double layer capacity of carbon materials. The pore size should be bigger than the thickness of the double layer, otherwise, the electrical double layer will overlap in the pores and lose its capacity. According to IUPAC, the pores can be classified into three categories: micropore (< 2 nm), mesopore (between 2 nm and 50 nm) and macropore (> 50 nm). A successful model should consider the effect of the double-layer overlapping which prevents ions from entering a micropore and results in a lower electrosorption capacity. Yang et al[122] developed such an electrical double layer model, which can investigate the effects of applied voltage and ion solution (NaF) concentration on the electrosorption capacity and determine the cutoff pore width (which is defined as the width of the smallest pore which can make contribution to the double layer capacity).

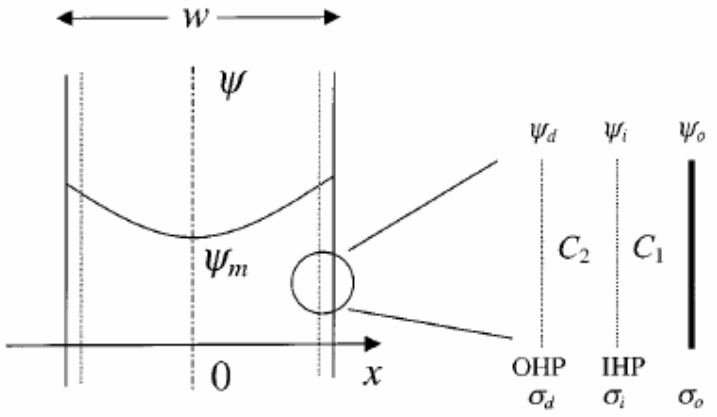

Figure 1.4. Theoretical distribution of electrical potential inside a pore of width *w*; the dotted lines indicate inner layers of the electrical double layer, which can be subdivided into the inner Helmholtz plane (IHP) and outer Helmholtz plane (OHP). The definitions of these parameters can be found in context.[122]

In this model, it is assumed that the total capacity is the sum of the all double

layer capacities of every pore in the carbon materials. As shown in Figure 1.4, a slit pore with width *w* is assumed forming by two planar plates separated by a distance of *w*. The planar Poisson-Boltzman equation can be used to express the electrical potential profile ψ in a symmetric electrolyte solution in such a pore. In the equation ψ is always positive due to the fact that only anion capacity is considered in this model. The Poisson-Boltzman equation is

$$\frac{\mathrm{d}^2\psi}{\mathrm{d}x^2} = \frac{2zeN_0}{\epsilon}\sinh\left(\frac{ze\psi}{kT}\right) \tag{6}$$

where ψ denotes the electrical potential, *x* represents the distance variable, *e* denotes the electrical charge of the electron, *z* is the valence of the ions, N_0 is the total number of ions in the bulk solution with a dielectric constant of *ε*, *T* is the absolute temperature and *k* is the Boltzmann constant.

In order to solve this equation, constant potential along *w* and diffuse layer boundary conditions were assumed as follows:

$$\frac{\mathrm{d}\psi}{\mathrm{d}x} = 0 \text{ and } \psi = \psi_{\mathrm{m}} \text{ at } x = 0 \tag{7}$$

$$\psi = \psi_{\mathrm{d}} \text{ at } x = \pm\frac{W}{2} \tag{8}$$

In these equations, ψ_{m} and ψ_{d} represent the electrical potentials at the midplane and the diffuse layer.

As one can see, the inner Helmholtz plane (IHP) and the outer Helmholtz plane (OHP) have different capacities which are defined as C_1 and C_2, respectively. Based on the Gouy-Chapman-Stern-Grahame model,[13] the charge density relates to potential, which can be described with following equations:

$$\psi_0 - \psi_i = \int_0^{\sigma_0} \frac{d\sigma_0}{C_1(\sigma_0)} \tag{9}$$

$$\psi_i - \psi_d = \int_0^{\sigma_d} \frac{d\sigma_d}{C_2(\sigma_d)} \tag{10}$$

where ψ_o and ψ_i are potentials at the surface and the IHP, σ_o represents the surface charge density, and σ_d represents the diffuse-layer charge density.

The anode and the cathode have same voltage but with opposite sign. Therefore, after applying voltage V, the surface potential is

$$\psi_0 = \frac{V}{2} - \phi_{ecm} \tag{11}$$

where ϕ_{ecm} is the potential at the electrical capillary maximum. The applying voltage has a limit because some faradaic reactions will occur if the applying voltage is too big. Only if V is small enough, ψ_o is the driving force of double layer capacity formation.

If the charge density at the IHP is zero, and C_1 is constant over the low voltage range, the diffuse layer potential (ψ_d) can be determined by combining equations (9 ~ 11). The expression of the diffuse layer potential is shown in equation (12).

$$\psi_d = \frac{V}{2} - \phi_{ecm} - \frac{\sigma_0}{C_1} \tag{12}$$

The surface charge density can be obtained by solving equation (6) with boundary conditions in equations (7) and (8). Hence, the surface charge density is

$$\sigma_0 = \sqrt{4\epsilon RTI}\left[\cosh\left(\frac{e\psi_d}{kT}\right) - \cosh\left(\frac{e\psi_m}{kT}\right)\right]^{1/2} \tag{13}$$

In this expression, R is the gas constant and I is the ionic strength.

If the applied potential is really low, Poisson-Boltzmann equation has a

solution as shown in equation (14).

$$\frac{\exp(e\psi/2kT)-1}{\exp(e\psi/2kT)+1}=\left[\frac{\exp(e\psi_d/2kT)-1}{\exp(e\psi_d/2kT)+1}\right]\exp(-\kappa x) \tag{14}$$

$$\kappa=\left(\frac{2N_A Ie^2}{\epsilon kT}\right)^{1/2} \tag{15}$$

where κ is called Debye-Hückel parameter and N_a is Avogadro's number.

In this case, ψ_m can be calculated by substituting x = w/2 into equation (14). By substituting ψ_m's expression in equation (15), the surface charge density is obtained as follows.

$$\sigma_0=\sqrt{4\epsilon RTI}\left[\cosh\left(\frac{e\psi_d}{kT}\right)-\cosh\left\{8\left[\frac{\exp(e\psi_d/2kT)-1}{\exp(e\psi_d/2kT)+1}\right]\exp(-\kappa w/2)\right\}\right]^{1/2} \tag{16}$$

If κ is relatively large, the expression of the surface charge density can be simplified further as shown in equation (17).

$$\sigma_0=\sqrt{8\epsilon RTI}\sinh\left(\frac{e\psi_d}{2kT}\right) \tag{17}$$

The cutoff pore width is the smallest width of pore which can make contribution to the double layer capacity. Hence, the cutoff pore width is the value when the surface charge density is equal to zero. Therefore, the cutoff pore width can be obtained as shown in equation (18). Based on the simulation, the cutoff pore width can be in a range of 5 to 50 Å, which is strongly dependent on the diffuse layer potential and Debye-Hückel parameter κ.

$$w_m=\frac{2}{-\kappa}\ln\left\{\frac{e\psi_d[\exp(e\psi_d/2kT)+1]}{8kT[\exp(e\psi_d/2kT)-1]}\right\} \tag{18}$$

Although the model can be successful to predict the cutoff pore width, it has some limitations because it ignores the ion size and assumes the compact layer thickness is

less than pore width. It also must emphasize that the model is only useful for low electrolyte concentration and low surface potential. The simulation results meet the experimental results very well for carbon aerogel electrodes in 0.1 M NaF solutions at voltages up to 1.2 V if the overlapping effect is considered. Otherwise, the model overestimates the electrical double layer capacity.

1.7 Pore Analytical Models

1.7.1 BET Theory

BET theory is named after its originators, Brunauer, Emmett, and Teller and was first published in 1938.[123,124] They extended the Langmuir theory[125], so that BET theory applies not only to monolayer molecular adsorption, but also to multilayer adsorption. In this model, they assume no interaction between gas molecules and solid surface. Gas molecules physically adsorb on a solid in layers infinitely, and forces active in the condensation of gases are also responsible for the binding energy in multimolecular adsorption. The phenomenon of adsorption can be expressed with the following equation.

$$\frac{P}{V_a(P_0 - P)} = \frac{1}{V_m C} + \frac{C-1}{V_m C}\left(\frac{P}{P_0}\right) \tag{19}$$

$$C\alpha \exp\frac{q_1 - q_L}{RT} \tag{20}$$

where V_a is the quantity of gas adsorbed at pressure P, V_m is the quantity of gas adsorbed when the entire surface is covered with a monomolecular layer, and b is an empirical constant. P_0 is the saturation pressure of the gas. q_1 is the heat of

adsorption of the first layer, and q_L the heat of liquefaction of the adsorptive, R is gas constant and T is the absolute temperature. The linear relationship of plot of $P/[V_a(P_0 - P)]$ vs. P/P_0 is maintained only in the range of $0.05 < P / P_0 < 0.35$. The value V_m can be determined from the intercept and slope of this plot. Hence the surface area of solids by physical adsorption of gas molecule can be obtained.

The specific surface area can be calculated by equation (21).

$$s = \frac{V_m \sigma N_A}{m V_o} \tag{21}$$

where σ is the area of the surface occupied by individual gas molecules and N_A is the Avogadro constant, m is the mass of absorbing sample and V_o is the molar volume of the gas, which is 22414 cm^3/molar for gas at atmospheric pressure.

If the pores are viewed as cylinders, then the pore volume V is $\pi(D/2)^2 L$, and the pore surface area, s, is equal to πDL, hence the average pore width is equal to $4V/s$ by BET method (where D is the diameter of the pore, L is the pore length, $L \gg D$, and V is V_m).[126]

1.7.2 Density Function Theory[126,,127,128]

Density function theory (DFT) is a molecular-based statistical thermodynamic theory, which relates the adsorption isotherm to the microscopic properties of the system.[126] The gas atoms in the pore space are influenced by an external attractive force or van der Waal's forces, so that they spend long time on the solid surface. A greater average density of gas atoms is formed in the space near the solid surface than away from it. At equilibrium state, a model can be developed for the adsorption

isotherm for the system because the distribution of gas molecules near the surface can be described by a function of pressure and molecular properties of the components.

The detailed procedure on evaluation of pore structure with DFT theory has been described by Webb and Orr.[126] For a porous structure with distributive slit-shaped pore, the pore area contributed by pores of size H is given by $f(H)$. Let $q(p, H)$ be the quantity of adsorbate adsorbed per unit area at pressure p in a pore of size H. Therefore, the total amount of adsorbate at pressure p, $Q(p)$, is given by the integral equation as follows:

$$\boldsymbol{Q(p) = \int q(p, H)\, f(H) dH} \tag{22}$$

It is convenient to describe equation (22) for each individual pressure point as:

$$\begin{bmatrix} \boldsymbol{Q(p_1)} \\ \boldsymbol{Q(p_2)} \\ \vdots \\ \boldsymbol{Q(p_n)} \end{bmatrix} = \begin{bmatrix} \boldsymbol{q(p_1, H_1)} & \boldsymbol{q(p_1, H_2)} & \cdots & \boldsymbol{q(p_1, H_m)} \\ \boldsymbol{q(p_2, H_1)} & \boldsymbol{q(p_2, H_2)} & \cdots & \boldsymbol{q(p_2, H_m)} \\ \vdots & \vdots & \vdots & \vdots \\ \boldsymbol{q(p_n, H_1)} & \boldsymbol{q(p_n, H_1)} & \cdots & \boldsymbol{q(p_n, H_1)} \end{bmatrix} \begin{bmatrix} \boldsymbol{f(H_1)} \\ \boldsymbol{f(H_2)} \\ \vdots \\ \boldsymbol{f(H_m)} \end{bmatrix} \tag{23}$$

In the equation, $Q(p_1)$, $Q(p_2)$, … and $Q(p_n)$ are the experimentally determined values from the adsorption isotherm. Therefore, as long as the kernel matrix, $q(p_i, H_j)$, are known, $f(H_j)$, which provides pore size distribution information, could be evaluated with a least-square method. $q(p_i, H_j)$, quantity of adsorbate adsorbed per unit area at pressure p_i in a pore of size H_j can be obtained by integrated the equilibrium density profile, $\rho(r)$, of the adsorbates on the adsorbent surface for a particular pore shape.

Various approaches, e.g., molecular dynamics, Monte Carlo simulation, and density functional theory (DFT), offer the techniques to calculate $\rho(r)$ for a given pair of adsorbate and adsorbents. Nevertheless, DFT provides a practical solution in the sense of accuracy and less computational requirements.[126] As shown by Tarazona,[129]

the equilibrium density profile for hard-sphere interacted with hard-wall, can be obtained by minimizing the free-energy density function $W[\rho(r)]$ which has the following equation:

$$W[\rho(r)] = F[\rho(r)] + \int dr\rho(r)(V(r) - \mu) \qquad (24)$$

where $\rho(r)$ is the density profile of the hard-spheres, $F[\rho(r)]$ is the intrinsic Helmholtz free energy considered as a function of the particle density distribution, $V(r)$ is the external potential due to the hard-wall, and μ is the chemical potential. Distinguishing the contribution from both repulsive and attractive forces between hard-spheres, the free energy $F[\rho(r)]$ is given by:

$$\begin{aligned} \boldsymbol{F}[\boldsymbol{\rho}(\boldsymbol{r})] &= \boldsymbol{F}_{\boldsymbol{repulsive}}[\boldsymbol{\rho}(\boldsymbol{r})] + \boldsymbol{F}_{\boldsymbol{attractive}}[\boldsymbol{\rho}(\boldsymbol{r})] \\ &= \int \boldsymbol{f}_{\boldsymbol{hs}}[\boldsymbol{\rho}(\boldsymbol{r})]\boldsymbol{dr} + \frac{1}{2}\int\int \boldsymbol{\rho}(\boldsymbol{r})\boldsymbol{\rho}(\boldsymbol{r}')\boldsymbol{u}(\boldsymbol{r},\boldsymbol{r}')\boldsymbol{dr}\boldsymbol{dr}' \end{aligned} \qquad (25)$$

where $f_{hs}[\rho(r)]$ is the Helmholtz free energy density of a uniform hard-sphere fluid calculated using an appropriate equation of state, and *u(r, r')* is the pair-wise attractive potential calculated from the Lennard-Jones relation by:

$$\boldsymbol{u}(\boldsymbol{r},\boldsymbol{r}') = -4\boldsymbol{\varepsilon}\left[\left(\frac{\boldsymbol{\sigma}}{|\boldsymbol{r}-\boldsymbol{r}'|}\right)^6 - \left(\frac{\boldsymbol{\sigma}}{|\boldsymbol{r}-\boldsymbol{r}'|}\right)^{12} \right] \qquad (26)$$

In Lennard-Jones relation, ε and σ represent the depth of the intermolecular potential well and the molecular size, respectively.

Combining equations (24), (25) and (26), the equilibrium density profile, $\rho(r)$, for a particular pair of absorbates and adsorbents under assumed pore geometry, can be solved. Consequently, $q(p_i, H_j)$, quantity of adsorbate adsorbed per unit area at pressure p_i in a pore of size H_j can be obtained. As a result, using experimentally determined adsorption isotherms, one can calculate the pore size distribution using

equation (23).

The total pore volume of the absorbent from the DFT is V_{STP}, which is obtained by equation (27).

$$V_{STP} = \left(\frac{273.2}{T}\right)\left(\frac{P}{760}\right)V_I \tag{27}$$

In this equation, T and P are ambient temperature and pressure. V_I is the total amount of adsorbate $Q(p)$ in equation (22).

Once the total pore volume V_{STP} is obtained, the total surface area, s, is given by equation (28).

$$s = 16.2 \times 10^{-20}(N_A)(V_{STP}) \tag{28}$$

where N_A is Avogadro's number. As to the the average pore width, DFT has the same equation as BET, but substituting s and V in $4V/s$ with values obtained from DFT.

1.8 Thesis Objectives

Limited studies to date indicate that carbon nanotube based electrodes may have promising potential for supercapacitor application. However, up to now, no systematic pore structure control scheme has been developed for this new type of supercapacitor electrodes. Considering the significant effects of pore structure on the capacitance performance of supercapacitor electrodes,[34] one can immediately appreciate the value of a proper pore structure control scheme for the CNT based supercapacitor electrodes. In this thesis, three approaches are presented to study CNT application in supercapacitors. The first approach is to realize pore structure

control of CNT based supercapacitor electrodes. This approach involves stabilization and carbonization of a composite film composed of SWNTs and two polymer components, in which one polymer provides the carbon source and the other is used as a sacrificial component for pore structure control. In the second approach, CNTs will be functionalized with different chemicals and to different degrees. The effect of functionalization on the SWNT capacitance performance has been evaluated. In the last approach, the arylsulfonic acid functionalized SWNT has been wrapped with a conducting polymer, polypyrrole. This approach is designed to take full advantage of SWNT and conducting polymers, for developing high performance supercapacitors.

1.9 References

1 H. E. Becker. U.S. Patent 2 800 616, **1957**.

2 D. I. Boos. U.S. Patent 3 536 963, **1970**.

3 B. E. Conway. *J. Electrochem. Soc.* **1991**, *138*, 1539.

4 S. Sarangapani, B.V. Tilak, C. P. Chen. *J. Electrochem. Soc.* **1996**, *143*, 3791.

5 T. C. Murphy, R. B. Wright, R. A. Sutula, in: F. M. Delnick, D. Ingersoll, X. Andrieu, K. Naoi (Eds.), *Electrochemical Capacitors II, Proceedings*, vols. 96–25, The Electrochemical Society, Pennington, NJ, **1997**, p 258.

6 B. E. Conway. *Electrochemical Supercapacitors, Scientific Fundamental and Technological Applications*, Plenum Publishers, **1999.**

7 http://www.nuin.co.kr/html/pro6.html.

8 R. Kotz, M. Carlen. *Electrochim. Acta* **2000**, *45* , 2483.

9 A. J. Bard, and L. R. Faulkner. *Electrochemical Methods, Fundamentals and Applications(2nd)*, John Wiley & Sons, Inc, **2001**.

10 H. Von Helmhlotz. *Ann. Phys.* **1853**, *89*, 211.

11 D. L. Chapman. *Phil. Mag.* **1913**, *25*, 475.

12 O. Stein. *Zeit. Elektrochem.* **1924**, *30*, 508.

13 D. C. Grahame. *Chem. Rev.* **1947**, *41*, 441.

14 A. Soffer, M. Folman. *Journal of Electroanalytical Chemistry and Interfacial Electrochemistry* **1972**, *38*, 25.

15 Y. Oren, H. Tobias, A. Soffer. *Journal of Electroanalytical Chemistry and Interfacial Electrochemistry* **1984**, *162(1-2)*, 87.

16 Y. Oren, A. Soffer. *Journal of Electroanalytical Chemistry and Interfacial Electrochemistry* **1985**, *186*, 63.

17 Y. Oren, A. Soffer. *Journal of Electroanalytical Chemistry and Interfacial Electrochemistry* **1986**, *206*, 101.

18 D. Golub, Y. Oren, A. Soffer. *Journal of Electroanalytical Chemistry and Interfacial Electrochemistry* **1987**, *227*, 41.

19 D. Golub, A. Soffer, Y. Oren. *Journal of Electroanalytical Chemistry and Interfacial Electrochemistry* **1989**, *260*, 383.

20 M. Muller, B. Kastening. *J. Electroanal. Chem.* **1994**, *374*, 149

21 B. Kastening, M. Hahn, J. Kremeskotter. *J. Electroanal. Chem.* **1994**, *374*, 159

22 T. C. Liu, W. G. Pell, B. E. Conway. *Electrochim Acta* **1997**, **42**, 3541.

23 D. Mitchell, D. A.J.Rand, R. Woods. *J. Electroanal. Chem.* **1973**, *43*, 9.

24 T. Arikado, C. Iwakura, H. Tamura. *Electrohim. Acta* **1977**, *22*, 513.

25 A. Rudge, I. Raistrick, S. Gottesfeld, J. P. Ferraris. *Electrochim. Acta* **1994**, *39*, 273.

26 J. P. Ferraris, M. M. Eissa, I. D. Brotherston, D. C. Loveday, A. A. Moxey. *J. Appl. Electrochem.* **1998**, *459*, 57.

27 A. Laforgue, P. Simon, C. Sarrazin, J. F. Fauvarque. *J. Power Sources* **1999**, *80*, 142.

28 M. Mastragostino, C. Arbizzani, F. Soavi. *J. Power Sources* **2001**, *97-98*, 812.

29 E. Frackowiak, K. Jurewicz, S. Delpeux, F. Beguin. *J. Power Sources* **2001**, *97-98*, 822.

30 D. Belanger, X. Ren, J. Davey, F. Uribe, S. Gottesfeld. *J. Electrochem. Soc* **2001**, *147*, 2923.

31 F. Fusalba, P. Gouerec, D. Villers, D. Belanger. *J. Electrochem. Soc.* **2001**,*148*, A1.

32 K. Rajendra Prasad, N. Munichandraiahz. *J. Electrochem. Soc.***2002**, *149 (11)*, A1393.

33 E. Frackowiak, F. Beguin. *Carbon* **2001**, *39 (6)*, 937.

34 H. Shi. *Electrochim Acta* **1996**, *40(10)*, 1633.

35 C. Niu, E. K. Sichel, R. Hoch, D. Moy, H. Tennent. *Appl. Phys. Lett.* **1997**, *70(11)*, 1480.

36 R. Z. Ma, J. Liang, B. Q. Wei, B. Zhang, C. L. Xu, D. H. Wu. *J. Power Sources* **1999**, *84*, 126.

37 L. Diederich, E. Barborini, P. Piseri, A. Podesta, P. Milani, A. Schneuwly, R. Gallay. *Appl. Phys. Lett.* **1999**, *75*, 2662.

38 X. Andrieu, L. Josset. *Proceedings - Electrochemical Society* **1996,** *95-29* (Electrochemical Capacitors), 181-186.

39 D. Qu , H. Shi. *J. Power Sources* **1998**, *74*, 99–107.

40 J. Randin, E. Yeager. *J. Electrochem. Soc.* **1971**, *118*, 711.

41 R.Torregrosa, J. M. Martín-Martínez. *Fuel* **1991**, *70 (10)*, 1173.

42 F. Fodriguezreinoso, M. Molinasabio. *Carbon* **1992**, *30 (7)*, 1111.

43 J. Laine, S. Yunes. *Carbon* **1992**, *30 (4)*, 601.

44 H. Hatori, Y.Yamada, M. Shiraishi. *Carbon* **1991**, *30*, 303.

45 D. Barby, Z. Haq. European Patent 0060138, **1982**.

46 C. J. C. Edwards, D. A. Hitchen, M. Sharples. US Patent 4775655, **1988**.

47 R.W. Pekala, C. T. Alviso, J. D. LeMay. *J. Noncrystal solids* **1990**, *125*, 67.

48 R.W. Pekala, R.W. Hooper. *J. Materials Science* **1989**, *22*,1840.

49 J. Lee, S. Han, T. Hyeon. *Journal of Materials Chemistry* **2004**, *14(4)*, 478-486.

50 K. Jurewicz, C. Vix-Guterl, E. Frackowiak, S. Saadallah, M. Reda, J. Parmentier, J. Patarin, F. Beguin. *Journal of Physics and Chemistry of Solids* **2004**, *65(2-3)*, 287-293.

51 C. Vix-Guterl, S. Saadallah, K. Jurewicz, E. Frackowiak, M. Reda, J. Parmentier, J. Patarin, F. Beguin. *Materials Science & Engineering B* **2004**, *B108(1-2)*, 148-155.

52 M. F. Rose, C. Johnson, T. Owens, B. Stephens. *J. Power Sources* **1994**, *47*, 303.

53 L. Bonnefoi, P. Simon, J. F. Fauvarque, C. Sarrazin, J. F. Sarrau, A. Dugust. *J. Power Sources* **1999**, *80*,149.

54 T. Osaka, X. Liu, M. Nojima, T. Momma. *J. Electrochem. Soc.* **1999**, *146(5)*, 1724-1729.

55 F. Beck, M. Dolata. *Journal of Applied Electrochemistry* **2001**, *31(5)*, 517-521.

56 C. Lin, J. A. Ritter. *Carbon* **1997**, *35(9)*, 1271-1278.

57 E. J. Zanto, J. A. Ritter, B. N. Popov. *Proceedings - Electrochemical Society* **1999**, *98-16*(Lithium Batteries), 71-81.

58 X. Chu, K. Kinoshita. *Proceedings - Electrochemical Society* **1996**, *95-29* (Electrochemical Capacitors), 235-245.

59 D. W. Firsich. U.S. Patent 5993996, **2002**.

60 K. Jurewicz, K. Babel, A. Ziolkowski, H. Wachowska. *Journal of Physics and Chemistry of Solids* **2004**, *65(2-3)*, 269-273.

61 L. Diederich, E. Barborini, P. Piseri, A. Podesta, P. Milani. *Appl. Phys. Lett. 1999*, *75(17)*, 2662.

62 S. Trasattu, G. Buzzanca. *Journal of Electroanalytical Chemistry and Interfacial Electrochemistry* **1971**, *29(2)*, 1-2.

63 J. P. Zheng, P. J. Cygan, T. R. Jow. *J. Electrochem. Soc.* **1995**, *142(8)*, 2699-2703.

64 V. Srinivasan, J.W. Weidner. *J. Electrochem. Soc.***1997**, *144 (8)*, L210-L213.

65 N. L. Wu. *Materials Chemistry and Physics* **2002**, *75 (1-3)*, 6-11.

66 N-L. Wu, Y.-P. Lan, C.-Y. Han, S.-Y. Wang, L.-R. Shiue. *Proceedings - Electrochemical Society* **2002**, 2002-7(Electrochemical Capacitor and Hybrid Power Sources), 95-106.

67 Y.-Z. Su, Y.-P. Niu, Y.-Z. Xiao, M. Xiao, Z.-X. Liang, K.-C. Gong. *Journal of Polymer Science, Part A: Polymer Chemistry* **2004**, *42(10)*, 2329-2339.

68 K. R. Prasad, N. Munichandraiah. *J. Power Sources* **2002**, *112*, 443-451.

69 J. I. Hong, I. H. Yeo, W. K. Paik. *J. Electrochem. Soc* **2001**, *148 (2)*, A156.

70 Y. H. Lee, K. H. An, S. C. Lim, W. S. Kim, H. J. Jeong, C. H. Doh, S. I. Moon. *New Diamond and Frontier Carbon Technology* **2002**, *12 (4)*, 209.

71 Q. F. Xiao, X. Zhou. *Electrochim Acta* **2003**, *48 (5)*, 575.

72 M. Hughes, G. Z. Chen, M. S. P. Shaffer, D. J. Fray, A. H. Windle. *Chemistry of Materials* **2002**, *14(4)*, 1610-1613.

73 W.-C. Chen, T.-C. Wen. *J. Power Sources* **2003**, *117*, 273-282.

74 K. Liang , A. Chen, Z. S. Feng , Z. X. Ye. *Acta Physico-Chimica Sinica* **2002**, *18 (4)*, 381.

75 J. H. Jang, S. Han, T. Hyeon, S. M. Oh. *J. Power Sources* **2003**, *123(1)*, 79-85.

76 M. Wu, G. A. Snook, G. Z. Chen, D. J. Fray. *Electrochemistry Communications* **2004**, *6(5)*, 499-504.

77 X. Qin, S. Durbach, G. T. Wu. *Carbon* **2004**, *42(2)*, 451.

78 R. H. Baughman, A. A. Zakhidov, W. A. de Heer. *Science* **2002**, *297*, 787-792.

79 V. N. Popov. *Material Science and Engineering R* **2004**, *43*, 61-102.

80 S. Iijima. *Nature* **1991**, *354*, 56-58.

81 S. Iijima, T. Ichihashi. *Nature* **1993**, *363*, 603.

82 D. S. Bethune, C. H. Kiang, M. S. de Vires, G. Gorman, R. Savoy, J. Vazquez, R. Beyers. *Nature* **1993**, *363*, 605.

83 A. Thess, R. Lee, P. Nikolaev, H. Dai, P. Petit, J. Robert, C. Xu, Y. H. Lee, S. G. Kim, A. G. Rinzler, D. T. Colbert, G. E. Scuseria, D. Tomanek, J. E. Fischer, R. E. Smalley. *Science* **1996**, *273*, 483.

84 M. J. Yacaman, M. M. Yoshida, L. Rendon, J. G. Santiesteban. *Appl. Phys. Lett.* **1993**, *62*, 202.

85 H. Dai, A. G. Rinzler, P. Nikolaev, A. Thess, D. T. Colbert, R. E. Smalley. *Chem. Phys. Lett.* **1996**, *260*, 471.

86 I. W. Chiang, B. E. Brinson, A. Y. Huang, P. A. Willis, M. J. Bronikowski, J. L. Margrave, R. E. Smalley, R. H. Hauge. *J. Phys. Chem. B* **2001**, *105*, 8297.

87 M.-F. Yu, B. S. Files, S. Arepalli, R. S. Ruoff. *Phys. Rev. Lett.* **2000**, *84(24)*, 5552.

88 D. A. Walters, L. M. Ericson, M. J. Casavant, J. Liu, D. T. Colbert, K. A. Smith, R. E. Smalley. *Applied Physics Letters* **1999**, *74(25)*, 3803-3805.

89 G. Gao, T. Cagın, W. A. Goddard. *Nanotechnology* **1998**, *9(3)*, 184-191.

90 J. E. Fischer, H. Dai, A. Thess, R. Lee, N. M. Hanjani, D. L. Dehaas, R. E. Smalley. *Physical Review B* **1997**, *55(8)*, R4921-R4924.

91 W. A. de Heer, W. S. Bacsa, A. Chatelain, T. Gerfin, R. Humphrey-Baker, L. Forro, D. Ugarte. *Science* **1995**, *268*, 845-847.

92 M. Kociak, A. Yu. Kasumov, S. Guéron, B. Reulet, I. I. Khodos, Yu. B. Gorbatov, V. T. Volkov, L. Vaccarini, H. Bouchiat. *Phys. Rev. Lett.* **2001**, *86(11)*, 2416-2419.

93 Z. K. Tang, L. Zhang, N. Wang, X. X. Zhang, G. H. Wen, G. D. Li, J. N. Wang, C. T. Chan, P. Sheng. *Science* **2001**, *292(5526)*, 2462-2465.

94 S. Berber, Y.-K. Kwon, D. Tománek. *Physical Review Letters* **2000**, *84(20)*, 4613-4616.

95 X. Liu, T. Pichler, M. Knupfer, M. S. Golden, J. Fink, H. Kataura, Y. Achiba. *Physical Review B* **2002**, *66*, 045411-045418.

96 A. Peigney, Ch. Laurent, E. Flahaut, R.R. Bacsa, and A. Rousset. *Carbon* **2001**, *39*, 507-514.

97 J. N. Barisci, G. G. Wallace, R. H. Baughman. *Electrochim. Acta* **2000**, *46*, 509-517

98 J. N. Barisci, G. G. Wallace, R. H. Baughman. *J. Electrochem. Soc.* **2000**, *147(12)*, 4580-4583.

99 J. N. Barisci, G. G. Wallace, D. Chattopadhyay, F. Papadimitrakopoulos, R. H. Baughman. *J. Electrochem. Soc.* **2003**, *150(9)*, E409-E415.

100 S. Shiraishi, H. Kurihara, K. Okabe, D. Hulicova, A. Oya. *Electrochemistry Communications* **2002**, *4*, 593-598.

101 C.-Y. Liu, A. J. Bard, F. Wudl, I. Weitz, J. R. Heath. *Electrochemical and Solid-State Letters* **1999**, *2 (11)*, 577-578.

102 C. S. Li, D. Z. Wang, T. X. Liang, G. T. Li, X. F. Wang, M. S. Cao, J. Liang. *Science in China Series E-Technological Sciences* **2003**, *46 (4)*, 349.

103 Q. Jiang, M. Z. Qu, G. M. Zhou, B. L. Zhang, Z. L. Yu. *Material Letters* **2002**, *57*, 988.

104 E. Frackowiak, S. Delpeux, K. Jurewicz, K. Szostak, D. Cazorla-Amoros, F. Beguin. *Chem. Phys. Lett.* **2002**, *361*, 35.

105 E. Frackowiak, K. Metenier, V. Bertagna, F. Beguin. *Appl. Phys. Lett.* **2000**, *77*, 2421.

106 J. Y. Lee, K. H. An, J. K. Heo, Y. H. Lee. *J. Phys. Chem. B* **2003**, *107*, 8812.

107 B.-J. Yoon, S.-H. Jeong, K.-H. Lee, H.-S. Kim, C. G. Park, J. H. Han. *Chem. Phys.* Lett. **2004**, *388*, 170-174.

108 D. Belanger, X. Ren, J. Davey, F. Uribe, S. Gottesfeld. *J. Electrochem. Soc*. **2000**, *147(8)*, 2923.

109 K. S. Ryu, X. Wu, Y.-G. Lee, S. H. Chang. *J. Appl. Polym. Sci.* **2003**, *89*, 1300.

110 K. Lota, V. Khomenko, E. Frackowiak. *J. Phys. Chem. Solids* **2004**, *65*, 295.

111 Y. Sun, S. R. Wilson, D. I. Schuster. *J. Am. Chem. Soc.* **2001**, *123*, 5348.

112 K. Jurewicz, S. Delpeux, V. Bertagna, F. Beguin, E. Frackowiak. *Chem. Phys. Lett.*

2001, *347*, 36.

113 K. H. An, K. K. Jeon, J. K. Heo, S. C. Lim, D. J. Bae, Y. H. Lee. *J. Electrochem. Soc.* **2002**, *149 (8)*, A1058.

114 C. Downs, J. Nugent, P. M. Ajayan, D. J. Duquette, S. V. Santhanam. *Adv. Mater.* **1999**, *11(12)*, 1028.

115 M. Hughes, M. S. P. Shaffer, A. C. Renouf, C. Singh, G. Z. Chen, D. J. Fray, A. H. Windle. *Adv. Mater.* **2002**, *14(5)*, 382.

116 G. A. Snook, G. Z. Chen, D. J. Fray, M. Hughes, M. Shaffer. *J. Electroanaly. Chem.*, **2004**, *568*, 135.

117 E. Frackowiak, K. Jurewicz, K. Szostak, S. Delpeux, F. Beguin. *Fuel Proc. Tech.* **2002**, *77–78*, 213.

118 Q. Xiao, X. Zhou. *Electrochimica Acta* **2003**, *48*, 575.

119 Y. Zhou, B. He, W. Zhou, H. Li. *J. Electrochem. Soc.* **2004**, *151(7)*, A1052.

120 K. H. An, W. S. Kim, Y. S. Park, J. M. Moon, D. J. Bae, S. C. Lim, Y. S. Lee, Y. H. Lee. *Adv. Mater.* **2001**, *13(7)*, 497.

121 T. Liu , T. V. Sreekumar , S. Kumar , R. H. Hauge , R. E. Smalley. *Carbon* **2003**, *41*, 2427.

122 K.-L. Yang, T.-Y. Ying, S. Yiacoumi, C. Tsouris, E. S. Vittoratos. *Langmuir* **2001,** *17,* 1961-1969.

123 S. Brunauer, P. H. Emmett, E. Teller. *J. Am. Chem. Soc.* **1938**, *60*, 309.

124 http://en.wikipedia.org/wiki/BET_theory.

125 I. Langmuir. *J. Am. Chem. Soc.* **1918**, *40*, 1631.

126 P. A. Webb, C. Orr. *Analytical Methods in Fine Particle Technology*, Micromeritics Instrument Corp. **1997**.

127 http://en.wikipedia.org/wiki/Density_functional_theory.

128 J. P. Oliver. *Carbon* **1998**, *36(10)*,1469.

129 P. Tarazona. *Physical Review A* **1985**, *31*, 2672.

CHAPTER 2

PAN/SWNT/SAN TERNARY COMPOSITE FILMS BASED SUPERCAPACITOR ELECTRODES

2.1 Introduction

Among the carbon nanotube based supercapacitor electrodes, recently reported approaches using high temperature carbonization and/or CO_2 physical activation of carbon nanotube/polymer binary composite precursors[1,2] show very promising results. The pellet electrodes made from carbonized SWNT/poly(vinyldene chloride) (in the 7:3 weight ratio) composites and evaluated in 7.5 M KOH electrolyte gave values of 180 F/g specific capacitance, 20 kW/kg power density and 7 Wh/kg energy density, respectively.[1] Core-sheath rope structure of SWNT/polyacrylonitrile (PAN) (60:40) composite film provides a unique handle for the control of pore structure and surface area of carbonized and activated SWNT/PAN composite film electrodes. [2]

Studies summarized above indicate that carbon nanotube based electrodes have significant potential for supercapacitor application. Considering the significant effect of pore structure,[3] the need for proper pore structure control for the carbon nanotube based supercapacitor electrodes becomes obvious. However, to date, no systematic pore structure control scheme has been developed. In this chapter, we present a novel approach to achieve pore structure control, involving stabilization and carbonization of a composite film composed of SWNTs and two polymer components, in which one of the polymer (PAN) is a carbon source and the second polymer

poly(acrylonitrile-co-styrene)(SAN) is used as a sacrificial component for pore structure control.

2.2. Experimental

2.2.1 Solution Preparation and Film Casting

Solution of PAN (containing less than 5% itaconic acid and methacrylate copolymer, from Enichem Solution Corp) and SAN (25 wt% acrylonitrile 75 wt% styrene copolymer, Mw = 165,000 g/mol, ACROS Organics) in dimethylformamide (DMF, Fisher Scientific) was prepared in desired PAN:SAN ratio in 40 g DMF. The polymer concentration is less than 3.75 mg/mL, but the exact value depends on the compositions. To this solution, HiPCO SWNTs with 35 wt% impurities or about 7 at% catalytic impurity (Fe)[4] (from Carbon Nanotechnologies Inc.) were added to make a PAN/SWNT/SAN suspension with total solid content of 150 mg. In the preparation of suspension, a few minutes of homogenization (Biohomogenizer M133/1281-0, ESGE, Switzerland) followed by 30 minutes of bath sonication (Ultrasonic processor operated at 550 Watts power and at a frequency of 20 kHz, Manufacturer Misonix Inc.) was applied. The PAN/SWNT/SAN composite films were formed by casting the prepared suspension onto a glass substrate and by evaporating the DMF in vacuum at 85 °C. The thickness of these composite films is typically about 26 μm. PAN/SWNT/SAN composite films with varying weight percentage of SWNT, PAN and SAN were prepared and the compositions are listed in Table 2.1. In PAN1 series composite films, the weight ratio of PAN to SWNT is

kept constant at 9 to 1, while SAN concentration is varied from 0 to 50 wt% with respect to the total weight. In PAN2 and PAN3 composite films, the weight ratio of PAN to SWNT is 20 to 1 and 5 to 1 respectively, while SAN concentration is kept constant at 30 wt%. A ternary diagram showing various compositions used is shown in Figure 2.1.

Table 2.1. Compositions of PAN/SWNT/SAN composite films

	PAN1-SAN0	**PAN1-SAN10**	**PAN1-SAN30**	**PAN1-SAN50**	**PAN2-SAN30**	**PAN3-SAN30**
SAN(%)	0	10	30	50	30	30
SWNT (%)	10.2	9.2	7.1	5.1	3.4	11.4
PAN (%)	89.8	80.8	62.9	44.9	66.6	58.6
PAN : SWNT	9:1	9:1	9:1	9:1	20:1	5:1
Residual weight on carbonization (%)	69.7	61.5	48.5	36.1	45.4	50.2

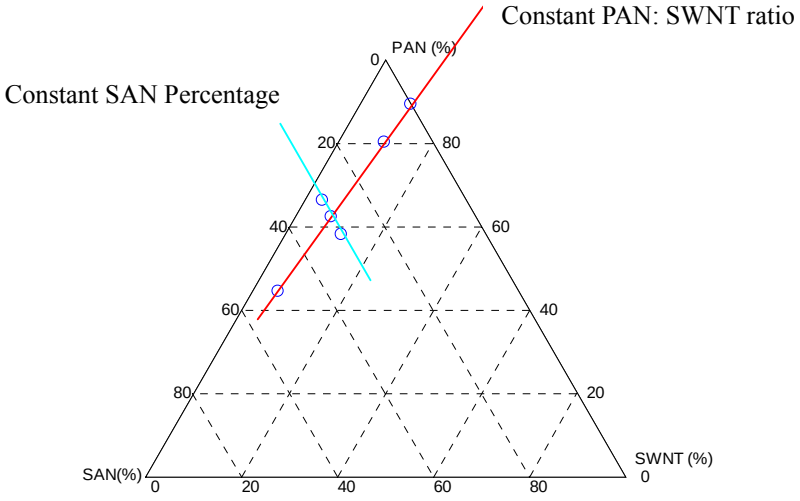

Figure 2.1. PAN-SWNT-SAN composition representation on a ternary diagram.

2.2.2 Film Pyrolysis

The composite film electrodes are prepared by first stabilizing PAN/SWNT/SAN composite film in air in a box furnace (Lindberg, 51668-HR Box Furnace 1200C from Blue M Electric) by heating from room temperature to 250 °C at a rate of 1 °C/min. After stabilization for 2 hours at 250 °C in air, argon is purged through the box furnace for a few minutes and then the temperature is raised at a rate of 5 °C/min to 700 °C and held at 700 °C for 30 minutes while maintaining argon flow.

2.2.3 Thermal and Morphological Characterization

Thermogravimetric analysis (TGA) was carried out on TGA 2950 (TA Instruments, Inc.) by heating the sample in nitrogen at 5 °C/min to 900 °C. The scanning electron microscopy (SEM) observation was performed on gold coated samples on LEO 1530.

2.2.4 Surface Area and Pore Size Distribution Measurements

The isothermal N_2 gas adsorption was carried out on Micromeritics gas adsorption analysis ASAP 2020 (from Micromeritics Instrument Corporation, Norcross, GA) at 77 K. The degassing conditions (90 °C for 16 hours at 1×10^{-4} Pa) are the same for all the samples. Mass of the sample after-degassing is used for the determination of the specific surface area and pore size distribution. The detailed data analysis procedure is reviewed in Sections 1.7.1 and 1.7.2.

2.2.5 Electrode Preparation and Electrochemical Analysis

Constant current charging/discharging and cyclic voltammetry measurements were carried out on Solartron 1470 Cell Test at room temperature. The testing cell used for this measurement is schematically shown in Figure 2.2, where two film electrodes (diameter = 1.27 cm) separated by Celgard 3400 microporous membrane were sandwiched between nickel current collectors. 6 M KOH aqueous solution or the ionic liquid was used for capacitance evaluation. In the constant current charging/discharging (CC) measurement, the cell was charged and discharged between 0 to 0.8 V for KOH aqueous solution and 0 to 3 V for 1-butyl-3-methyl imidazolium tetrafluoroborate (BMIMBF4) ionic liquid (obtained from Merck) electrolytes. The charging-discharging currents used in CC measurement were 0.5, 1, 5 and 10 mA. Scanning rates of 5, 10, 20, 50,100 and 200 mV/s were used in cyclic voltammetry (CV) measurements. The impedance spectroscopy of these materials was determined with Solartron 1255B Frequency Response Analyzer. A 0.05 V alternating current (AC) perturbation was used in the impedance measurements over a frequency range from 100 kHz to 50 mHz. The specific capacitance (C_{sp}), energy density (ED) and power density (PD) of the film electrodes were calculated using the following equations: [2]

$$C_{sp} = \frac{I}{dV(t)/dt}\left(\frac{1}{m_A} + \frac{1}{m_B}\right) \quad (1)$$

$$ED = \int_0^t IV(t)dt/(m_A + m_B) \quad (2)$$

$$PD = IV(t)/(m_A + m_B) \quad (3)$$

where V and I is the voltage and current responses in the constant current charging-discharging or cyclic voltammetry measurements, respectively; and m_A and m_B are the masses of the two film electrodes. The typical value of the electrode mass is about 1~ 2 mg. The discharging current density (A/g) is calculated by using I (m_A +m_B)/($m_A m_B$) in CC measurement, and using s*C_{sp} in CV measurement (s is the scanning rate in cyclic voltammetry and C_{sp} is the specific capacitance).

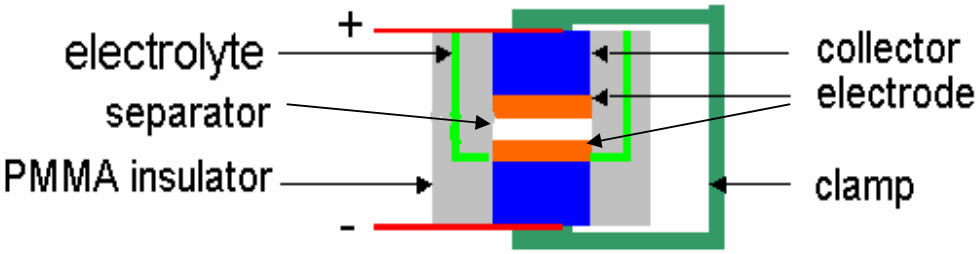

Figure 2.2. Schematic of supercapacitor testing cell.

2.2.6 X-ray Photoelectron Spectra

X-ray photoelectron spectra collection were carried out on Surface Science Model SSX –100 ESCA Spectrometer using Al Kα radiation (hν = 1486.6 eV) operating at an excitation source with a pass energy of 150 eV for general surveys and 50 eV for high resolution surveys. The vacuum in the analysis chamber was about 5 $\times 10^{-9}$ Torr. The spectra analysis was accomplished using ESCA 2000.

2.3 Results and Discussion

2.3.1 TGA Measurement

TGA measurement (Figure 2.3) suggests that, at the end of carbonization process, the total mass loss for PAN, SAN, and SWNTs when heated independently to 700 ºC in an inert environment is 60%, 100%, and 10%, respectively. In the Table 2.1, the experimentally determined residual mass values for various samples are listed. One can see that with increasing SAN content in the composite film, the experimentally measured residue of the carbonized PAN/SWNT/SAN decreases, as expected. The residual weight data is consistent with the fact that SAN completely burns out.

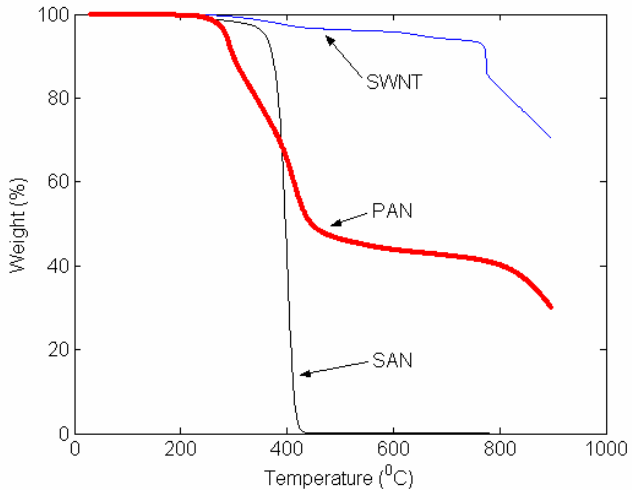

Figure 2.3. TGA analysis of SWNT, SAN and PAN in nitrogen at 5 °C/min to 900 °C.

2.3.2 Morphology

The 100% mass loss of SAN polymer by TGA analysis suggests that simple

stabilization and carbonization treatment of PAN/SWNT/SAN composite films can be used for developing porous SWNT-carbon film without the need for activation. Scanning electron micrographs of a carbonized PAN/SAN film without SWNT and carbonized PAN/SWNT/SAN films are given in Figure 2.4. Carbonized PAN/SAN film without SWNTs exhibits pores in the 1 to 10 μm range. This is a result of SAN domains which have been burned out on carbonization. The surface of the carbonized PAN1-SAN0 film was quite smooth, while the surfaces of carbonized PAN1-SAN10, PAN1-SAN30, PAN1-SAN50, PAN2-SAN30 and PAN3-SAN30 films were quite rough, exhibiting a porous structure. Pyrolysis of SAN domains, which are formed by the phase separation of SAN from PAN matrix due to the immiscibility of styrene segments,[5,6] is responsible for the observed porous structure. Therefore, by controlling the morphology and the size of SAN domains through phase separation conditions, we can develop pore structure controlled SWNT-carbon composite films. In this context, it is also noted that nanostructured carbon arrays from carbonization of an ABA triblock copolymer of acrylonitrile (A) and n-butyl acrylate (B) was recently reported.[7] This further provides the evidence that using the ternary system of SWNT/PAN/sacrificial copolymer can be a general approach to enable development of pore structure controlled SWNT-carbon composite films, which can find applications for electrical energy storage, catalysis and separation membranes.

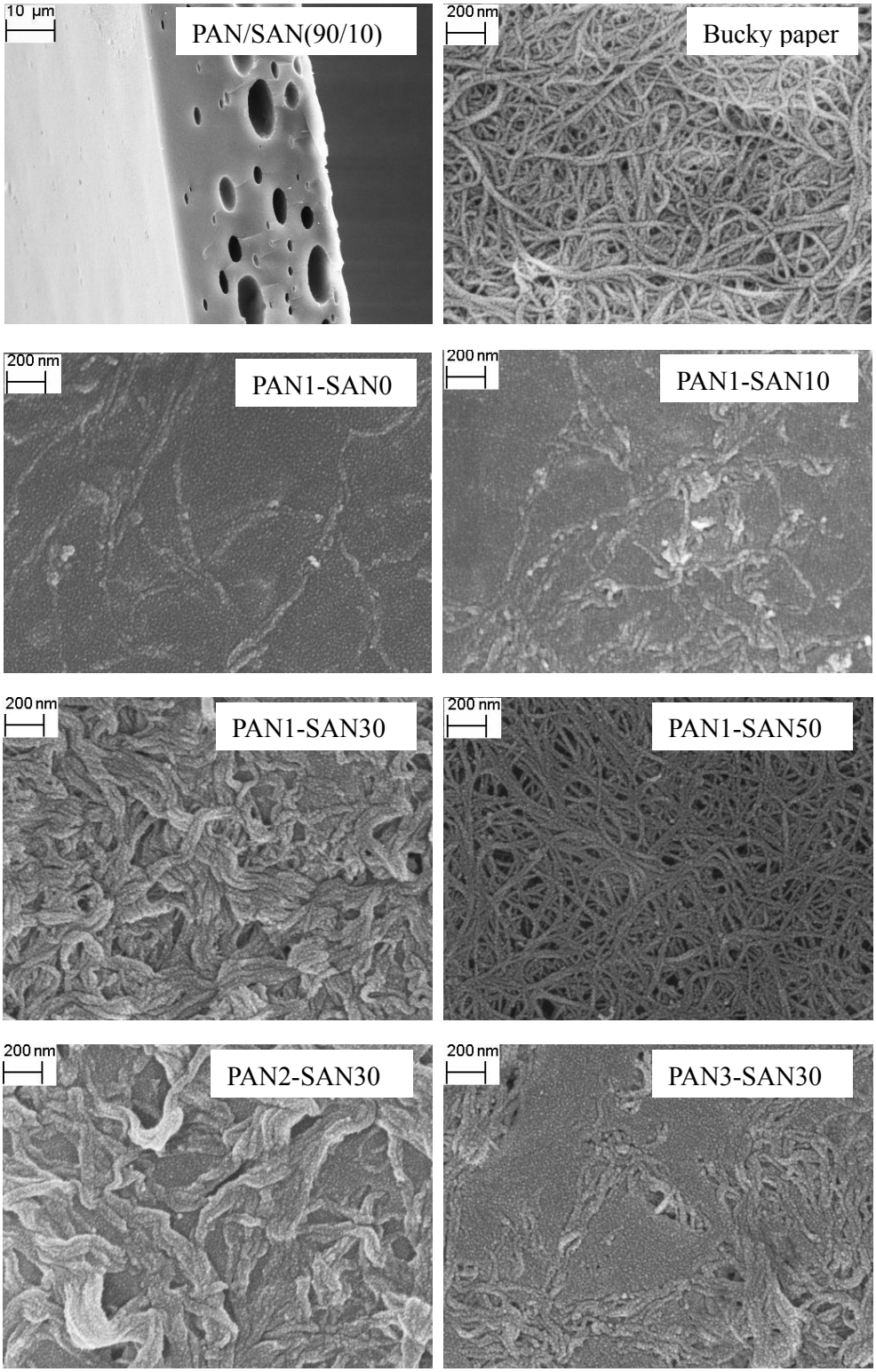

Figure 2.4. Scanning electron micrographs of PAN/SAN, bucky paper, and carbonized PAN/SWNT/SAN films. Sample designations are shown in Table 2.1.

2.3.3 Characterization of Surface Area and Pore Size Distribution

To investigate the effect of composition on the pore structure and the specific surface area of carbonized PAN/SWNT/SAN composite films, isothermal N_2 adsorption at 77 K was carried out on these samples. The N_2 adsorption results for all carbonized PAN/SWNT/SAN films (Figure 2.5) show typical type IV isothermal adsorption behavior.[8] This indicates that relatively large pores exist in the adsorbents. Significant difference in quantity adsorbed is observed with the variation of the composition. The existence of meso-pores (2 nm – 50 nm) is evidenced by the hysteresis of adsorbed quantity of N_2 between the adsorption and the desorption plots at relatively high pressure, which is caused by capillary condensation of N_2 in the meso-pores.[9] The surface area analysis results for all the carbonized samples are given in Table 2.2.

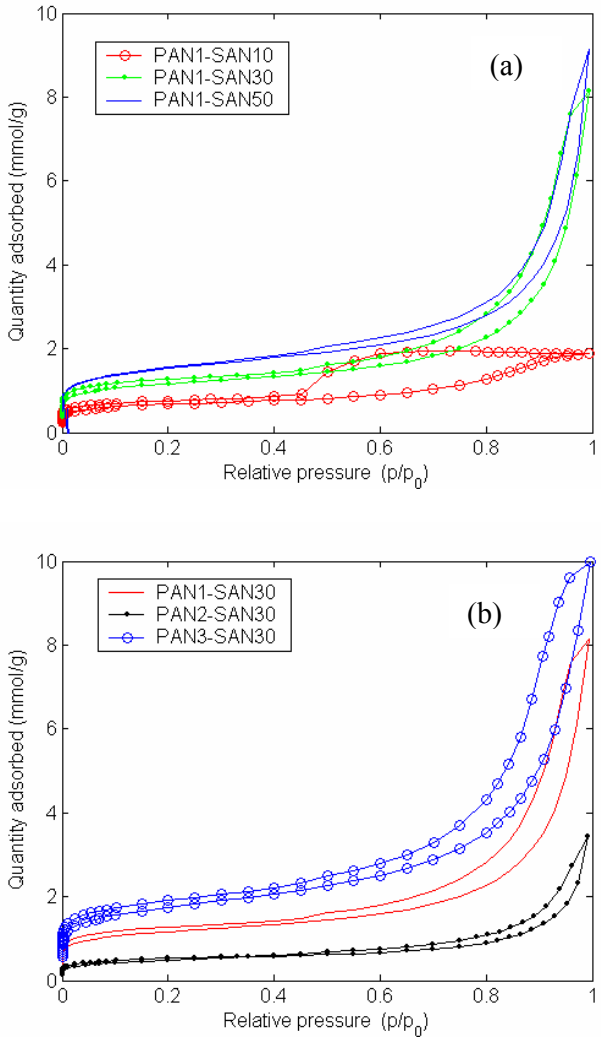

Figure 2.5. Results of isothermal N_2 adsorption (at 77 K) of carbonized PAN/SWNT/SAN composite films. Sample designations are shown in Table 2.1.

Table 2.2. Specific capacitance, surface area, pore volume and double layer capacity of SWNT bucky paper and carbonized PAN/SWNT/SAN composites. Compositions of PAN/SWNT/SAN ternary composite samples are listed in Table 2.1. The pore volume, surface area and pore size can be calculated as shown in Sections 1.7.1 and 1.7.2.

		PAN1-SAN0	**PAN1-SAN10**	**PAN1-SAN30**	**PAN1-SAN50**	**PAN2-SAN30**	**PAN3-SAN30**	**Bucky-paper**
Capacitance (F/g) at 0.1 V		11 ± 1	96 ± 1.2	106 ± 0.7	114 ± 1.2	78 ± 1.3	110 ± 0.4	55 ± 0.1
Capacitance (F/g) at 0.4 V		10 ± 0.3	85 ± 0.7	84 ± 0.2	72 ± 0.3	54 ± 0.4	89 ± 0.2	49 ± 0.1
Capacitance (F/g) at 0.7 V		5 ± 0.5	65 ± 1.6	62 ± 1.1	39 ± 0.4	29 ± 0.3	74 ± 0.3	41 ± 0.1
BET surface area(m^2/g)		16	50	87	115	38	132	546
pore volume(cm^3/g)		0.01	0.07	0.28	0.32	0.12	0.35	0.76
DFT surface area(m^2/g)		5	23	48	60	21	70	297
DFT pore volume(cm^3/g)		0.01	0.06	0.24	0.22	0.09	0.28	0.72
Pore width (nm)		3	5	13	11	13	11	5.6
C_{dl} ($\mu F/cm^2$)	BET	69	192	122	99	205	83	10
	DFT	220	417	221	190	371	157	19

On the basis of DFT model for N_2 adsorption in slit pore of carbon materials,[8] the pore size distribution for all PAN/SWNT/SAN carbonized composite films has been quantitatively determined (Figure 2.6). The dominant meso- and marco-pore

structures (pore size > 2 nm) for these samples is clearly revealed by Figure 2.6. The pore width in carbonized PAN/SWNT/SAN films as quantified by the nitrogen gas adsorption analysis is in the range of 3 to 13 nm, while pores of 2 to 10 μm were observed in PAN/SAN film (Figure 2.4). The average pore size in the SWNT bucky paper was 5.6 nm with a pore volume of 0.76 cm^3/g. The pore size in PAN/SWNT/SAN film containing PAN/SWNT in the 9:1 ratio with 10% SAN was in the 5 to 30 nm range with the maximum pore volume arising from 9 nm wide pores (Figure 2.6b). On the other hand, at the same PAN/SWNT ratio, for 30 and 50% SAN the pore size was in the range of 5 to 200 nm, with maximum pore volume arising from 50 nm wide pores (Figure 2.6b). Figure 2.6c shows the effect of SWNT content on pore size distribution. At low SWNT content, pore size was in the 5 to 200 nm range, and the maximum pore volume was due to 50 nm wide pores, while at a relatively high SWNT concentration (PAN/SWNT ratio 5:1) at 30% SAN, pore size was in the range of 2 to 200 nm and the maximum pore volume was due to 20 nm wide pores. This study suggests that the presence of single wall carbon nanotubes can dramatically alter the phase behavior of polymer blends and attribute this to differences in SWNT interactions with different polymers.[*] The sample containing no SAN, exhibited negligible pore volume (0.01 cm^3/g) and pore volume increased to 0.35 cm^3/g with increasing SAN and SWNT content.

[*] A polymer/carbon nanotube interaction study is given in Appendix A.

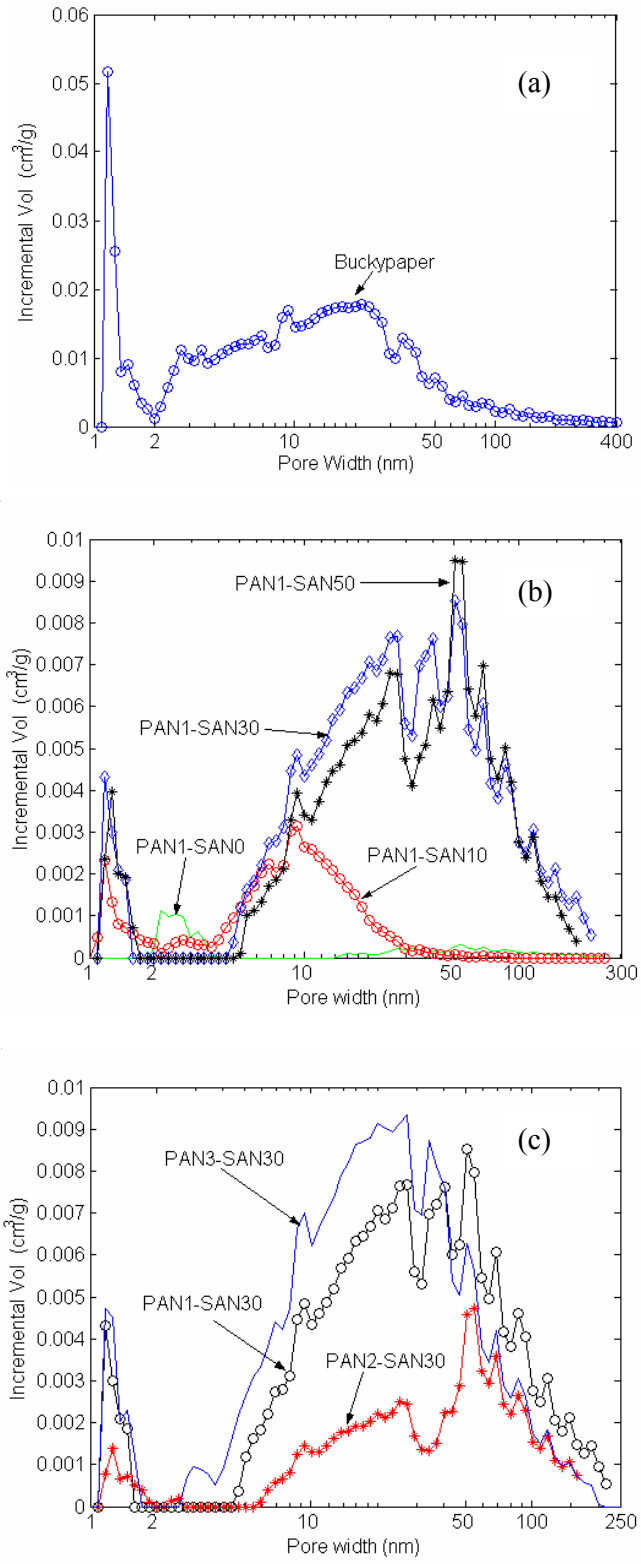

Figure 2.6. Pore size distribution in (a) SWNT bucky paper, (b) and (c) carbonized PAN/SAN/SWNT films. Compositions of carbonized PAN/SAN/SWNT films are listed in Table 2.1.

At a given PAN:SWNT ratio (9:1), surface area and pore volume increased with SAN content (Figure 2.7a). Variation in PAN:SWNT ratio (20:1, 9:1, and 5:1), at a given SAN content (30%) did not result in significant change in the average pore size (11 and 13 nm), while the total pore volume and the surface area did increase with increasing SWNT content (Figure 2.7b). This further suggests that the presence of SWNTs play a significant role in controlling the phase behavior of PAN/SAN blend. The polymer blend morphology in the presence of SWNTs remains largely unexplored, and to the best of our knowledge this is just the first report on a topic that promises to be quite rewarding with many different polymer combinations.

2.3.4 Capacitance Evaluation

The capacitance performance, typical voltage - time response in CC measurement, is shown in Figure 2.8. Similar voltage dependent capacitance behavior was also observed in the carbonized and activated SWNT/PAN film electrodes.[2] The voltage-dependent specific capacitance of PAN/SWNT/SAN composite films is believed to relate to their broad pore size distribution. In addition, the voltage dependence of the electrical double layer capacity and the pseudo-capacitance, [10] which are the major charge storage mechanisms for carbon-based supercapacitor electrodes, might not be neglected either. In Figure 2.9, the cyclic voltammetric curves of all carbonized PAN/SWNT/SAN film exhibit deformed rectangular shape, which may be attributed to the presence of functional groups and/or to broad pore size distribution.

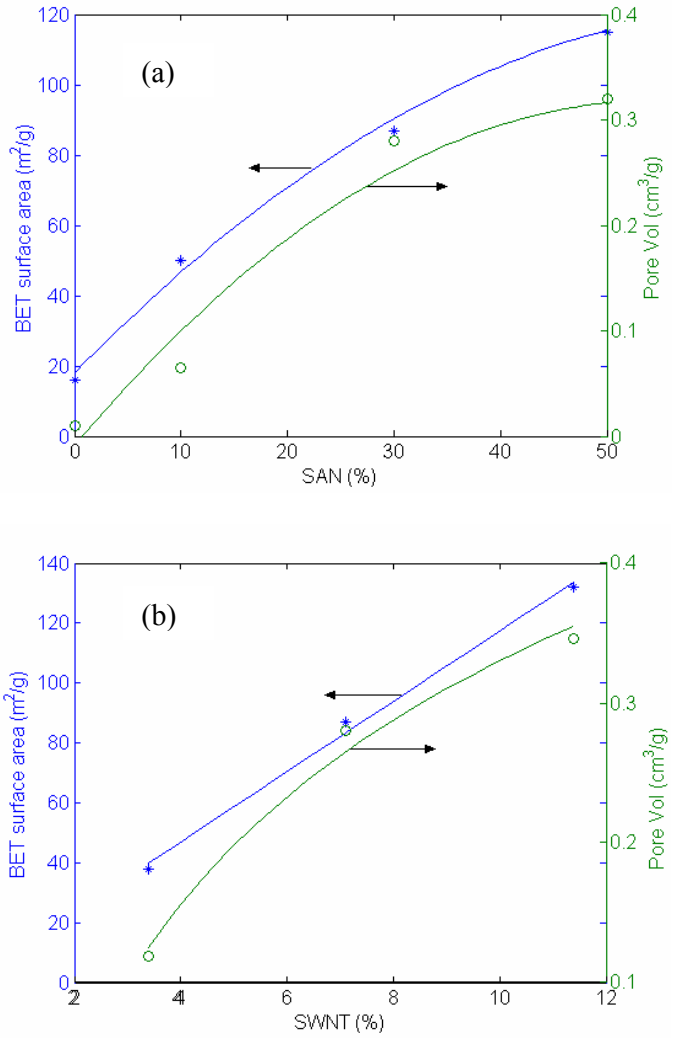

Figure 2.7. Surface area and pore volume of carbonized PAN/SWNT/SAN composite films (a) as a function of SAN content (PAN:SWNT ratio is 9:1), and (b) as a function of SWNT content (SAN content is fixed at 30%).

Current density data obtained at different scan rates at a given voltage (0.1 V) for these ternary composites is plotted as a function of scan rate in Figure 2.10. The slope is constant for most of the samples, except for PAN2-SAN30, which has significantly less SWNT content than other samples. This behavior indicates that suitable SWNT and SAN content are very important to the capacitive behavior of

these systems.

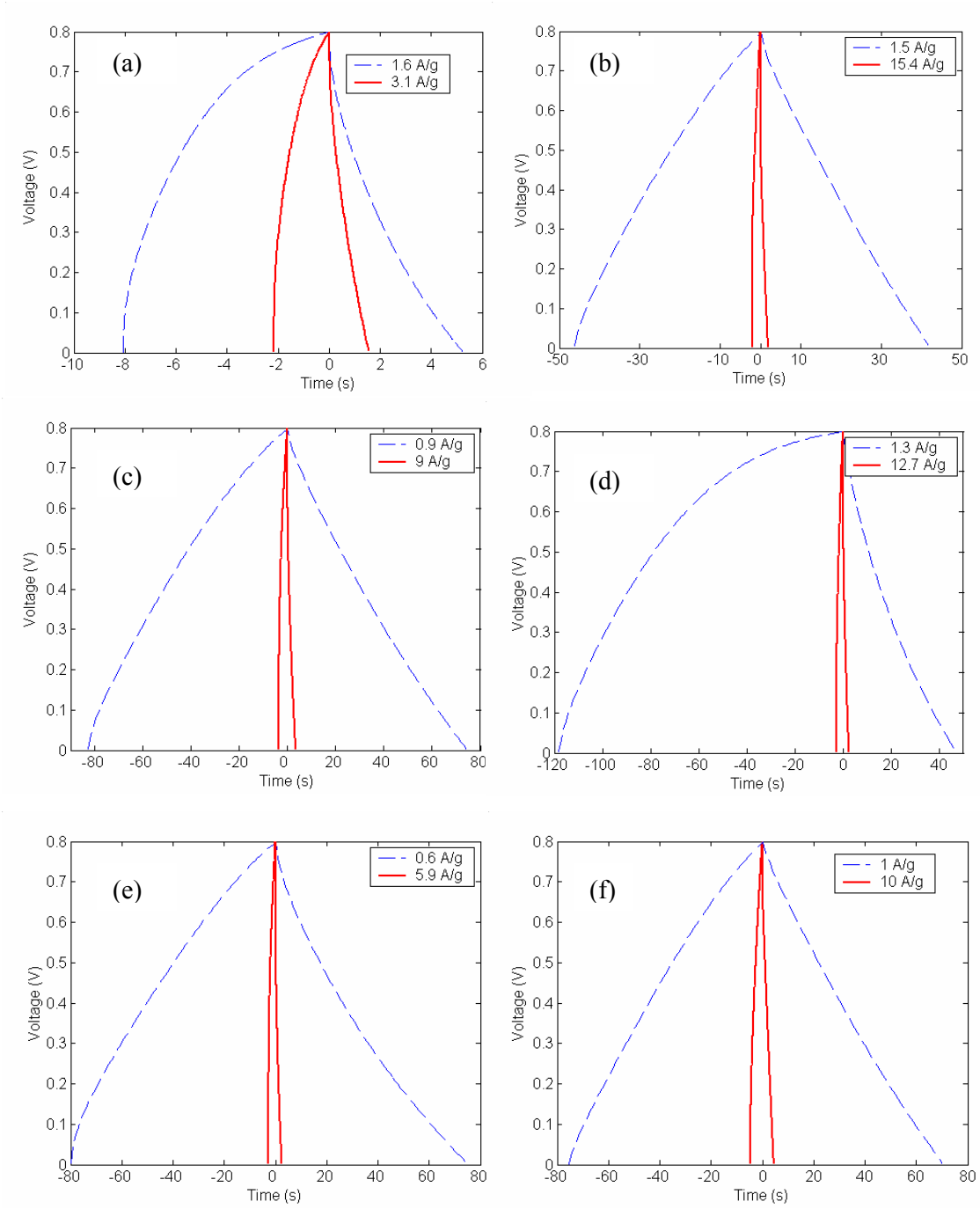

Figure 2.8. Constant current charging/discharging of PAN/SWNT/SAN ternary composite electrodes at two current densities. (a) PAN1-SAN0; (b)PAN1-SAN10; (c)PAN1-SAN30; (d)PAN1-SAN50; (e)PAN2-SAN30; (f)PAN3-SAN30. Sample designations are shown in Table 2.1.

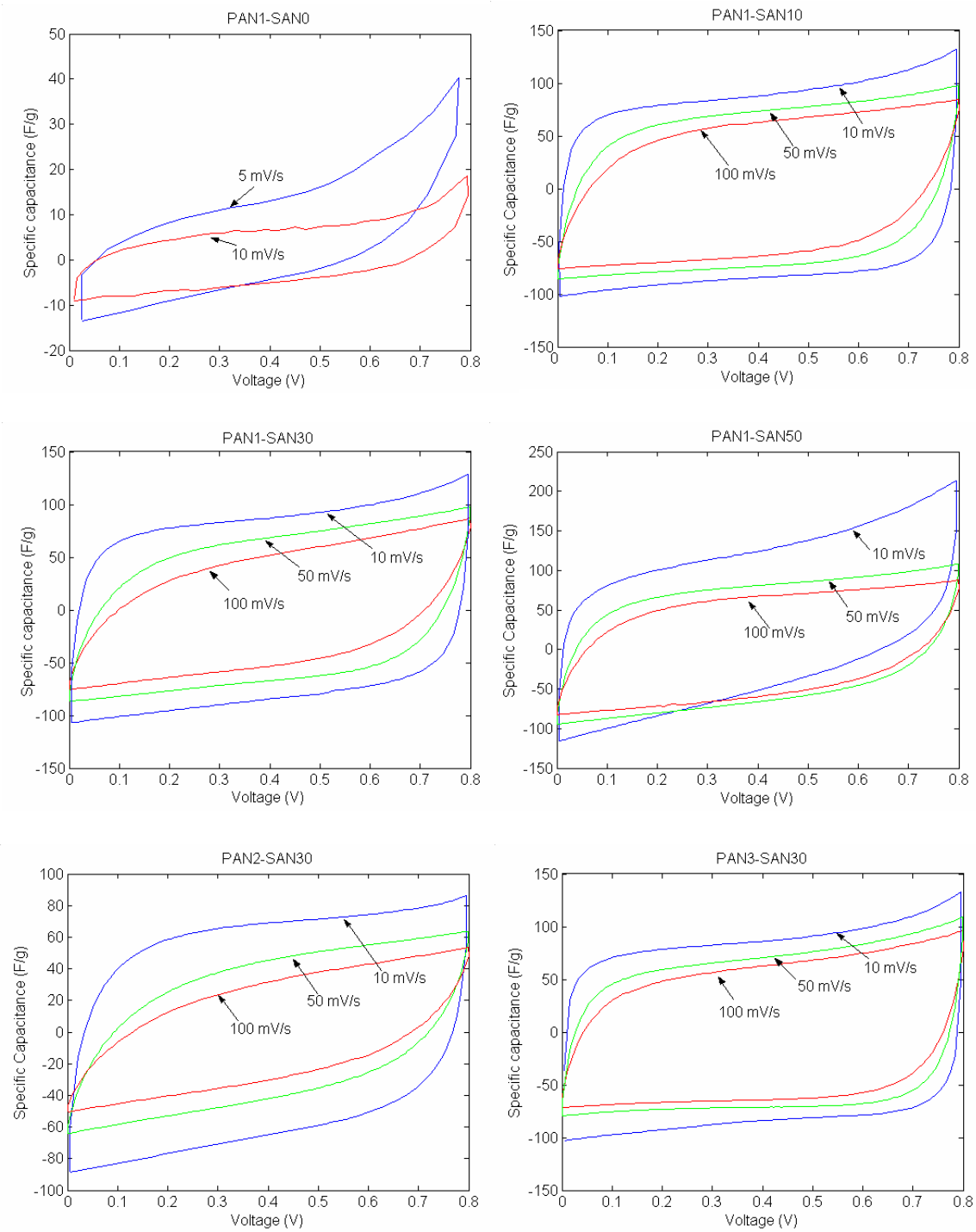

Figure 2.9. Voltammograms at different scan rates of PAN/SWNT/SAN ternary composite electrodes.

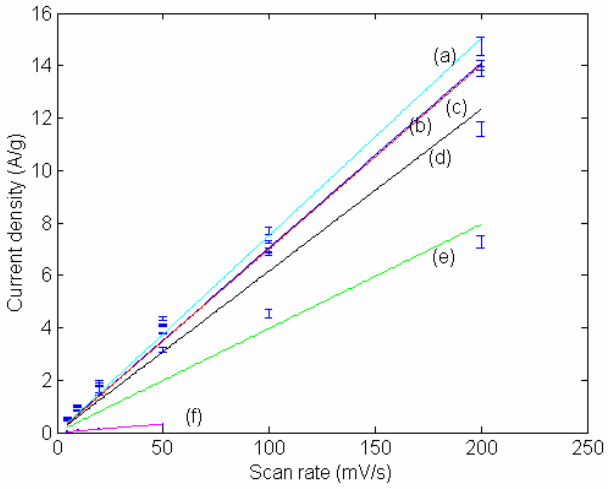

Figure 2.10. Plot of current density as a function of scan rate for PAN/SWNT/SAN ternary composite film. R^2 is the correlation coefficient**.** Low R^2 value indicates significant deviation from linear behavior. The error bar is 3σ. (a) PAN1-SAN50, R^2=0.995; (b) PAN3-SAN30, R^2=0.998; (c) PAN1-SAN10, R^2=0.995; (d)PAN1-SAN30, R^2=0.969; (e)PAN2-SAN30, R^2=0.916; (f) PAN1-SAN0, R^2=0.901.

2.3.5 Capacitance Performance

The plots of specific capacitance vs. discharging current density for various samples at 0.1 V are given in Figure 2.11. At similar discharging current, CC and CV measurement give comparable specific capacitance values. For all the samples, the specific capacitance monotonically decreased with increasing discharging current density. However, the declining rate of the specific capacitance at small discharging current varied from sample to sample. The declining rate for PAN3-SAN30, PAN1-SAN50, and PAN1-SAN10, which have relatively large specific capacitance at high discharging current, is significantly lower than that for PAN1-SAN30 and PAN2-SAN30. Extensive studies[11,12,13,14,15] on the capacitance performance of porous electrodes reveal that, due to the overlapping effect of the electrical double

layer, electrolyte access to the smaller pores is limited. A cut-off pore size of up to several nanometers, depending on the electrolyte concentration and the applied voltage, has been predicted as discussed in Section 1.6.[16] Only those pores larger than the cut-off pore size can be accessed by the electrolyte to form the electrical double layer. Further, the higher resistance of the electrolytes in smaller pores causes slower response to the external electrical stimulation,[10,11,12,13,14,15] preventing the electrical double layer formation. Therefore, the smaller sized pores lose their capacitance contribution at higher current density, resulting in lower capacitance. For this reason, the sample with dominant micro pore size distribution (PAN1-SAN0) has a precipitous decline rate in the specific capacitance. Besides the pore size effect, the pseudo-capacitance contribution by the redox of surface functional groups on the carbonized PAN/SWNT/SAN composite films may also be responsible for the observed discharging current density dependent capacitance performance.[10]

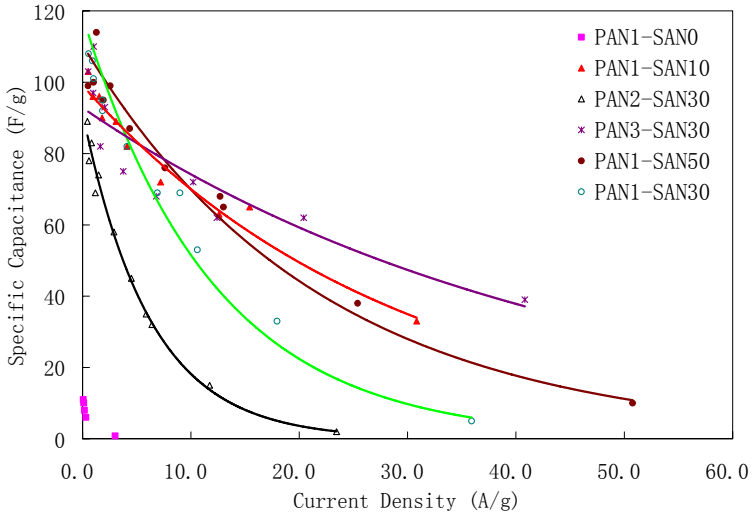

Figure 2.11. Specific capacitance of carbonized PAN/SWNT/SAN composite films evaluated with CC and CV discharging measurement at 0.1 V discharging voltage.

The samples with SAN copolymers have significantly higher capacitance than the sample without SAN. The specific capacitance changes in PAN1 series samples suggest 10 – 30 wt% SAN copolymer concentration in PAN/SWNT/SAN composite film is a better choice than 50 wt% SAN copolymer to optimize the capacitance performance of the carbonized composite film electrodes. The SWNT concentration in the composite film also plays a significant role, which is evidenced by the capacitance comparison of SAN30 series samples. When the SAN polymer concentration is kept at 30 wt%, the specific capacitance of the carbonized PAN/SWNT/SAN composite film with 3.4 wt% SWNT (PAN2-SAN30) is much less than the films with higher SWNT concentration (PAN1-SAN30, 7.1 wt% and PAN3-SAN30, 11.4 wt%). The observed specific capacitance increased with increasing SWNT concentration in SAN30 series samples cannot be attributed to the capacitance contribution by SWNTs, as the C_{sp} of bucky paper - a 100% SWNT bulk film, is only about 40 F/g.[2,17] Considering this fact as well as the important role of SWNT/PAN ratio in determining the different pore structures of carbonized PAN1-SAN30, PAN2-SAN30 and PAN3-SAN30 films, we can infer that existence of SWNTs influences the porous structure development of PAN/SWNT/SAN composite films, which in turn can significantly affect the capacitance performance of the carbonized films.

At low discharging current density, the specific capacitance for PAN1-SAN10, PAN1-SAN30 and PAN3-SAN30 can be as high as 100 F/g at 0.1 V as shown in Figure 2.11. However, the surface area and pore structures of carbonized

PAN/SWNT/SAN composite films are much different, so we may expect that the dominant capacitance contribution from electrical double layer in micro pores at low discharging current are similar among different samples. At high current density, micropores may not be accessed by ions effectively. Nevertheless, different meso- and macro-pore structures among the carbonized PAN/SWNT/SAN films explained the C_{sp} difference at high discharging current. The double layer capacity of the bucky paper is consistent with the double layer capacity of graphite and activated carbons, which are reported to be in the range of 10 to 50 μF/cm^2.[10,18] The double layer capacity of various PAN/SAN/SWNT ternary composite samples are in the range of 83 to 205 μF/cm^2 calculated based on the BET surface area and much higher when calculated based on the DFT surface area (Table 2.2). As compared to SWNT bucky paper, the ternary composites exhibit significantly reduced microporosity (pores <2 nm, Figure 2.6a). The high double layer capacity in the ternary composites, at least in part may be attributed to the reduced microporosity. By comparison, double layer capacity of the recently reported carbonized PAN/MWNT composites, was in the range of 24 to 64 μF/cm^2.[19]

2.3.6 Correlation between Surface Area and Capacitance

As discussed above, the surface area and pore size play an important role in obtaining high specific capacitance. Correlating the specific capacitance and surface area, we find that the capacitance of these carbonized films increases with increasing surface area, but the increase in capacitance is smaller when the surface area is high as

shown in Figure 2.12. However, there is no such relationship between surface area and capacitance in various activated carbon materials.[3] This further reveals that capacitance of carbon materials are affected by many factors, such as pore size and functional groups.

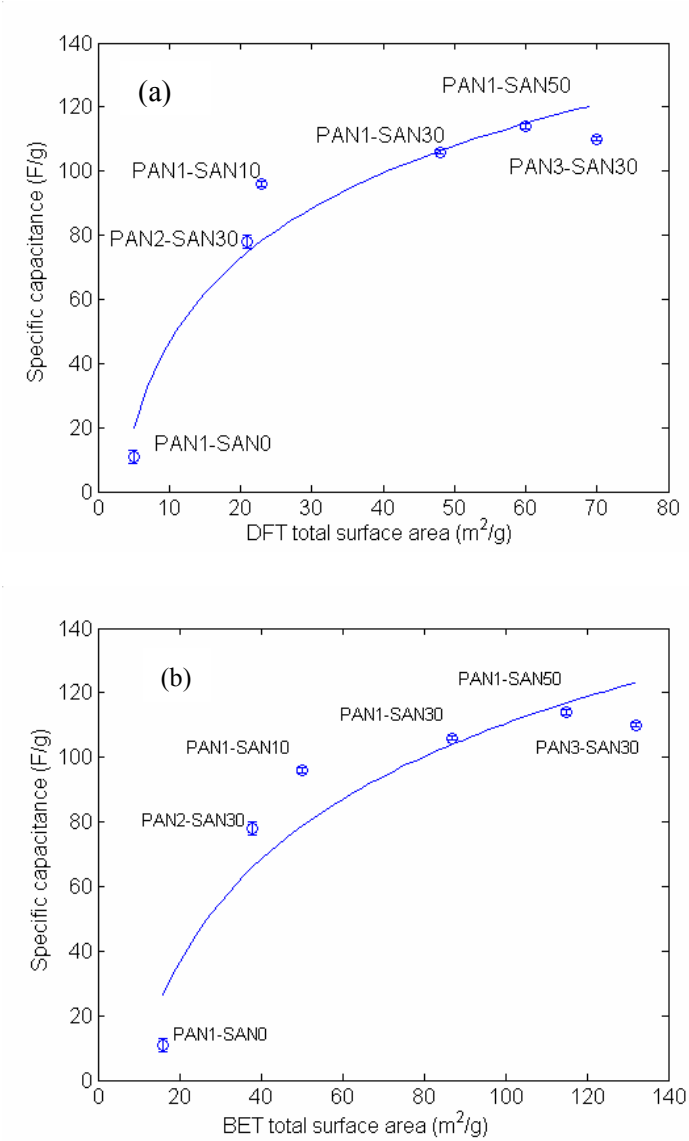

Figure 2.12. Correlation of specific capacitance with total surface area:(a) DFT; (b) BET.

In order to evaluate the long-term performance of carbonized PAN/SWNT/SAN films, PAN3-SAN30 film has been charged and discharged with cyclic voltammetery for 10000 cycles at a scan rate of 20 mV/s. The long term specific capacitances of PAN3-SAN30 (Figure 2.13) decreases with increasing charge/discharge cycles. This decrease is mainly attributed to pseudo-capacitance arising from the presence of functional groups.

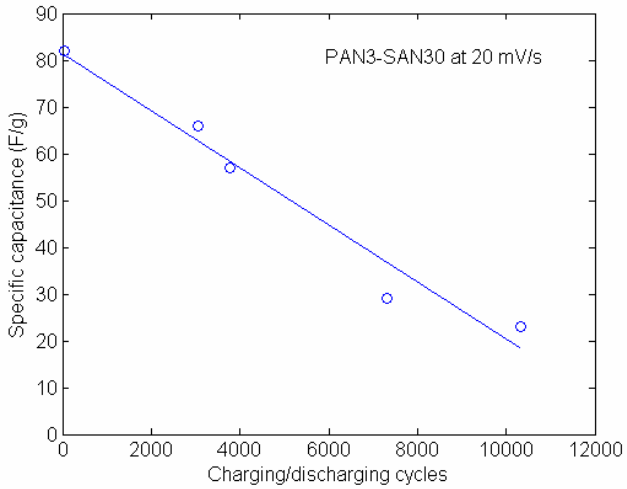

Figure 2.13. PAN/SWNT/SAN long term life performance in 6 M KOH with a scan rate of 20 mV/s.

2.3.7 Characterization of Functional Groups

X-ray photoelectron spectroscopy (XPS) is an effective technique for characterizing surface functional groups.[20,21] The surface atomic composition of the carbonized ternary composites determined by XPS is listed in Table 2.3. All composites samples typically contain 3 to 5 wt% nitrogen and 6 to 15 wt% oxygen. The C1s peak can be resolved into 3 peaks,[22,23] which are C-C at 284.8 eV, C-O

(phenolic, ether) and C-N at 285.8 eV, and C=O (carbonyl or quinone) at 287.2 eV. The concentrations of C-C, C-O (C-N), and C=O groups in these carbonized PAN/SWNT/SAN samples were in the range of 67-78%, 17-24%, and 5-9%, respectively (Figure 2.14). Pyridinic nitrogen is reported to result in the pseudocapacitance behavior,[19] which may partially explain high double layer capacity of the ternary composite samples observed in this work.

Table 2.3. Atomic compositions of PAN/SWNT/SAN carbonized ternary composite films as determined from XPS

	1st measurement			2nd measurement		
	C (%)	**O (%)**	**N (%)**	**C (%)**	**O (%)**	**N (%)**
PAN1-SAN0	85.1	11.5	3.4	87.2	8.4	4.4
PAN1-SAN10	84.7	10.1	5.2	79.6	16.8	3.5
PAN1-SAN30	83.1	14.1	2.8	81.2	17.2	1.7
PAN1-SAN50	89.1	8.5	2.4	92.0	4.6	3.4
PAN2-SAN30	88.5	8.2	3.3	89.9	7.1	3.0
PAN3-SAN30	82.1	15.8	2.1	87.0	7.1	5.8

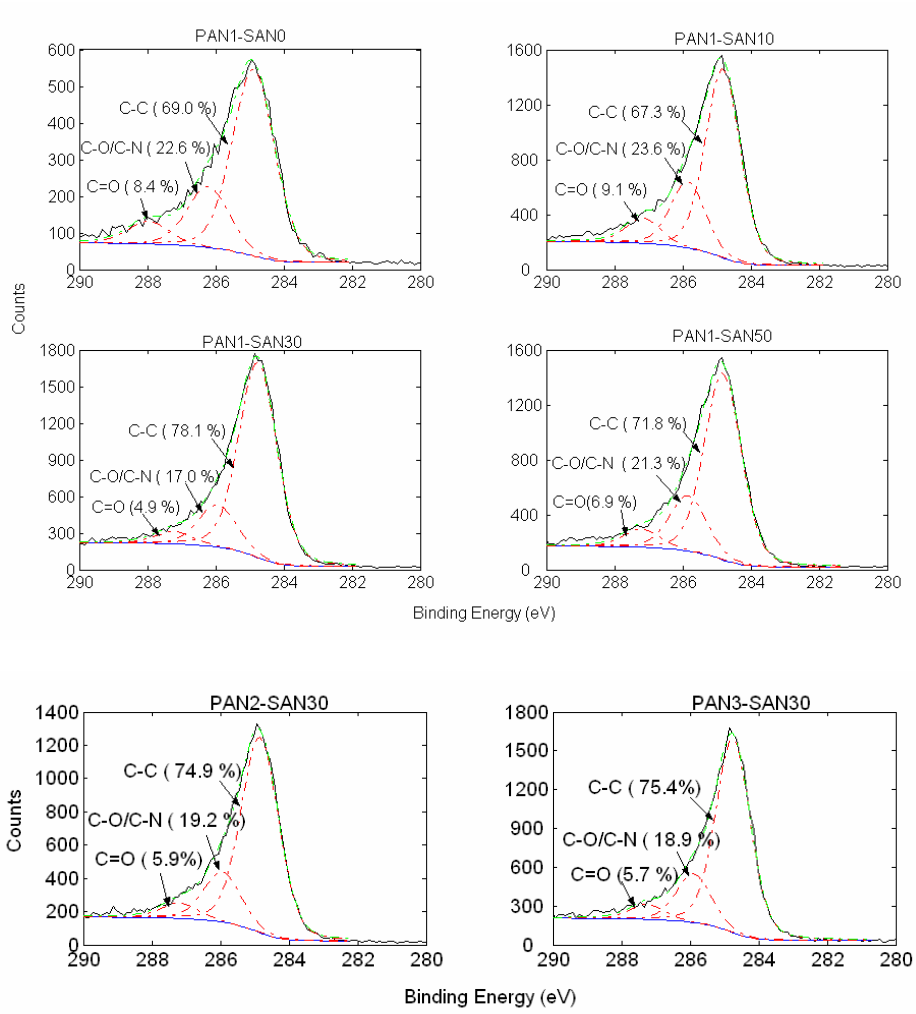

Figure 2.14. XPS spectra of carbonized PAN/SWNT/SAN composite films.

2.3.8 Ragone Plots

A Ragone plot, in which the specific power density and energy density have been empirically plotted against each other on logarithmic scales, is normally used as a performance indicator of an energy storage device. Ragone plots show that the carbonized ternary composite films containing SAN have much higher energy density than those without SAN (Figure 2.15a). Among these samples, PAN3-SAN30 has the highest energy density and power density at higher current (10 mA). The power

density is affected by the conductivity of the films. SWNT can increase the conductivity of the films, so it is not surprising to see that PAN3-SAN30 has highest power density due to its high SWNT content.

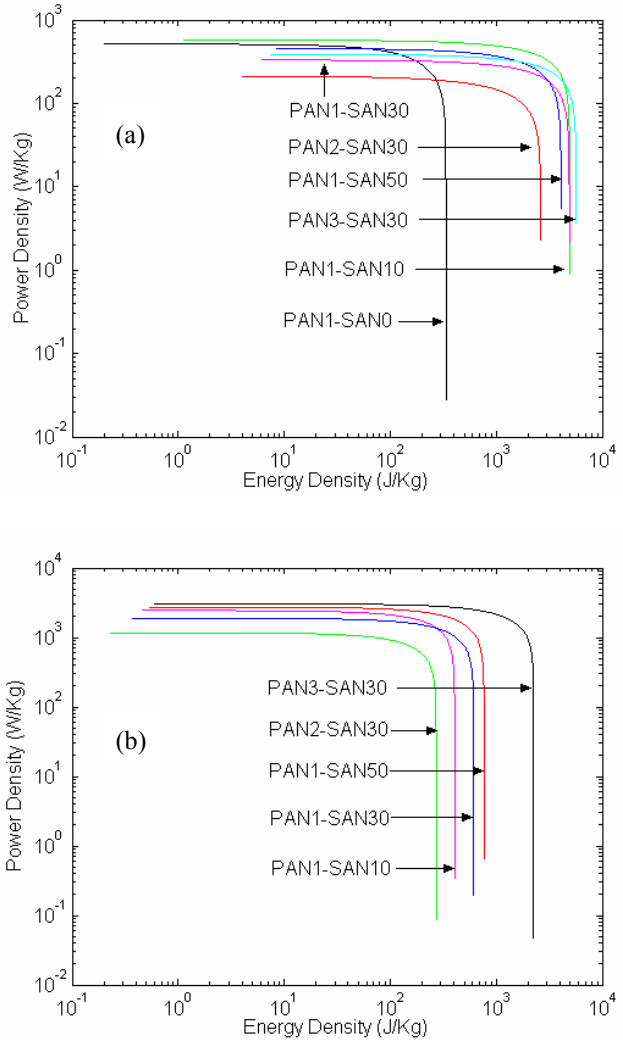

Figure 2.15. Ragone plots of carbonized PAN/SWNT/SAN composite film electrodes at discharging currents of (a) 1 mA and (b)10 mA

2.3.9 Impedance Analysis

The impedance of carbonized PAN/SWNT/SAN film electrodes is shown in Figure 2.16. In 6 M KOH aqueous solution, carbonized PAN/SWNT/SAN film electrode based supercapacitors show a depressed semicircle in the high frequency region, which is indicative of a charge-transfer process. At intermediate frequencies, there is a straight line with a slope of approximately 45° for PAN3-SAN30 based capacitors, which is a common observation for porous carbon materials. In 6 M KOH, it can be seen from the intercepts of curves on the real impedance axis that all these materials show comparable equivalent series resistance which is less than 1 Ω.

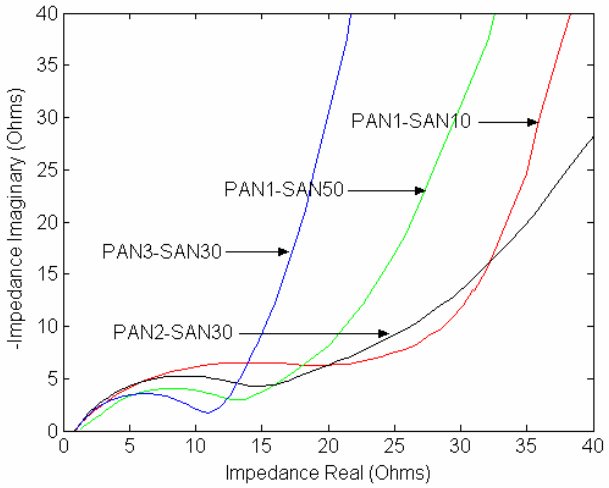

Figure 2.16. Plot of impedance for imaginary vs real component for carbonized PAN/SWNT/SAN films at 6 M KOH.

2.3.10 Application of Electrical Double Layer Model

The electrical double layer model discussed in Section 1.6 takes advantage of all previous models, such as Helmholtz model,[24] Gouy-Chapman model,[25] and

Gouy-Chapman-Stern model,[26] and Grahame model.[27] This electrical double layer model does not fully meet our experimental conditions because high concentration electrolyte (6 M KOH aqueous solution) was used in our evaluation. However, the concept of the cutoff pore size width used in this model is good to explain carbonized PAN/SWNT/SAN film electrodes. In carbonized PAN/SWNT/SAN film electrodes, the double layer capacity is more than 200 $\mu F/cm^2$, which is much higher than activated carbon. For comparison, the double layer capacity of activated carbon is in a range of 10 - 50 $\mu F/cm^2$. In activated carbon, width of most of the pores is less than 1 nm, which is in the range of cutoff pore width, hence most of the pores can not be accessed and double layer capacity is low. However, in PAN/SWNT/SAN film, most of the pores are bigger than 5 nm, which is bigger than the cutoff pore width. Thus in the PAN/SWNT/SAN samples, all the pores can be effectively used, resulting in high double layer capacity.

2.4 Conclusions

A novel process has been developed for preparing carbon-based SWNT composite film electrodes, which involves stabilization and carbonization of a ternary composite film of PAN, SAN and SWNT. Isothermal N_2 adsorption studies indicate that the pore structure of PAN/SWNT/SAN strongly depends on the concentration of SAN co-polymer as well as on the SWNT to PAN ratio. The specific capacitance of greater than 100 F/g for the novel composite film electrodes has been achieved. Extremely high electrical double layer capacity (100 to 200 $\mu F/cm^2$) for the

carbonized PAN/SWNT/SAN is at least partially attributed to the surface functional groups. For comparison, the double layer capacity of activated carbons is in a range of 10- 50 $\mu F/cm^2$.

2.5 References

1 K. H. An, W. S. Kim, Y. S. Park, J. M. Moon, D. J. Bae, S. C. Lim, Y. S. Lee, Y. H. Lee. *Advanced Materials* **2001**, *13(7)*, 497-500.

2 T. Liu, T.V. Sreekumar, S. Kumar, R. H. Hauge, R. E. Smalley. *Carbon* **2003**, *41*, 2440-2442.

3 H. Shi. *Electrochim Acta* **1996**, *41(10)*, 1633-1639.

4 I. W. Chiang, B. E. Brinson, A. Y. Huang, P. A. Willis, M. J. Bronikowski, J. L. Margrave, R. E. Smalley, and R. H. Hauge. *J. Phys. Chem. B* **2001,** *105,* 8297-8301.

5 W. Albrecht, G. Malsch, Th. Weigel, P. Klug, W. Makschin, V. Grobe. *Acta Polymerica* **1992**, *43(2)*, 119.

6 W. Albrecht, P. Klug, W. Makschin, Th. Weigel, H.-J. Gensrich, V. Grobe, D. Paul. *Acta Polymerica* **1992**, *43(3)*,165.

7 T. Kowalewski, N. V. Tsarevsky, K. Matyjaszewski. *J. Am. Chem. Soc.* **2002**, *124*, 10632.

8 P. A. Webb, C. Orr. *Anylytical Methods in Fine Particle Technology*, Micromeritics Instrument Corp. **1997.**

9 K. P. Tzevelekos, E. S. Kikkinides, M. E. Kainourgiakis, A. K. Stubos, N. K. Kanellopoulos, V. Kaselouri. *Journal of Colloid and Interface Science* **2000**, *223(1)*, 89.

10 B. E. Conway. *Electrochemical Supercapacitors, Scientific Fundamental and Technological Applications,* Plenum Publishers, Kluwer Academic, New York, **1999.**

11 Y. Oren, H. Tobias, A. Soffer. *J. Electroanal. Chem.* **1984**, *162(1-2)*, 87-99.

12 Y. Oren, A. Soffer. *J. Electroanal. Chem.* **1985**, *186*, 63-77.

13 Y. Oren, A. Soffer. *J. Electroanal. Chem.* **1986**, *206*, 101-114.

14 D. Golub, Y. Oren, A. Soffer. *J. Electroanal. Chem.* **1987**, *227*, 41-53.

15 D. Golub, A. Soffer. Y. Oren. *J. Electroanal. Chem.* **1989**, *260*, 383-392.

16 K-L. Yang, T-Y. Ying, S. Yiacoumi, C. Tsouris, E. S. Vittoratos. *Langmuir* **2001**, *17*, 1961-1969.

17 J. N. Barisci, G. G. Wallace, D. R. MacFarlane, R. H. Baughman. *Electrochemistry Communications* **2004**, *6*, 22-27.

18 K. Kinoshita. *Carbon Electrochemical and Physicochemical Properties*, John Wiley & Sons, New York, **1988**, p294.

19 F. Beguin, K. Szostak, G. Lota, E. Frackowiak. *Advanced Materials* **2005**, *17*, 2380.

20 M. El-Merraoui, H. Tamai, H. Yasuda, T. Kanata, J. Mondori, K. Nadai, K. Kaneko. *Carbon* **1998**, *36(12)*, 1769.

21 P. V. Samant, F. Goncalves, M. M. A. Freitas, M. F. R. Pereiram, J. L. Figueiredo. *Carbon* **2004**, *42*, 1315.

22 J. Chastain. *Handbook of X-ray Photoelectron Spectroscopy, Perkin-Elmer Corporation, Physical Electronics Division,* Inc. Eden Prairie, Minesota, **1992**, p41.

23 P. H. Wang, K. L. Hong, Q. R. Zhu. *Journal of Applied Polymer Science* **1996**, *62*, 1987.

24 H. Von Helmhlotz. *Ann. Phys.* **1853**, *89*, 211.

25 D. L. Chapman. *Phil. Mag.* **1913**, *25*, 475.

26 O. Stein. *Zeit. Elektrochem.* **1924**, *30*, 508.

27 D. C. Grahame. *Chem. Rev.* **1947**, *41*, 441.

CHAPTER 3

ELECTROCHEMICAL SUPERCAPACITOR BEHAVIOR OF FUNCTIONALIZED SINGLE WALL CARBON NANOTUBES

3.1 Introduction

Carbon nanotubes (CNTs) have unique mechanical, thermal, and electrical properties.[1] However, some chemical modification or functionalization should be applied to take full advantage of these excellent properties in the bulk material.[2,3,4,5] Functionalization was initially used to improve the solubility of nanotubes by opening their ends or side walls.[6,7,8] Functionalization can also introduce reactive moieties to disrupt the rope structure, and to obtain smaller diameter ropes and possibly individual nanotubes.[9] It also can help SWNT separation by chirality.[10]

The functionalization of CNTs proved to be an effective way to develop enhanced capacitance electrodes. The results show that unbundled SWNT can improve the capacitance performance effectively, and high capacitance values (~ 180 and 102 F/g) were obtained,[11,12] while the capacitance of untreated bucky paper membrane is less than 50 F/g.[13,14] This improvement may result from pseudocapacitance contribution induced by the functional groups. Additionally, functionalization enables the achievement of individual nanotube, which generally has higher specific surface area than bundled CNTs. Moreover, functionalization can alter the porous structure of carbon nanotubes.[15,16] The functional groups on

electrodes can also improve the wetting behavior between electrolyte and electrodes.[17]

In this chapter, electrochemical properties of functionalized SWNT electrodes in 6 M KOH aqueous solution and in ionic liquid have been determined. The morphological structure of these electrodes is characterized by N_2 adsorption/desorption, scanning electron microscopy (SEM) and X-ray photoelectron spectroscopy (XPS). The capacitance dependence on various morphological parameters has been discussed.

3.2 Materials and Experiment

3.2.1 Functionalized SWNT Film Preparation

SWNT are functionalized with arylchloride, sodium sulfonate, arylchloride & 4,4'-methylenedianiline, and bis(3,5 -di-tert-butylphenyl)-5-aminobenzene-1,3- dioate by Dr James M. Tour's group at Rice University following the previously reported procedure.[9,13] The compositions and structures of functionalized SWNTs are shown in Table 3.1 and Figure 3.1, respectively.

3.2.2 Contact Angle Measurement

The contact angle was measured on VCA Optima contact angle analysis system (AST Products, Inc.). Other experimental procedures are described in Chapter 2.

Table 3.1. Composition of functionalized SWNT electrodes

	Functional groups	**Functionalized Percentage (%)**
Bucky paper		0
JLH-67	Arylchloride	3.5
JLH –100		4.0
JLH –111		5.9
JLH –103	Sodium sulfonate	----
CDD-I-26	Arylchloride and 4,4’-methylenedianiline	----
CDD-I-76	Bis(3,5 -di-tert-butylphenyl) -5-aminobenzene-1,3-dioate	----

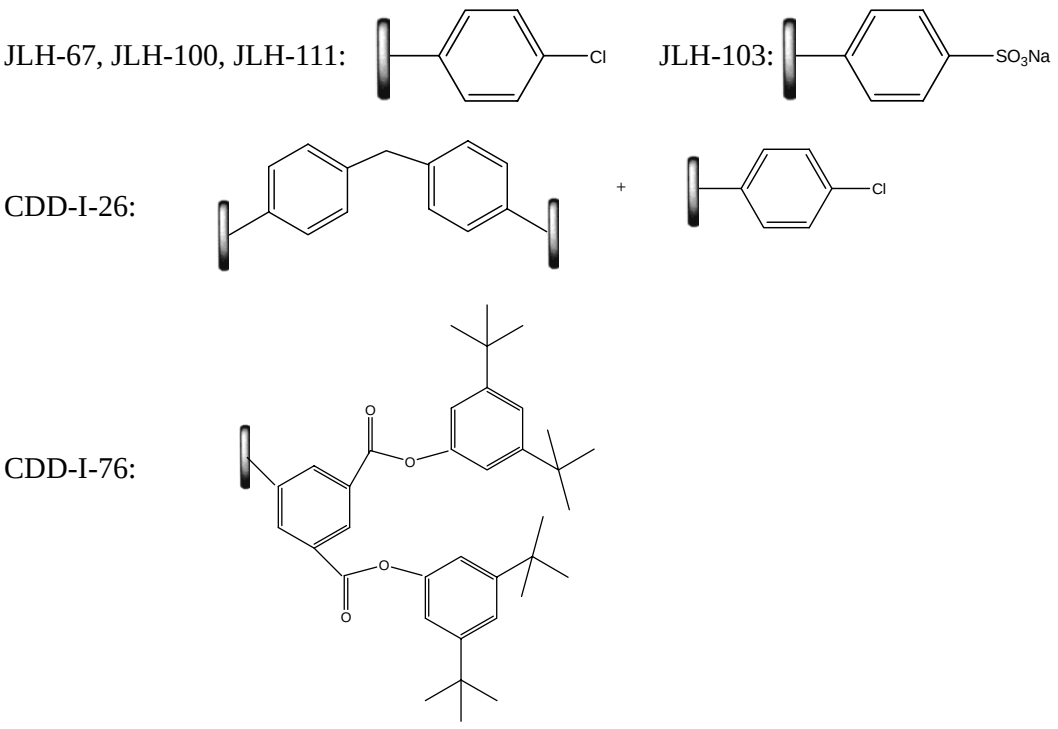

Figure 3.1. The structures of variously functionalized SWNTs.

3.3 Results and Discussion

3.3.1 Morphology Characterization for Arylchloride Functionalized SWNT

Scanning electron microscopy (SEM) was used to examine the morphology of the bucky paper and functionalized SWNTs. Figure 3.2a shows the rough surface of the control bucky paper. The SWNT bundles have diameters about 48 ± 16 nm. While loosely packed thicker bundles are observed in arylchloride membrane JLH-67 (Figure 3.2b). By comparison, JLH-111 (Figure 3.2d) with a higher degree of arylchloride functionality shows a much more compact structure, and the bundles have much smaller diameter than those of JLH-67 and the control bucky paper, while JLH-100 (Figure 3.2c) with intermediate functionality shows the presence of both small and large bundles. This behavior indicates that the functionalization can damage some CNTs and form some amorphous carbon.

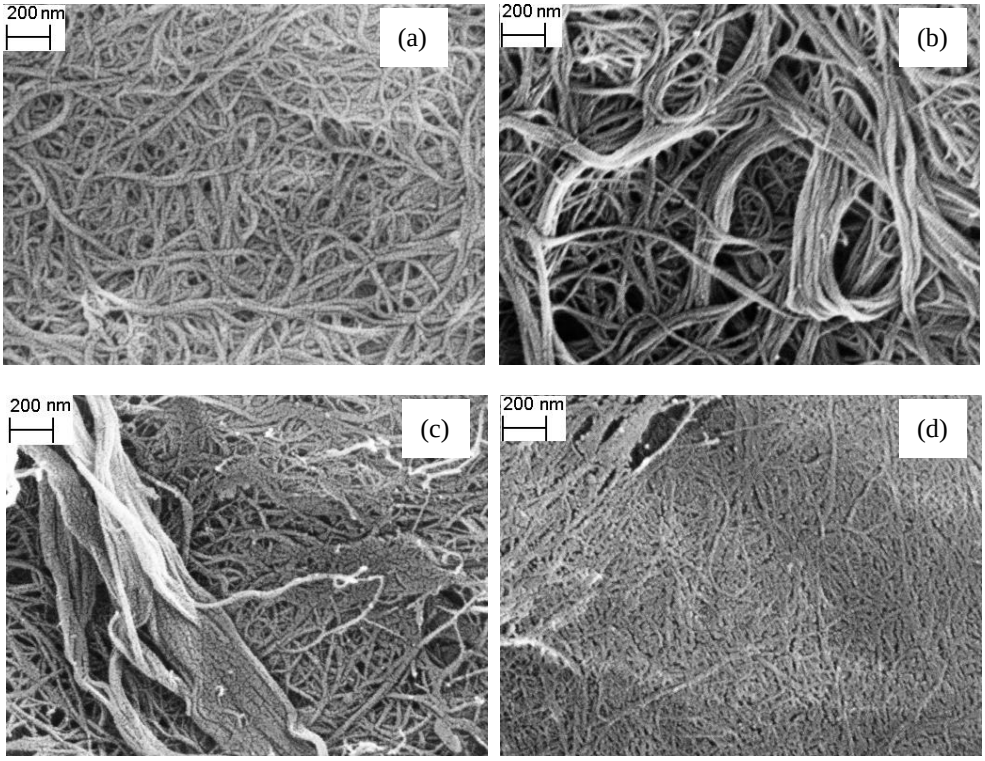

Figure 3.2. Scanning electron micrographs of control bucky paper and functionalized SWNT films. (a) Bucky paper; (b) JLH-67; (c) JLH-100; (d) JLH-111.

3.3.2 Characterization of Surface Area and Pore Size Distribution for Arylchloride Functionalized SWNT

The isothermal adsorption and desorption of bucky paper, JLH-67 and JLH-100 show isotherm type IV behavior which indicates that these membranes have relatively large pores, while JLH-111 shows type V behavior, which indicates that the adsorptive molecules have greater affinity for one another than they do for the functionalized SWNT membranes (Figure 3.3).[18]

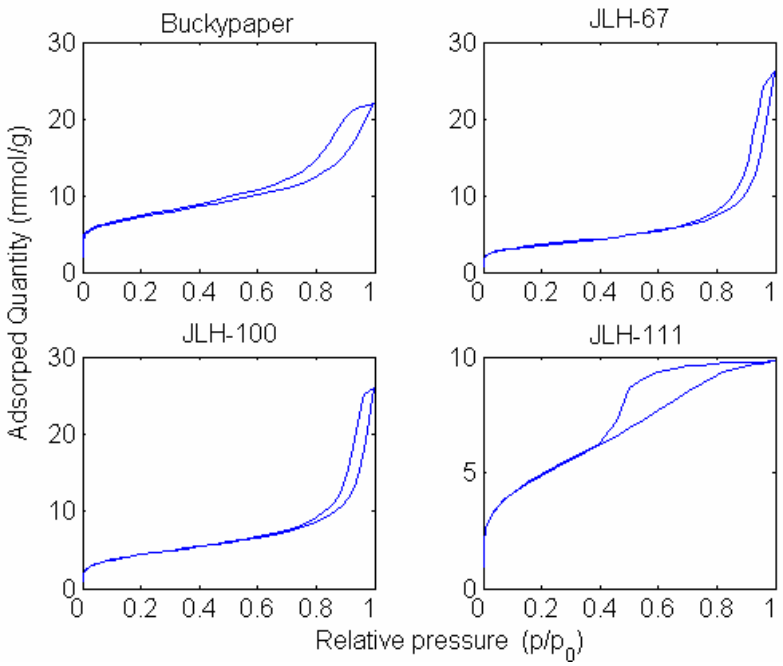

Figure 3.3. Adsorbed N_2 quantity vs. relative pressure of isothermal N_2 adsorption (77 K) for arylchloride functionalized SWNT electrodes with different degree of functionalization .

The pore size and pore size distribution of the control SWNT and functionalized SWNT as determined by DFT method are shown in Figure 3.4. It seems that the functionality not only affects the pore size, but also the pore size distribution. JLH-67 and JLH-100 have relatively larger pores and a broader pore size distribution, from 1 to 300 nm, but JLH-111 has relatively small pores which are less than 10 nm. The narrow pore size distribution of JLH-111 is probably attributed to the amorphous carbon produced by functionalization. More amorphous carbon can be produced because high functionalization degree can destroy more SWNTs.

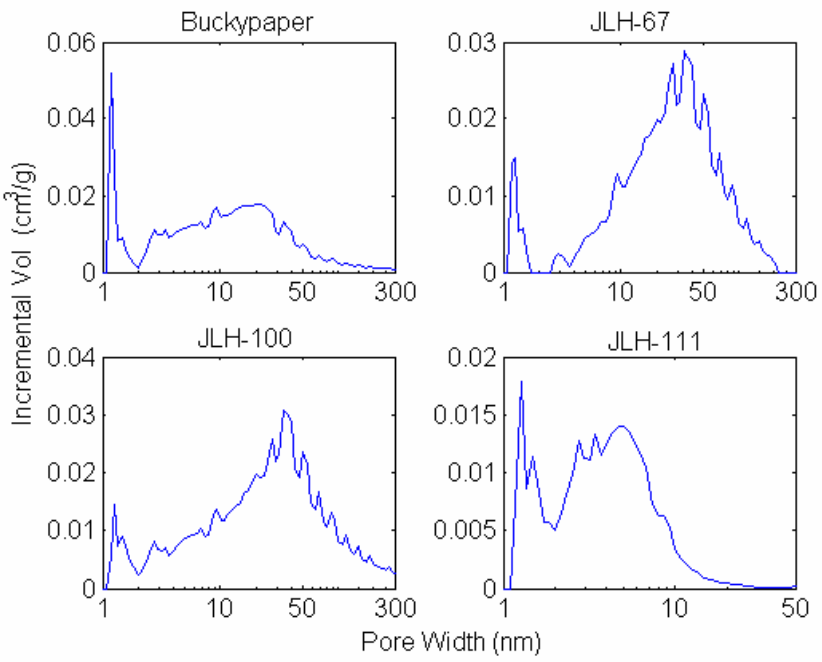

Figure 3.4. Pore size distribution determined by DFT model for arylchloride functionalized SWNT electrodes.

As to the pore volume of these samples, bucky paper, JLH-67, and JLH-100 have comparable values, about 0.76 ~ 0.90 cm^3/g, which is more than two times higher than for the JLH-111. The increased pore size may be due to the enlargement of interstitial pores by intercalation of arylchloride.[19] The surface area of the control bucky paper is at least 20% higher than that of functionalized samples (Table 3.2). Capacitance and various porosity parameters for functionalized SWNTs are summarized in Table 3.2.

Table 3.2. Capacitance, surface area, and various porosity parameters of arylchloride functionalized SWNTs

Discharge current 1 mA		**Bucky paper**	**JLH-67**	**JLH-100**	**JLH-111**
Capacitance (F/g)	0.1 V	**55**	**93**	**74**	**33**
	0.7 V	41	47	38	6
	mean	49	74	53	20
BET surface area (m^2/g)		**546**	**277**	**343**	**392**
Total Pore Volume (cm^3/g)		0.76	0.9	0.9	0.34
DFT surface area (m^2/g)	Total	297	182	189	206
	Micro	167	67	76	98
	Meso	128	75	109	107
	Macro	1.2	40	4	1
DFT Pore Volume (cm^3/g)	Total	0.69	0.70	0.85	0.30
	Micro	0.11	0.04	0.05	0.07
	Meso	0.52	0.52	0.6	0.23
	Macro	0.06	0.14	0.2	0
C_{dl} ($\mu F/cm^2$) (0.1V capacitance)	BET	10	34	21	8
	DFT-Total	19	51	39	16
	DFT-Meso&Macro	43	81	65	30
Average Pore Size (nm)		5.6	13.0	10.5	3.5

* Micro, meso and macro pore refers respectively the pore size of < 2 nm, 2 nm – 50 nm, and > 50 nm.

3.3.3 Capacitance Evaluation for Arylchloride Functionalized SWNTs

The electrochemical supercapacitor behavior was investigated under constant current charging/discharging and cyclic voltammetry with 6 M KOH as electrolytes. The charge/discharge characteristic curves of the functionalized samples at constant current of 1 mA in 6 M KOH are shown in Figure 3.5. Control bucky paper shows linear behavior, while SWNT membranes with arylchloride functional groups (JLH-67, JLH-100, and JLH-111) exhibit nonlinear behavior, which is indicative of the pseudocapacitance induced by the functional groups and/or a very broad pore size distribution, especially for JLH-111. Figure 3.6 shows the cyclic voltammetry plots at scan rates of 10, 20 and 50 mV/s. Control bucky paper shows ideal rectangular shape, while functionalized samples show deformed rectangular shape. The behavior indicates the existence of redox reactions due to functional groups.

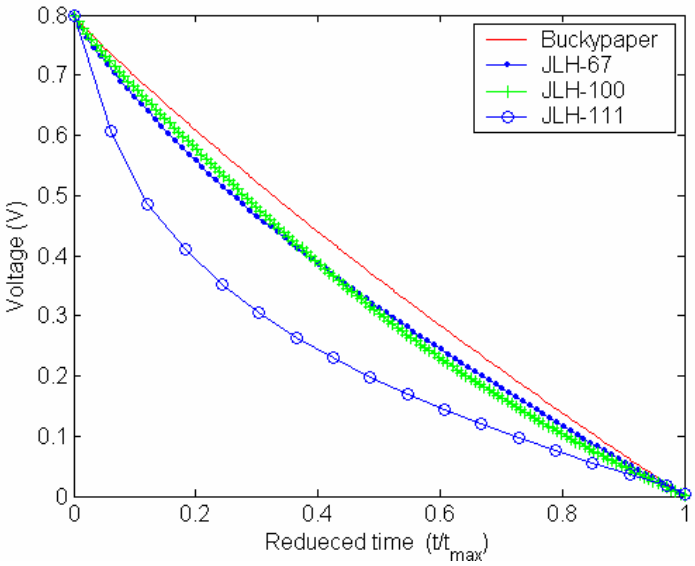

Figure 3.5. Constant current charge/discharge characteristic of SWNT with same functional groups.

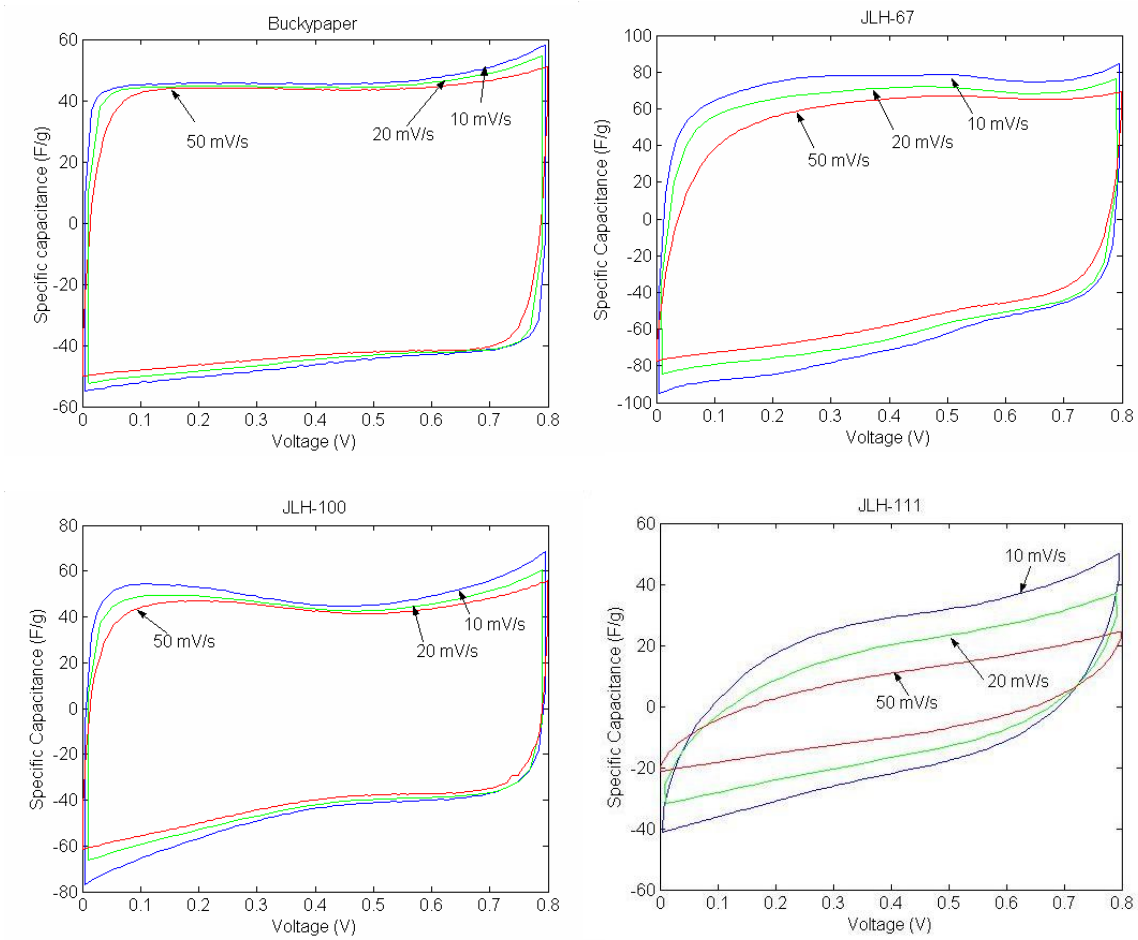

Figure 3.6. Cyclic voltammetry characteristic of SWNT with same functional groups.

The current densities at 0.1 V were plotted as a function of scan rate as shown in Figure 3.7. The correlation coefficient of the linear fit for JLH-111 is much lower than that for the other three samples. This indicates that redox reaction in JLH-111 is much more significant than other samples.

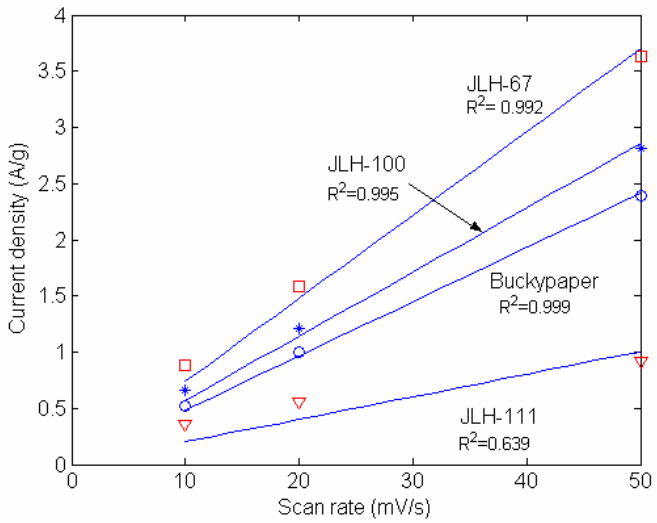

Figure 3.7. Plot of current density as a function of scan rate for arylchloride functionalized SWNT. R^2 is the correlation coefficient.

The specific capacitance of SWNT membranes with arylchloride groups as a function of current density was examined as shown in Figure 3.8. The capacitance performance of JLH-67 is much better than those of the other two functionalized SWNT and control SWNT bucky paper membranes. The capacitance of JLH-67 is still higher than 80 F/g even at a current density of 6 A/g. The higher degree of functionalization results in sharp drop in specific capacitance at rather low current density. The dramatic drop in capacitance even at low current density for JLH-111 is attributed to the fact that most of the pores in JLH-111 are less than 10 nm, which can't be accessed effectively by ions at high current density. As one can see from the scanning electron micrographs of JLH-111, it seems that nanotubes in JLH-111 are destroyed into amorphous carbon, so they form a very compact structure without any network. On the other hand, too many functional groups will block the pores, so

pores are becoming smaller and smaller. Thus, the pores are smaller than those in the samples with lower degree of functionalization. Therefore, we conclude that too higher degree of functionalization will deteriorate the specific capacitance of the CNT, although the introduction of moderate number functional groups is good for capacitance. Besides the surface area and functional groups on the electrodes, the affinity between electrode and electrolyte is also a very critical issue in the supercapacitor. The contact angles of these functionalized SWNT and control SWNT membranes are listed in Table 3.3. The contact angles of JLH-67, JLH-100 and JLH-111 in 6 M KOH are in the range of 30 to 40°. This is much lower than that for the control bucky paper, which has a value of 100°. Based on these data, we conclude that the affinity of SWNT to 6 M KOH aqueous electrolyte is improved by functionalization.

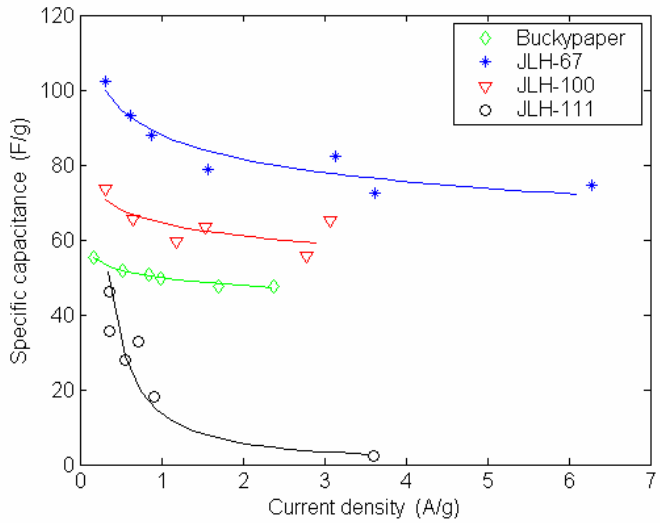

Figure 3.8. Specific capacitance as a function of discharge current density in 6 M KOH for arylchloride functionalized SWNTs.

Table 3.3. Contact angles of 6 M KOH on functionalized SWNT electrodes

	6 M KOH	**BMIMBF4**
Bucky paper	101 ± 3	21 ± 4
JLH-67	38 ± 2	< 10
JLH-100	29 ± 5	20 ± 3
JLH-111	40 ± 6	23 ± 2
JLH-103	82 ± 6	< 10
CDD-I-26	38 ± 8	< 10
CDD-I-76	59 ± 5	N/A

3.3.4 Relationship between Surface Area and Capacitance for Arylchloride Functionalized SWNTs

The relationship between the porous surface area of these functionalized SWNTs and their specific capacitance can be viewed in Figure 3.8. The specific capacitance is plotted as a function of total surface area, meso surface and macro surface area, respectively. The specific capacitance does not increase with total surface area (Figure 3.8a), neither it does with meso surface area (Figure 3.8b). However, the specific capacitance shows proportionality to marco surface area for control SWNT and arylchrolide functionalized SWNT membranes as shown in Figure 3.8c. It is well known that the double layer capacity is not same for all porous carbon surfaces. Secondly, the porous structure of the carbon materials directly controls quick accessibility to the stored energy on the interface. These results

illustrate the relative importance of the macro surface area in obtaining the desired large double layer capacitance value.

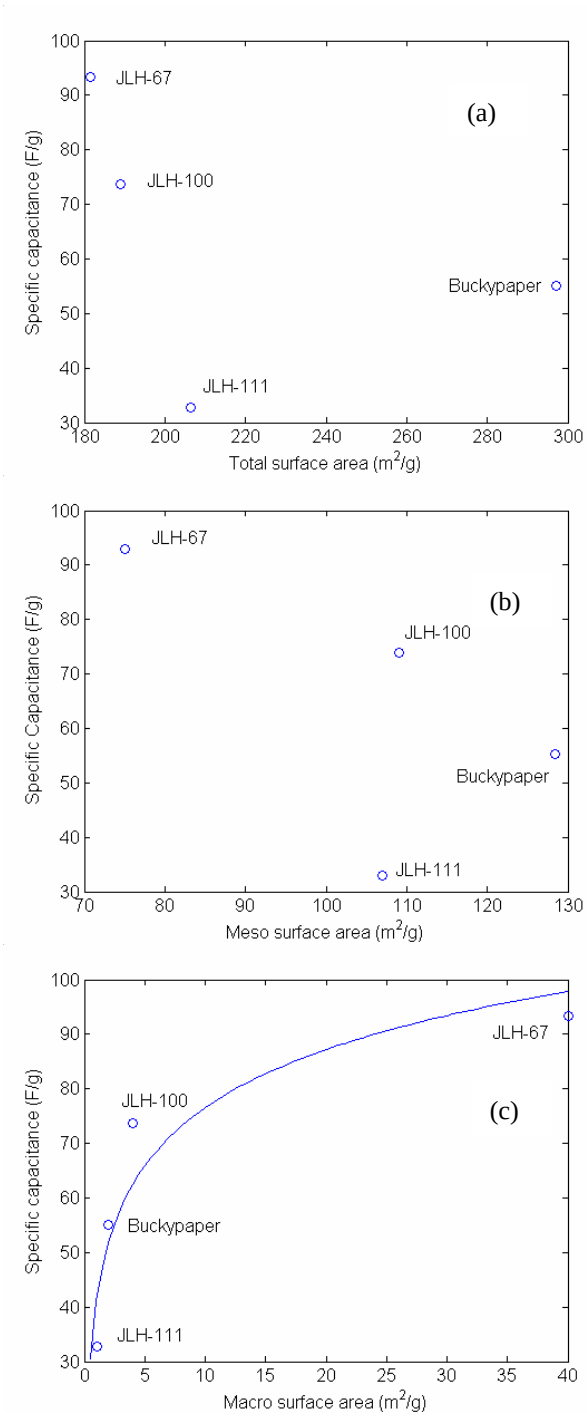

Figure 3.9. (a) Specific capacitance in 6 M KOH vs. total surface area (b) Specific capacitance in 6 M KOH vs. meso surface area; (c) Specific capacitance in 6 M KOH

vs. macro surface area for control SWNT and functionalized SWNT membranes with arylchloride.

3.3.5 Morphology Characterization of SWNTs with Different Functional Groups

Different functional groups are important for improving capacitance performance. It is observed that the surface of JLH-103 (Figure 3.9a) is rougher than that of CDD-I-26 (Figure 3.9b). However, no bundles are observed in CDD-I-76 (Figure 3.9c), in which SWNT was functionalized by a relatively large-structure chemical compound, bis(3,5-di-tert-butylphenyl)-5- aminobenzene-1,3-dioate.

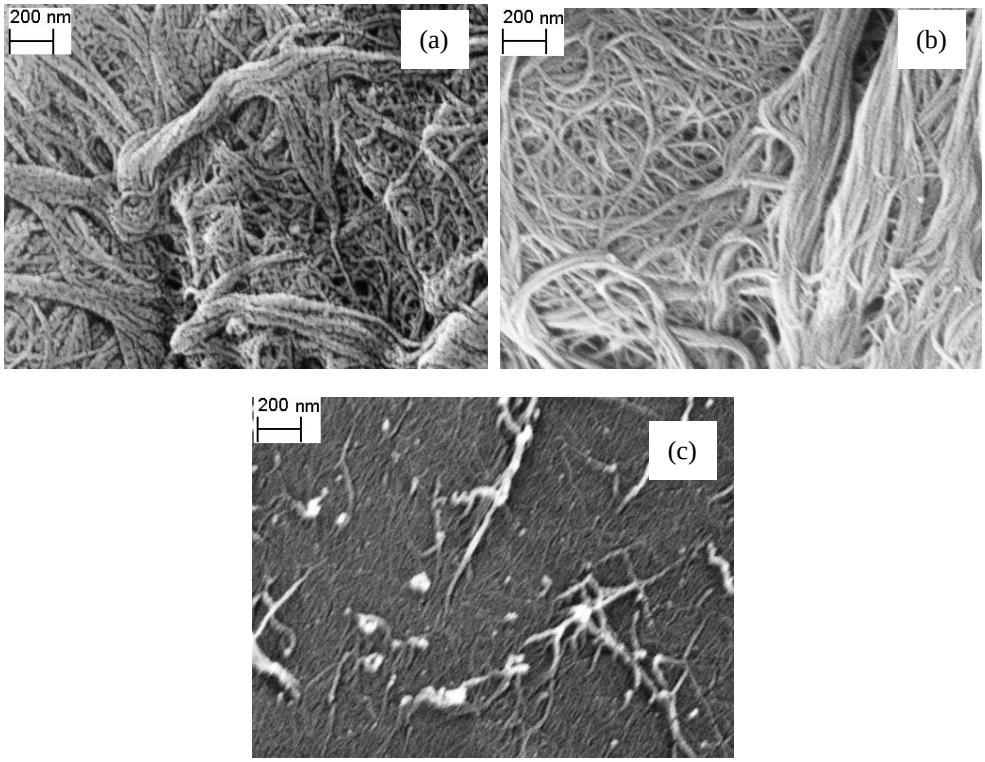

Figure 3.10. Scanning electron micrographs of functionalized SWNT films. (a) JLH-103; (b) CDD-I-26; (c) CDD-I-76.

3.3.6 Surface Area and Pore Size Characterization for SWNT with Different Functional Groups

The SWNTs functionalized with different functional groups were also tested with N_2 adsorption and desorption at 77 K as shown in Figure 3.10. JLH-103 and CDD-I-26 exhibit similar curve as that for the control bucky paper, which is type IV, while CDD-I-76 shows type V behavior. Change of adsorption of CDD-I-76 is mainly due to its bigger size functional groups. The specific surface areas are in the order of bucky paper > CDD-I-76 > JLH-103 > CDD-I-26 based on BET model, while they are somewhat different if calculated using DFT (Table 3.4). CDD-I-76 and JLH-103 have lower pore volume compared to CDD-I-26 as shown in Table 3.4.

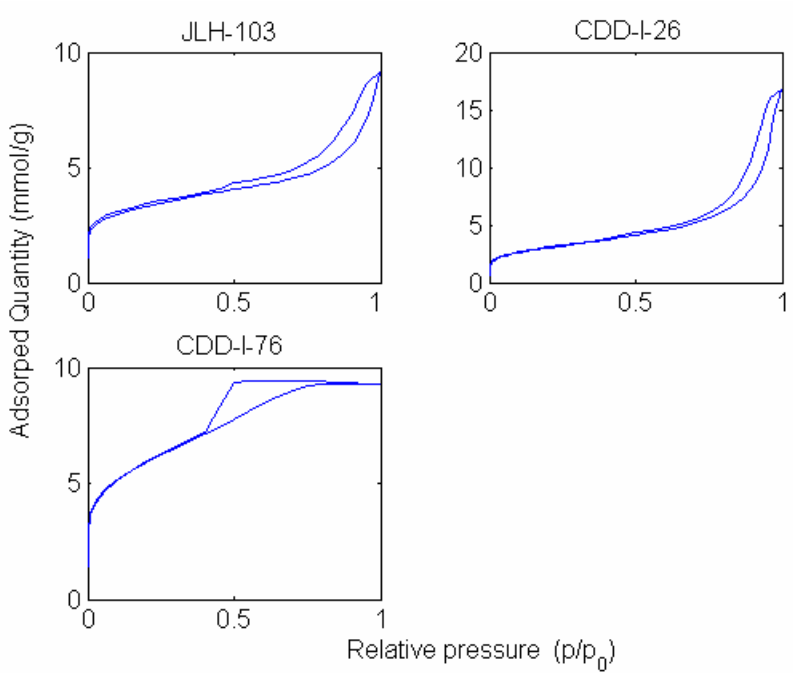

Figure 3.11. Nitrogen adsorption as a function of partial pressure for variously functionalized SWNTs.

Table 3.4. Capacitance, surface area, and capacity of functionalized SWNT electrodes

Discharge current 1 mA		**Bucky paper**	**JLH-103**	**CDD-I-26**	**CDD-I-76**
Capacitance (F/g)	0.1 V	**55**	**49**	**70**	**53**
	0.7 V	41	31	37	32
	Mean	49	39	53	46
BET surface area (m^2/g)		**546**	**249**	**234**	**455**
Total Pore Volume (cm^3/g)		0.76	0.32	0.58	0.3
DFT surface area (m^2/g)	Total	**297**	**120**	**142**	**233**
	Micro	167	67	55	139
	Meso	128	36	65	94
	Macro	2	17	22	0.0
DFT Pore Volume (cm^3/g)	Total	0.69	0.21	0.48	0.3
	Micro	0.11	0.04	0.04	0.1
	Meso	0.52	0.15	0.38	0.2
	Macro	0.06	0.02	0.06	0.0
C_{dl} ($\mu F/cm^2$) (0.1V capacitance)	BET	**10**	**20**	**30**	**12**
	DFT-Total	19	41	49	23
	DFT-Meso&Macro	42	93	80	57

* Micro, meso and macro pore refers respectively the pore size of < 2 nm, 2 nm – 50 nm, and > 50 nm.

CDD-I-76 has a relatively narrow pore size distribution and relatively small pore sizes, which are in the range of 1 to 10 nm. Other materials including the control SWNT show a broad pore size distribution from 1 to more than 200 nm (Figure 3.11). In JLH-103 and CDD-I-76, most surface area is from pores less than 2 nm. CDD-I-26 has relatively larger pores as compared to JLH-103 and CDD-I-76, which are easily accessed by the electrolyte ions particularly at high current density.

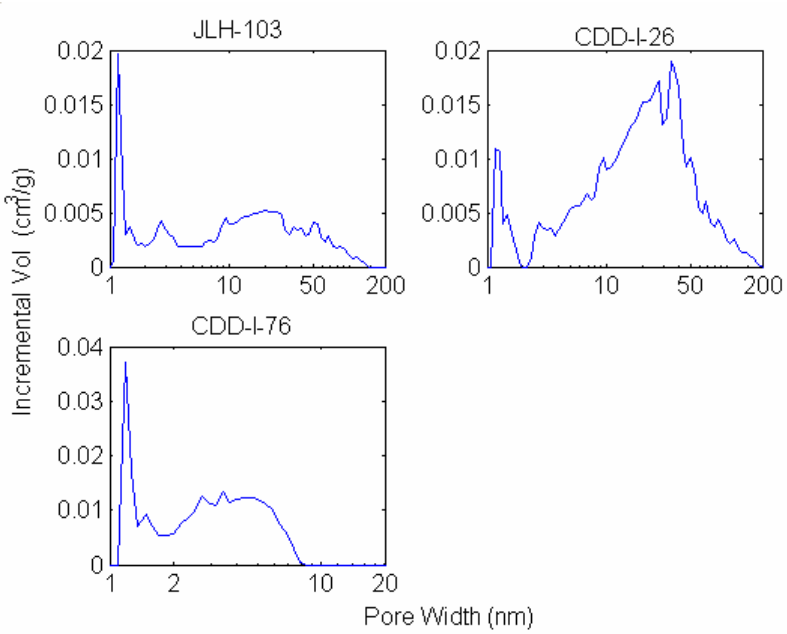

Figure 3.12. Pore size distribution determined by DFT model for arylchloride functionalized SWNT electrode.

3.3.7 Capacitance Characterization for SWNT with Different Functional Groups

The capacitance evaluation was performed in 6 M KOH aqueous solution via constant current charging/discharging and cyclic voltammetry. The plot of voltage as a function of reduced time is almost linear in the constant current discharge in

Figure 3.12. The behavior is very similar to other functionalized SWNTs discussed in previous sections. Nearly rectangular shape has been observed for the cyclic voltammetry of functionalized SWNT with different functional groups (Figure 3.13). The current densities at 0.1 V were collected at different scan rates for these membranes and were plotted as a function of scan rate as shown in Figure 3.14. Linear plots have been observed, which means that overall redox reactions in these materials are not significant.

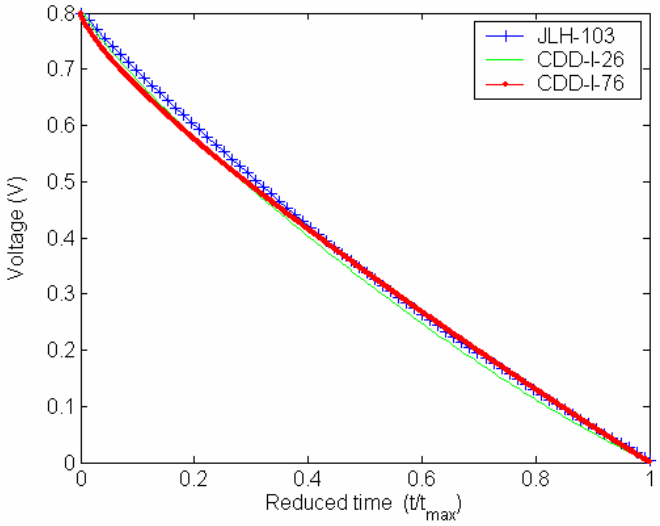

Figure 3.13. Constant current discharge characteristics of SWNT with different functional groups in 6 M KOH. The current is 1 mA.

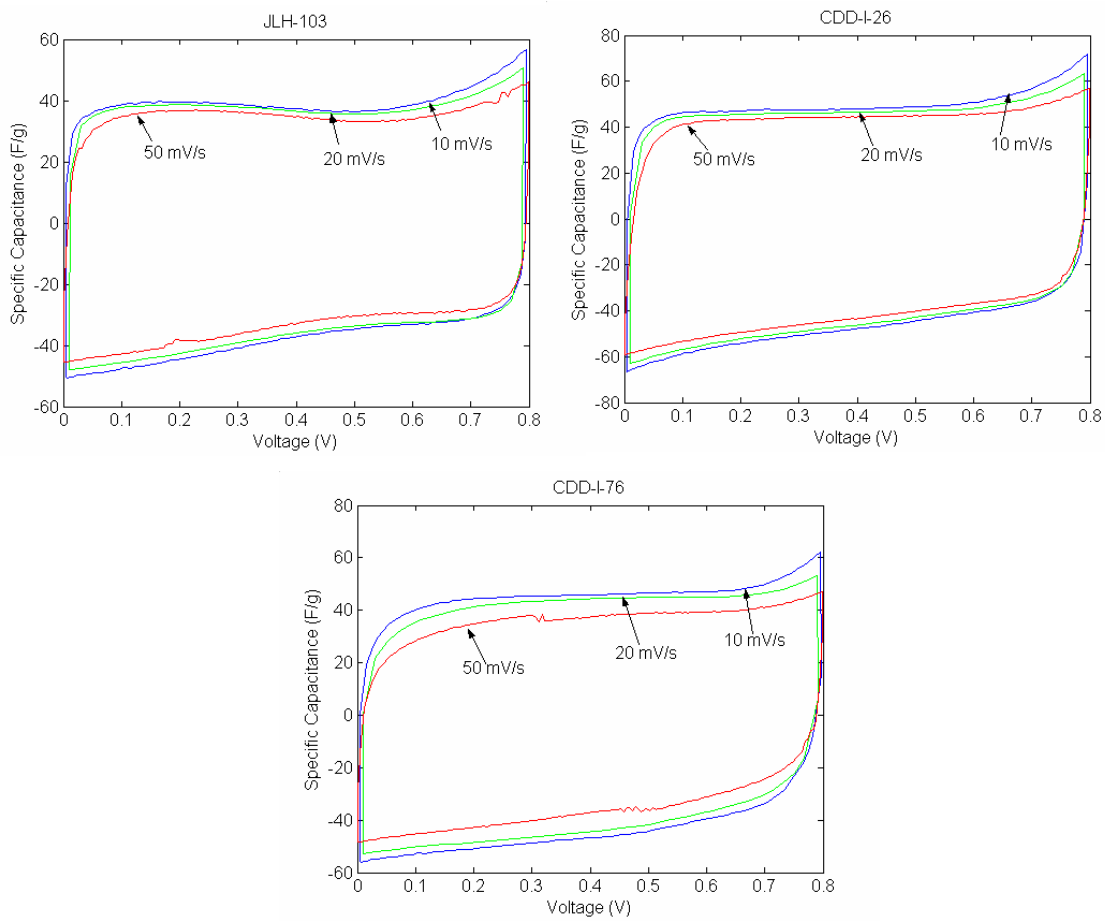

Figure 3.14. Cyclic voltammetry characteristic of supercapacitors based on functionalized SWNT at different scan rates.

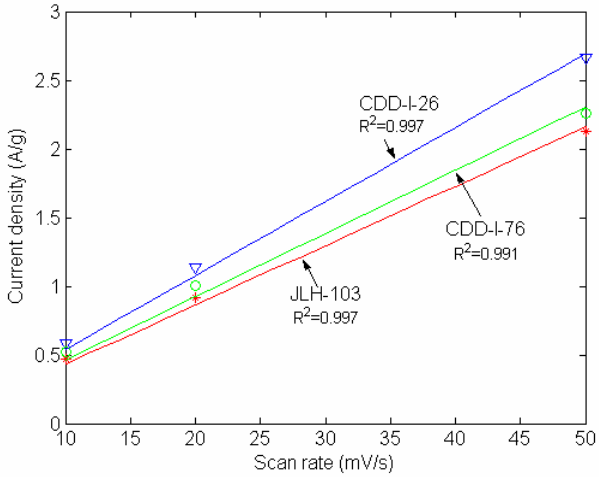

Figure 3.15. Plot of current density as a function of scan rate for functionalized SWNT membranes, which were evaluated in 6 M KOH. R^2 is the correlation coefficient.

The specific capacitance as a function of discharging current density in 6 M KOH aqueous solution is shown in Figure 3.15. The specific capacitance of all functionalized SWNTs monotonically decreases and then tends to level off as the discharging current density increases, just like that of the control bucky paper. It is a general trend due to the entrances of micropores being blocked by larger ions.[20] CDD-I-26 shows higher capacitance values than that of the control bucky paper at the same current density, while JLH-103 exhibits a lower value, which is consistent with the surface area as well as with pore size and pore size distribution. It is very interesting to note that CDD-I-76 shows a higher value at lower discharge current density, but a lower value at higher discharge current as compared to the control bucky paper. Table 3.4 summarizes the porous structural parameters, BET & DFT surface areas, and total pore volume for functionalized SWNTs.

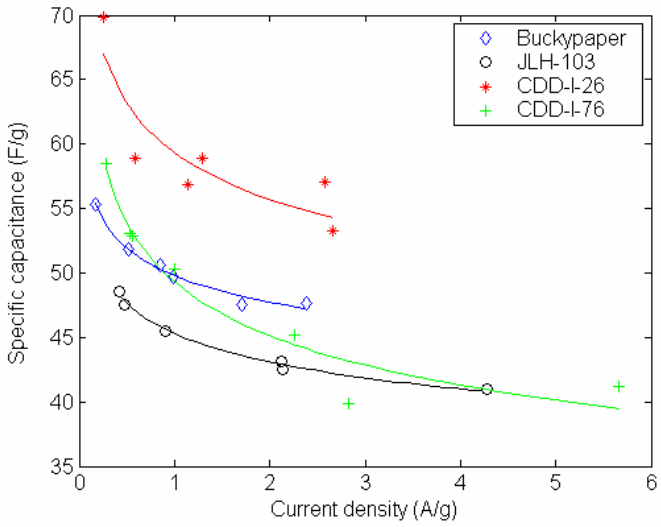

Figure 3.16. Specific capacitance as a function of current density for functionalized SWNT membranes in 6 M KOH.

3.3.8 Capacitance Characterization in Ionic Liquid

The use of ionic liquids, such as 1-butyl-3-methylimidazolium tetrafluoroborate (BMIMBF4), in supercapacitor has been of interest due to their higher operating voltage. The chemical structure of BMIMBF4 is

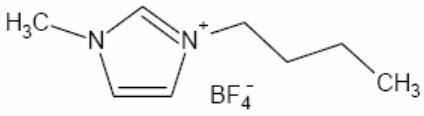

Typical constant current discharging and cyclic voltammograms were shown in Figures 3.16 and 3.17. Linear behavior is observed for bucky paper electrode, while nonlinear behavior for other functionalized SWNT membrane electrodes in ionic liquids. This nonlinear behavior can be caused by pore size distribution and redox reactions. Cyclic voltammetry at scan rates of 10, 20, 50 or 100 mV/s have been used to evaluate these SWNT membrane electrodes in ionic liquids as shown Figure 3.17. Although there is no peak on the curves, the ideal rectangular shape can not be observed. It is similar to the results in the literature.[21] This voltammetric curves change their shapes due to the detrimental of functional groups on the SWNT electrode surface at high voltage window (~3 V) in ionic liquid.[22] The current densities at 0.1 V were plotted as a function of scan rate as shown in Figure 3.18. Linear plots have not been observed, which means that overall redox reactions in these materials are obvious due to the detrimental of functional groups in high voltage environment.

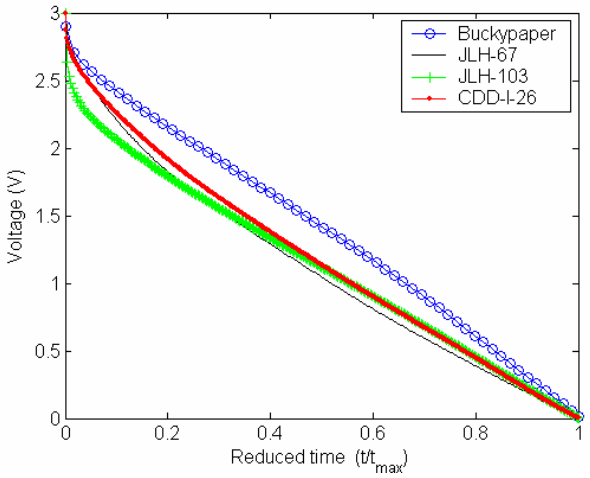

Figure 3.17. Constant current charging/discharging behavior in BMIMBF4 for bucky paper and functionalized SWNTs as a function of reduced time. The current is 1 mA.

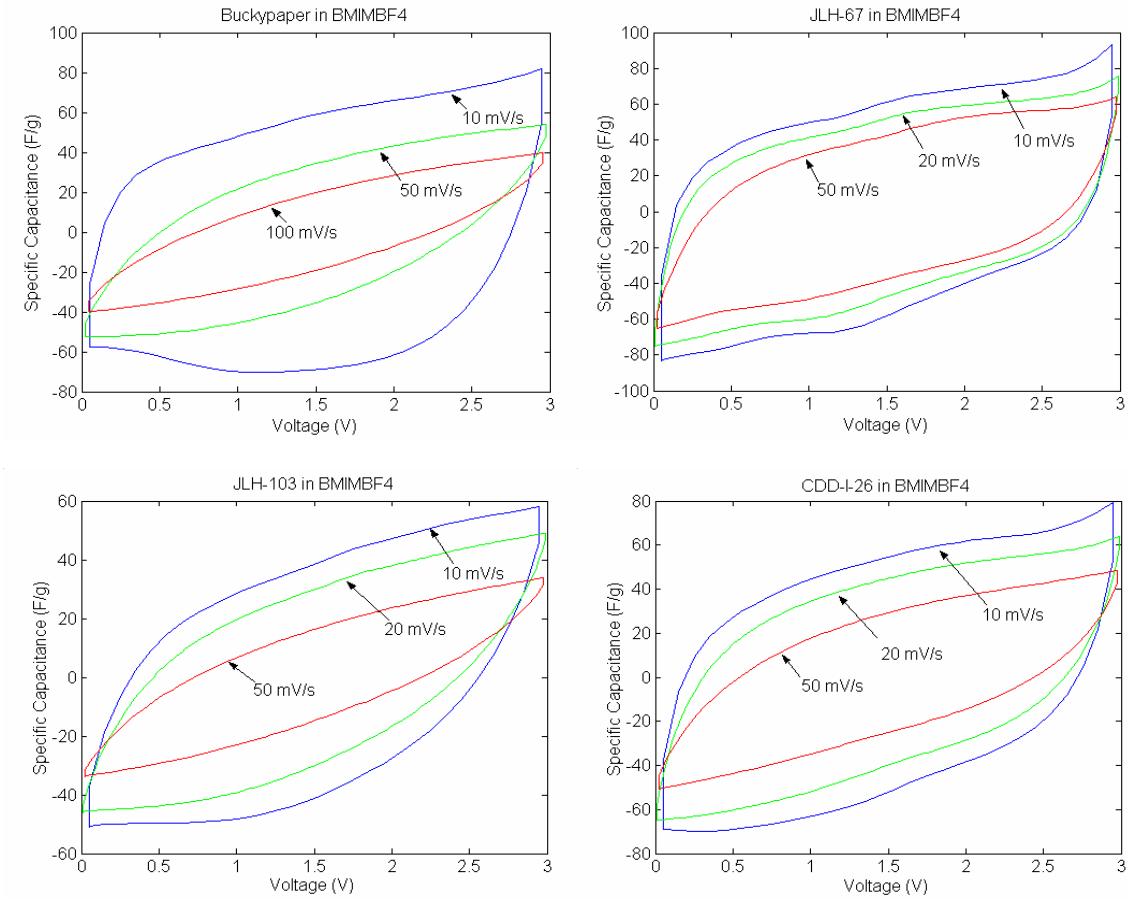

Figure 3.18. Cyclic voltammetry characteristic of supercapacitors based on functionalized SWNT in BMIMBF4 at different scan rates.

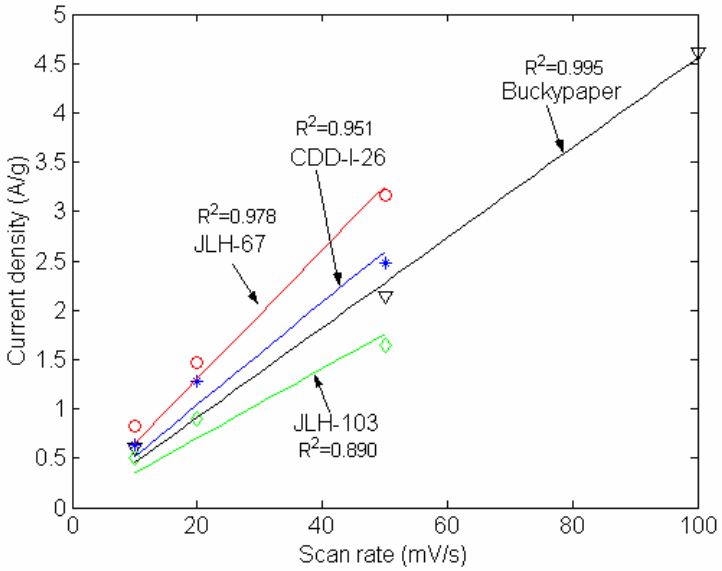

Figure 3.19. Plot of current density as a function of scan rate for functionalized SWNT membranes, which were evaluated at BMIMBF4. R^2 is the correlation coefficient.

The specific capacitance in ionic liquid decreases with increasing current density, but the decreasing rate (slope) of the bucky paper is smaller than that for the functionalized SWNT membranes (Figure 3.19). At high current density, the surface area contribution from micropores may not be accessed by the electrolytes. Only meso and macro pores are useful for capacitance. Meso and macro surface of bucky paper is the highest among these samples, explaining the lowest decreasing rate of the capacitance. Comparing capacitance values in KOH (Figure 3.15) and in ionic liquid (Figure 3.19), one notices that CDD-I-26 shows much higher capacitance values in ionic liquid due to the fact that the chemical affinity of the functional groups on electrodes to the electrolyte is improved. This observation is consistent with the contact angle values in KOH and in BMIMBF4 as shown in Table 3.3. Generally the

capacitance in organic electrolyte is lower than that in aqueous solution.[23]

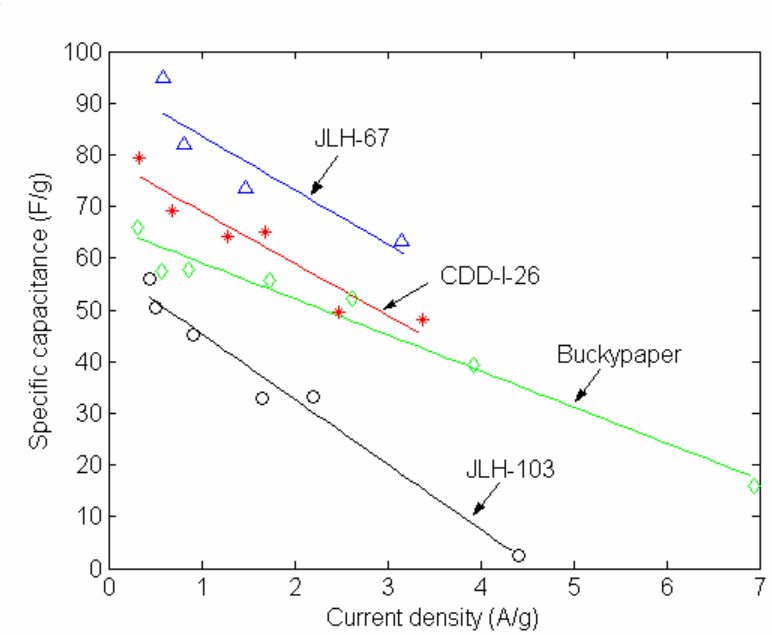

Figure 3.20. Specific capacitance as a function of discharge current density for functionalized SWNT membranes in ionic liquid.

The specific capacitance of functionalized SWNT membranes with different functional groups in 6 M KOH does not show proportionality to their total surface area, and neither to macro surface area as shown in Figure 3.20.

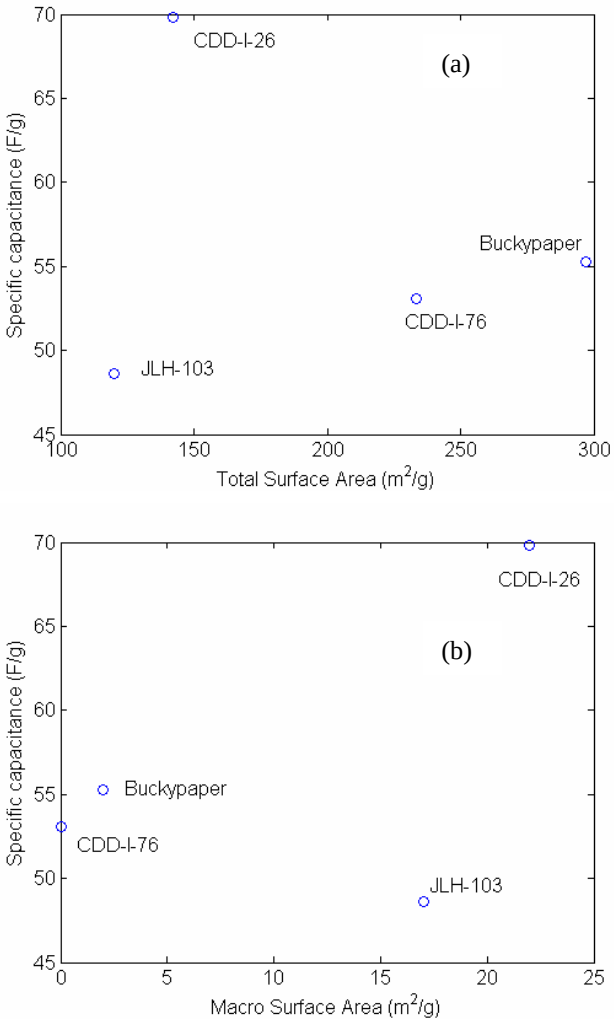

Figure 3.21. (a) Specific capacitance in 6 M KOH vs. total surface area for SWNT bucky paper and functionalized electrodes; (b) Specific capacitance in 6 M KOH vs. macro surface area for SWNT bucky paper and functionalized electrodes.

Figure 3.21 shows the plot of specific capacitance of bucky paper, JLH-67, JLH-103, and CDD-I-26 in BMIMBF4 as a function of their total surface area and macro surface area. However, no proportionality is observed between them. This behavior is in contrast to that of the functionalized SWNT membrane electrodes with same functional groups as discussed earlier in this chapter.

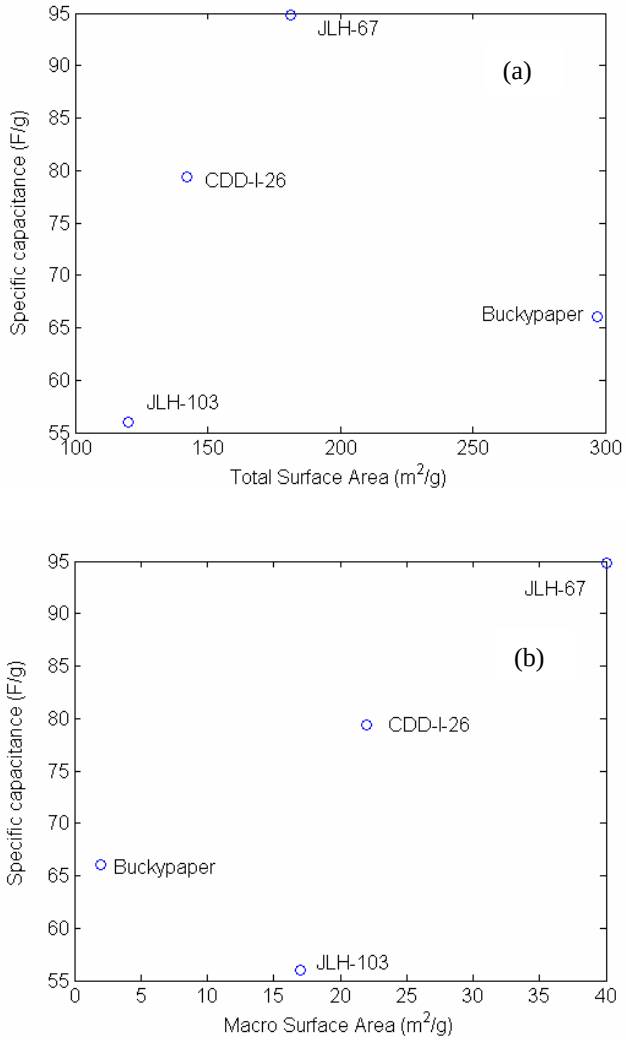

Figure 3.22. (a) Specific capacitance in BMIMBF4 vs. total surface area for SWNT bucky paper and functionalized electrodes; (b) Specific capacitance in BMIMBF4 vs. macro surface area for SWNT bucky paper and functionalized electrodes.

The Ragone plots at a discharging current of 10 mA in ionic liquid is shown in Figure 3.22 for control bucky paper and several functionalized SWNTs (JLH-103, CDD-I-26, and JLH-67). In BMIMBF4, those functionalized samples have power density up to 3 kW/kg, and the control bucky paper has energy density of 17 kJ/kg. The power density of the electrode is limited by its conductivity and capacitance, and

control bucky paper has higher conductivity than functionalized SWNTs because functional groups deteriorate SWNT's conductivity.

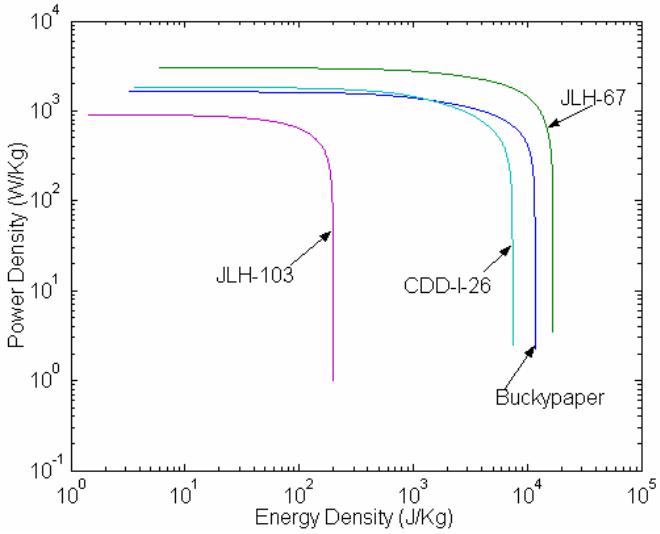

Figure 3.23. Ragone plots for functionalized SWNT electrodes in ionic liquid which are at a discharge current of 10 mA.

3.3.9 X-ray Photoelectron Spectroscopy

The films have been characterized by X-ray diffraction (Appendix B). Microstructures (pore size, pore size distribution) affect the capacitance, and double layer capacity.[24] The surface groups are also very important to the performance of the electrodes.[25] Hence X-ray Photoelectron Spectroscopy (XPS) was used to examine the atomic composition of the electrode surface. It shows that the oxygen content is much increased after functionalization with different chemical compounds as compared to the control bucky paper (Table 3.5). The high capacitance of JLH-67 is at least partially attributed to the high content of the oxygen. The addition of

oxygen is strongly dependent on the functionalization degree. It is not surprising that some samples have high oxygen content.

Table 3.5. Atomic concentration on SWNT and functionalized SWNTs electrode surface obtained from XPS

	C (%)	O (%)	S (%)	Cl (%)	Na (%)
Bucky paper	96.0	4.0			
JLH-67	84.5	12.9		2.6	
JLH-103	87.1	8.9	0.7		3.3
CDD-I-26	87.0	11.6		1.4	
CDD-I-76	89.7	10.3			

3.4 Conclusions

SWNTs were functionalized with different functional groups, such as bis(3,5-di-tert-butylphenyl)5-aminobenzene-1,3-dioate, sodium sulfonate, and arylchloride & 4,4'-methylene-dianiline, arylchloride. The capacitance, power density and energy density were evaluated in 6 M KOH and BMIMBF4 using galvanostatic constant current charge/discharge and cyclic voltammetry. The surface area, pore size, and pore size distribution were determined by N_2 isothermal adsorption and desorption. Correlating the capacitance with surface area, pore size, and pore size distribution, it was found that the macropores make significant contribution to the capacitance performance of some materials. The effect of

functionality on the specific capacitance is also examined. The capacitance of SWNT with arylchloride groups is up to 97 F/g, which is almost 2 times that of the control bucky paper. In BMIMBF4, functionalized SWNT electrodes can have high power density (3 kW/kg) and high energy density (17 kJ/kg). The capacitance value of some samples in ionic liquid is even higher than that in 6 M KOH. This was attributed to the chemical affinity between the electrode surface and the electrolyte.

3.5 References

1 R. H. Baughman, A. A. Zakhidov, W. A. de Heer. *Science* **2002**, *297*, 787.

2 A. Eitan, K. Jiang, R. Andrews, L.S. Schadler. *Chem. Mater.* **2003**, *15*, 3198.

3 J. Zhu, J. D. Kim, H. Q. Peng, J. L. Margrave, V. N. Khabashesku, E. V. Barrera. *Nano Letters* **2003**, *3*, 1107.

4 V. Georgakilas, N. Tagmatarchis, D. Pantarotto, A. Bianco, J.-P. Briand and M. Prato. *Chem. Commun.* **2002**, 3050–3051.

5 M. L. Shofner, V. N. Khabashesku, E. V. Barrera. *Chem. Mater.* **2006,** *18,* 906.

6 J. L. Bahr, J. M. Tour. *Chem. Mater.* **2001**, *13*, 3823.

7 M. J. O'Connell, P. J. Boul, L. M. Ericson, C. B. Huffman, Y. Wang, E. Haroz, C. Kuper, J. M. Tour, K. Ausman, R. E. Smalley. *Chem. Phys. Lett.* **2001**, *342*, 265.

8 J. Liu, A. G. Rinzler, H. Dai, J. H. Hafner, R. K. Bradley, P. J. Boul, A. Lu, T. Iverson, K. Shelimov, C. B. Huffman, F. Rodriguez- Macias, Y.-S. Shon, T. R. Lee, D. T. Colbert, R. E. Smalley. *Science* **1998**, *280*, 1253.

9 J. L. Hudson, M. J. Casavant, J. M. Tour. *J. Am. Chem. Soc.* **2004**, *126*, 11158.

10 C. A. Dyke, M. P. Stewart, J. M. Tour. *J. Am. Chem. Soc.* **2005**,*127*, 4498.

11 K. H. An, W. S. Kim, Y. S. Park, J. M. Moon, D. J. Bae, S. C. Lim, Y. S. Lee, Y. H. Lee. *Advanced Materials* **2001**, *13(7)*, 497.

12 C. Niu, E. K. Sichel, R. Hoch, D. Moy, H. Tennent. *Appl. Phys. Lett.* **1997**, *70(11)*, 1480.

13 C. Zhou, S. Kumar, C. D. Doyle, J. M. Tour. *Chem. Mater.* **2005**, *17*, 1997.

14 E. Frackowiak, K. Jurewicz, S. Delpeux, F. Beguin. *J. Power Sources* **2001**, *97*, 822.

15 Y. H. Hu, E. Ruckenstein. *Ind. Eng. Chem. Res.* **2004**, *43*, 708.

16 H. Hu, B. Zhao, M. E. Itkis, R. C. Haddon. *J. Phys. Chem. B* **2003**, *107*, 13838.

17 B. E. Conway. *Electrochemical Supercapacitors, Scientific Fundamental and Technological Applications*, Plenum Publishers, **1999**.

18 P. A. Webb, C. Orr. Analytical Methods in Fine Particle Technology, Micromeritics Instrument Corp. **1997**.

19 C.-M. Yang, H. Noguchi, K. Murata, M. Yudasaka, A. Hashimoto, S. Iijima, K. Kaneko. *Advanced Materials* **2005**, *17*, 866.

20 C. Kim, J. S. Kim, S. J. Kim, W. J. Lee, and K. S. Yang. *J. Electrochem. Soc.* **2004**, *151(5)*, A769.

21 A. Balducci, U. Bardi, S. Caporali, M. Mastragostino, F. Soavi. *Electrochemistry Communications* **2004**, *6*, 566.

22 A. Lewandowski, M. Galinski. *Journal of Physics and Chemistry of Solids* **2004**, *65*, 281.

23 G. Salitra, A. Soffer, L. Eliad, Y. Cohen, and D. Aurbach. *J. Electrochem. Soc.* **2000**, *147(7)*, 2486.

24 K. Kinoshita. *Carbon Electrochemical and Physicochemical Properties*, John Wiley & Sons, New York, **1988**.

25 X. Chu, K. Kinoshita. *The Electrochemical Society Proceedings* **1995**, *95-29*, 234.

CHAPTER 4

FUNCTIONALIZED SINGLE WALL CARBON NANOTUBES TREATED WITH PYRROLE FOR ELECTROCHEMICAL SUPERCAPACITOR MEMBRANES

4.1 Introduction

The CNT/conducting polymer composites prepared for supercapacitor applications have received much attention.[1,2,3,4,5,6,7,8] It is said that CNTs are electron acceptors, while the conducting polymer serves as a electron donor in the CNT/conducting polymer composites. The CNT matrices can provide a mesoporous scaffold and offer more active sites for faradaic reactions, hence achieving a high charge dynamics during supercapacitor performance.[6] For this class of materials, capacitance values from 80 to 310 F/g have been reported and depend on the conducting polymer, the CNT/conducting polymers fabrication method and the electrolyte.[1-8] In Chapter 3, we found that functionlization can improve the capacitance of CNT. In order to take a full advantage of the high capacitance of functionalized CNTs, in this chapter, methodology for the fabrication of nanoscale-enhanced electrochemical capacitor electrodes that can achieve very high capacitance is described. The electrodes are based on a composite of water-soluble arylsulfonic acid-functionalized SWNTs that had been treated with pyrrole.

4.2 Experimental Section

4.2.1 Functionalized SWNT Membrane Preparation

In a typical SWNT functionalization procedure,[9] 175 mg of p-SWNT (oxidatively purified SWNT) was treated with sulfonilic acid (10.08 g, 0.0582 mole), sodium nitrite (4.02 g, 0.0583 mole) and 2,2'-azobisisobutyronitrile (0.96 g, 0.0058 mole) in 200 mL oleum at 80 °C for 1 h to give a product (after standard workup[9]) in which 1 in 54 carbons of the SWNT were functionalized by an arylsulfonic acid group. The degree of functionalization was determined based on thermogravimetric analysis (TGA). In a typical pyrrole treatment, 28 mg of the functionalized SWNT was mixed in 300 mL deionized water with $Fe(II)Cl_2$ (50 mg, 0.39 mmol) and pyrrole (4.84 g, 72.1 mmole). After mixing overnight on an orbital shaker, the suspension was filtered using a poly(tetrafluoroethylene)(PTFE) filter and the solid was washed with water. Various samples and sample designations are given in Table 4.1 and the general structure of the functionalized SWNT is given in Figure 4.1. Various characterization methods used to investigate these pyrrole treated SWNT membranes are described in Chapter 2.

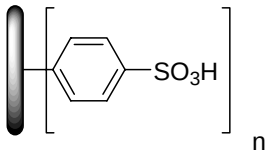

1 - 4

Figure 4.1. The general structure of the arylsulfonic acid functionalized SWNTs in samples **1** to **4.**

Table 4.1. Sample treatments and designations

Sample	Chemical treatment
Bucky paper	untreated HiPco SWNTs
1	p-SWNT* heavily functionalized with arylsulfonic acid moieties (mainly individual tubes) and then treated with pyrrole.
2	Raw SWNT functionalized with arylsulfonic acid moieties and then treated with pyrrole.
3	p-SWNT* functionalized with arylsulfonic acid moieties and then treated with pyrrole; approx. 1 in 33 carbons functionalized by TGA.
4	p-SWNT* functionalized with arylsulfonic acid moieties and then treated with pyrrole; approx. 1 in 54 carbons functionalized by TGA.

*p-SWNT= oxidatively purified material

4.3 Results and Discussion

4.3.1 Morphological Structure

From scanning electron microscopy studies, the diameter of SWNT bundles in the bucky paper was measured to be 48 ± 16 nm, and these bundles appeared to be densely packed and form SWNT rope network (Figure 4.2a). By comparison, SWNT bundle diameters in the pyrrole treated samples were measured to be 46 ± 14 (**1**), 61 ± 18 (**2**), 43 ± 11 (**3**), and 51 ± 13 (**4**) nm. In comparison to bucky paper and pyrrole treated sample **1**, and **2**, the SWNTs in **3** (Figure 4.2d) appear to be shorter and packed more densely. On the surface of these films, there are many pores

among the abundant SWNT or SWNT/pyrrole treated rope networks. The difference in packing was apparently caused by the degree of arylsulfonic acid functionalization. Based on the TGA study, we conclude that 1 out of every 54 carbons were functionalized in **4**, while 1 out of every 33 carbons were functionalized in **3**.

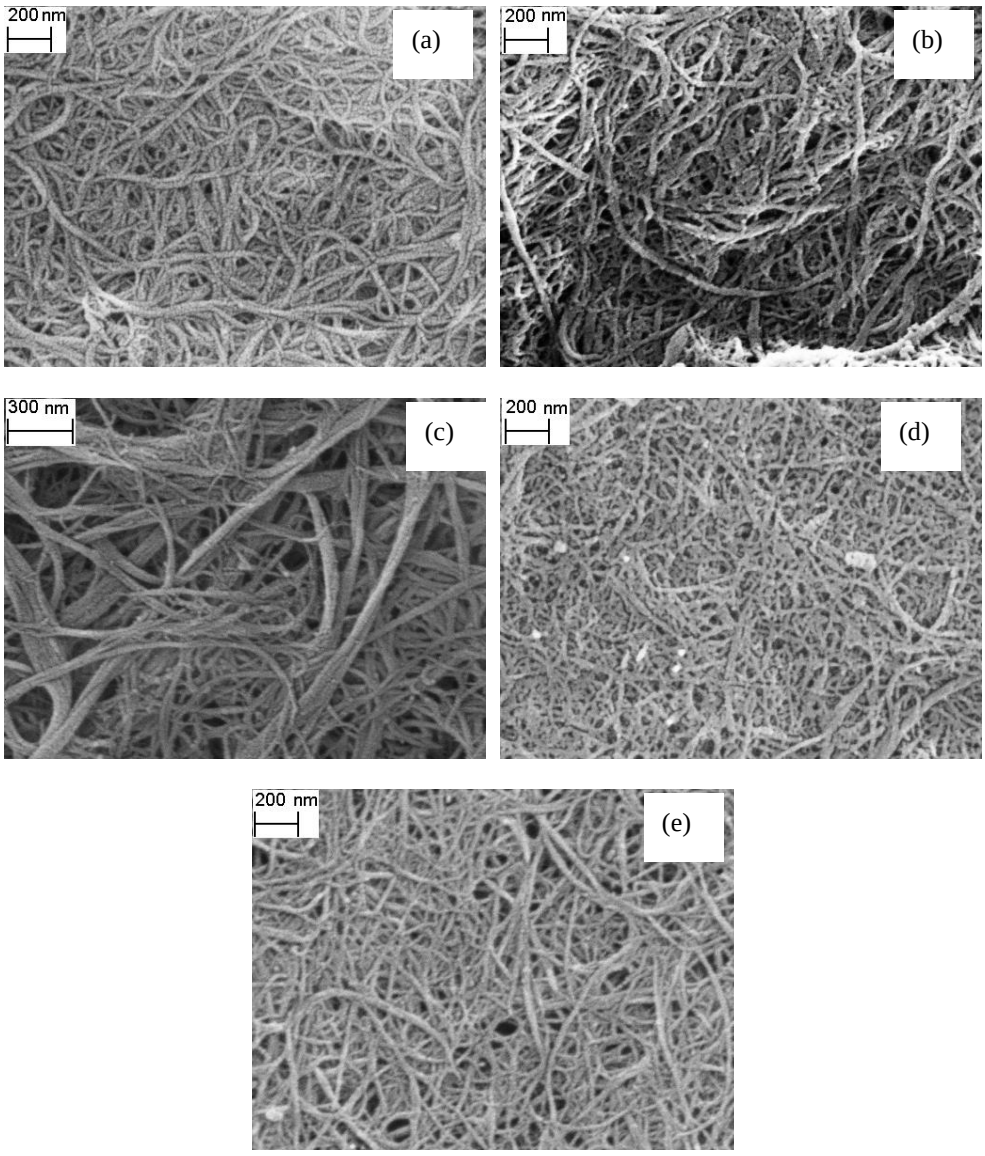

Figure 4.2. SEM images of SWNT and pyrrole treated functionalized SWNTs electrodes surface. (a) Bucky paper; (b) **1**; (c) **2**; (d) **3**;(e) **4**.

4.3.2 Characterization of Porous Structure

Bucky paper as well as SWNT/pyrrole treated electrodes exhibit type IV nitrogen adsorption isotherm (Figure 4.3), which is indicative of samples having relatively large pores. Data in Table 4.2 shows that the pyrrole treated samples have a lower surface area than the bucky paper. The ideal specific surface area can be as high as 1315 m^2/g for individual SWNT with 1 nm diameter and about 500 m^2/g for bundles.[10] KOH chemical activation can increase the surface area of CNTs,[11,12] while functionalization can diminish the surface area by destroying small-diameter CNTs.[13,14]

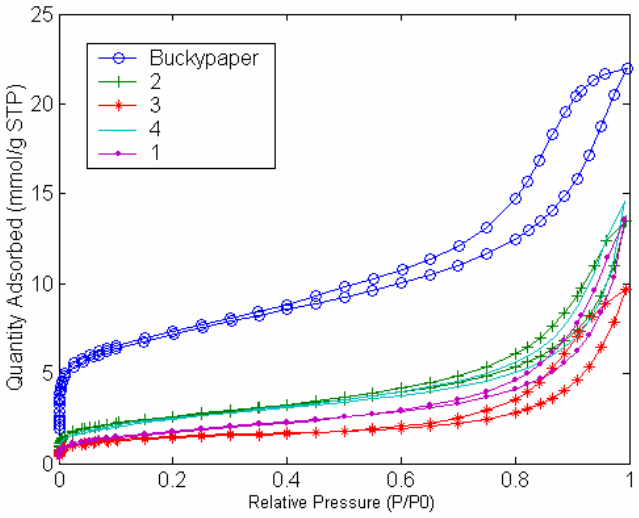

Figure 4.3. Adsorbed N_2 quantity vs. relative pressure of isothermal N_2 adsorption (77 K) of SWNT and pyrrole treated functionalized SWNTs films.

Table 4.2 Capacitance, surface area and pore volume of bucky paper and pyrrole treated SWNTs electrodes. Sample designations are shown in Table 4.1.

		Bucky paper	**1**	**2**	**3**	**4**
Capacitance (F/g) *	0.1 V	**55**	**176**	**151**	**114**	**305**
	0.7 V	41	28	41	36	45
	Mean value	49	102	93	80	183
BET surface area (m^2/g)		546	148	205	113	198
Total Pore Volume (cm^3/g)		0.76	0.47	0.47	0.34	0.51
DFT surface area (m^2/g)	Total	297	95	122	66	125
	Micro**	167	12	40	32	24
	Meso	128	27	46	27	25
	Macro	**2**	**56**	**36**	**7**	**76**
DFT Pore Volume (cm^3/g)	Total	0.69	0.28	0.32	0.30	0.25
	Micro	0.11	0.01	0.03	0.02	0.02
	Meso	0.52	0.21	0.25	0.22	0.18
	Macro	0.06	0.06	0.05	0.06	0.05
C_{dl} ($\mu F/cm^2$) (0.1 V Capacitance)	BET	**10**	**119**	**74**	**101**	**154**
	DFT-Total	19	186	124	173	243
	DFT-meso&macro	43	214	183	330	302

* 1 mA discharge current

** Micro, meso and macro pore refers the pore size of < 2 nm, 2 nm – 50 nm, and > 50 nm, respectively.

Based on IUPAC classification, the pore size is divided into three groups: micropores (pore width < 2 nm), mesopores (between 2 and 50 nm) and macropores (> 50 nm). As compared to micropores, macropores have negligible contribution to the total surface area.[15,16] Based on the DFT model, it is shown that bucky paper is predominantly composed of micropores, while pyrrole treated samples are mainly composed of meso and macropores (Figure 4.4). The surface area contribution for the pyrrole treated samples from macropores is as high as 61% of total DFT surface area (Table 4.2). Atomic concentration of the bucky paper and pyrrole treated SWNTs electrode surfaces determined from XPS are given in Table 4.3, which shows that **4** contains more pyrrole than **3**.

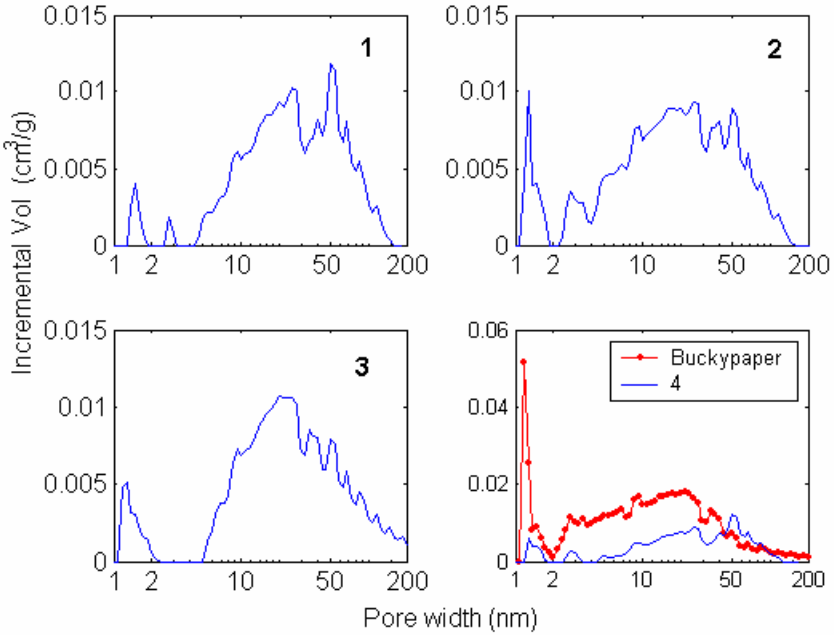

Figure 4.4. Pore size distribution determined by DFT model for SWNT and pyrrole treated functionalized SWNTs electrodes.

Table 4.3. Atomic concentration on SWNT and pyrrole treated SWNTs electrode surface obtained from XPS

	C (%)	**O (%)**	**N (%)**	**S (%)**	**Cl (%)**
Bucky paper	96	4			
3	70.9	18.9	8.1	1.8	0.3
4	74.5	12.3	10.3	2.4	0.5

4.3.3 Capacitance Evaluation

Typical constant current charging/discharging curves for pyrrole treated SWNT are shown in Figure 4.5. Constant current discharge behavior of bucky paper is almost linear with time, while for the pyrrole treated functionalized SWNTs electrodes the discharge behavior is non-linear (Figure 4.6). Figure 4.7 compares a typical cyclic voltammogram for bucky paper and SWNT/pyrrole film electrodes. The bucky paper voltammetric curve is closer to an ideal parallelogram shape, exhibiting no pseudocapacitance or very little contribution from redox reaction. However, in the case of pyrrole treated functionalized SWNTs film electrodes, a peak at 0.1 ~ 0.2 V was observed which may correspond to the oxidation and reduction of polypyrrole that might have been formed during the pyrrole treatment. The CV peak current of pyrrole treated films was double (**1**, **2** and **3**) and four times (**4**) the value obtained for the bucky paper. The capacitance of the bucky paper was about 55 F/g, which was comparable to the value reported in the literature.[17] The specific capacitance of polypyrrole is reported to be about 160 F/g.[18] In this study, pyrrole

treated sample **4** exhibited a specific capacitance of 350 F/g which is 7 times the value obtained for the bucky paper. Current density data obtained at different scan rates at 0.1 V for pyrrole treated SWNT membrane electrodes are plotted in Figure 4.8. The nonlinear behavior of these membranes as can be judged by relatively low correlation coefficient further confirms the redox reaction in the pyrrole treated samples. The specific capacitance of all these samples is voltage and current dependent as shown in Figure 4.9.

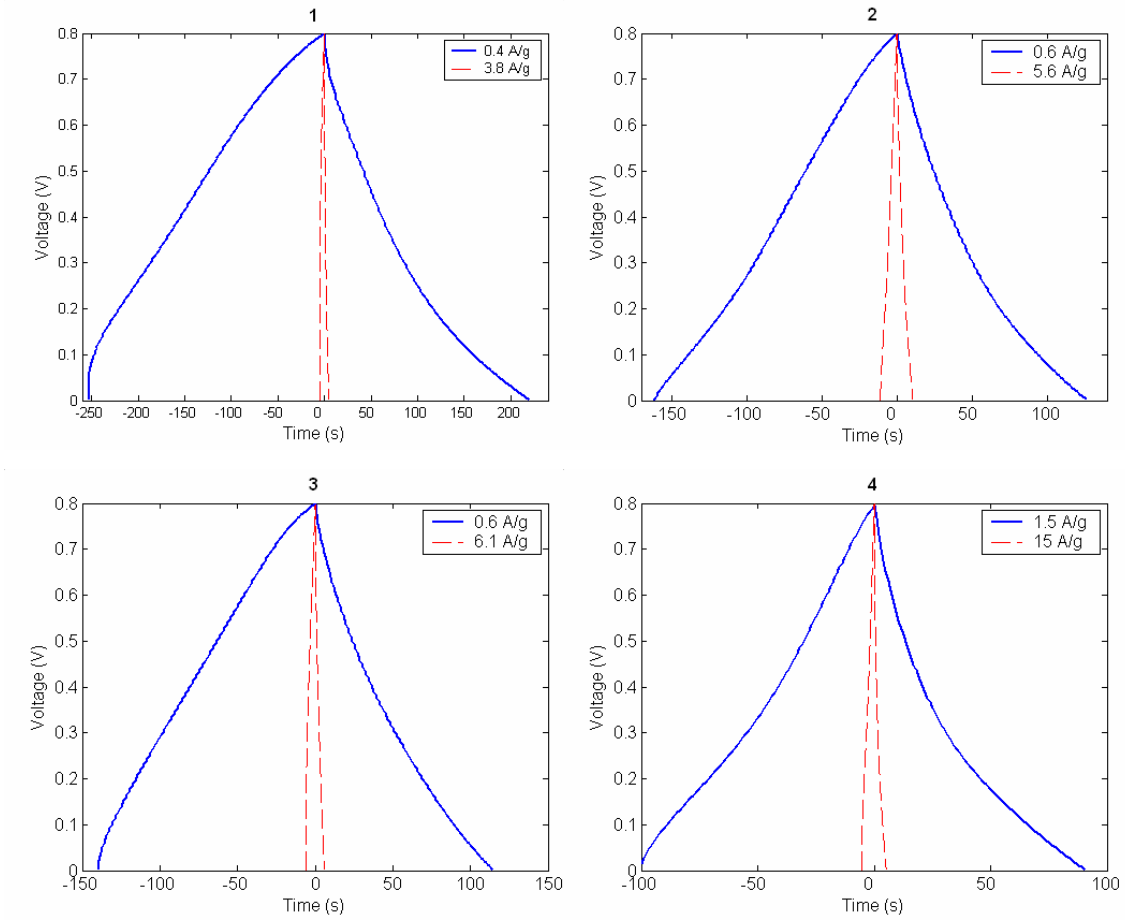

Figure 4.5. Constant current discharge behavior of pyrrole treated arylsulfonic acid functionalized SWNTs.

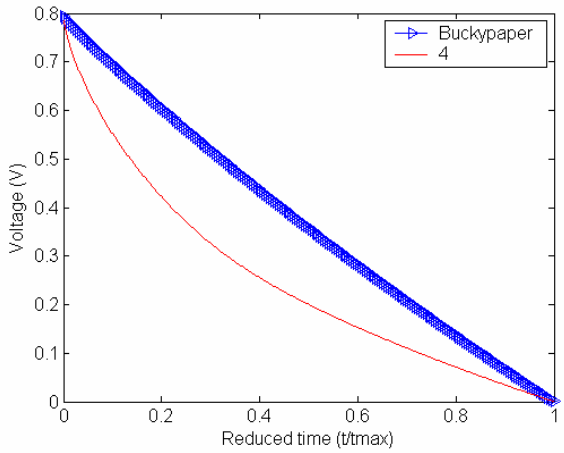

Figure 4.6. Constant current charging/discharging behavior for bucky paper and pyrrole treated arylsulfonic acid functionalized SWNTs as a function of reduced time. The current is 1 mA.

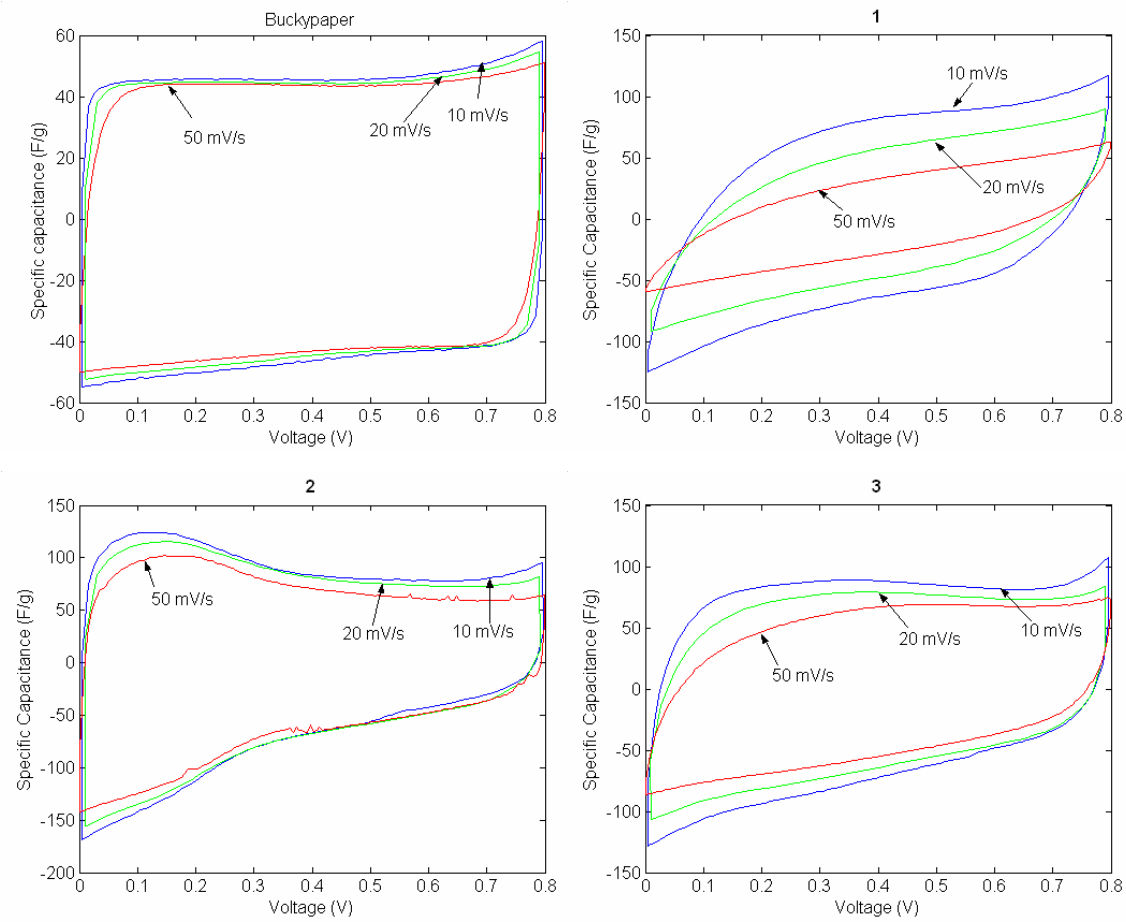

Figure 4.7. Cyclic voltammetry plots of SWNT and pyrrole treated arylsulfonic acid functionalized SWNTs. The scan rates are 10, 20, and 50 mV/s.

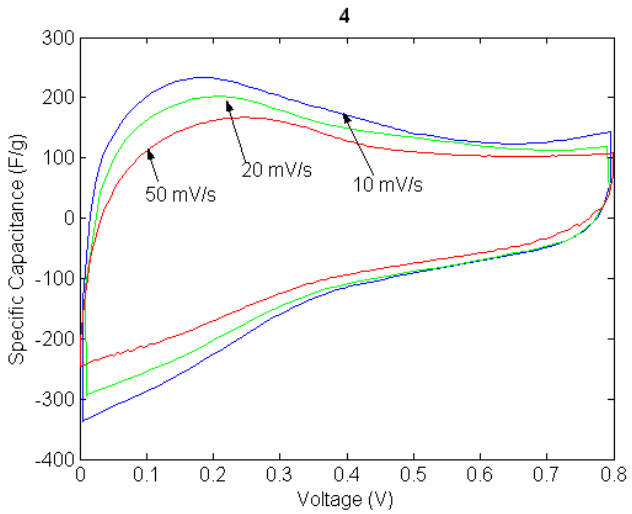

Figure 4.7. continued

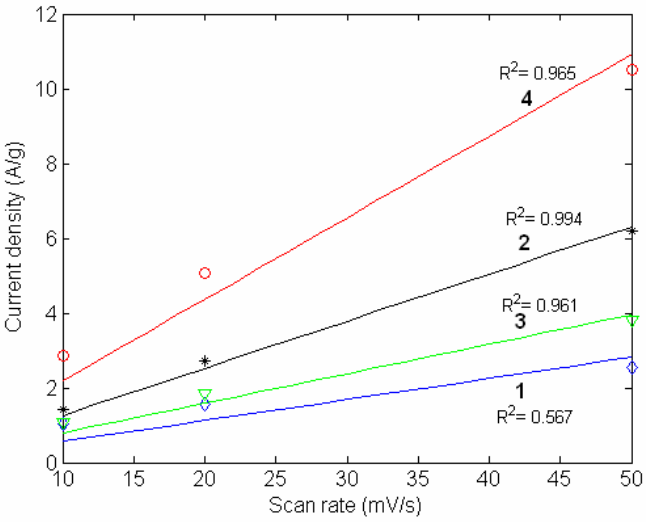

Figure 4.8. Plot of current density as a function of scan rate for pyrrole treated SWNT membranes. R^2 is the correlation coefficient.

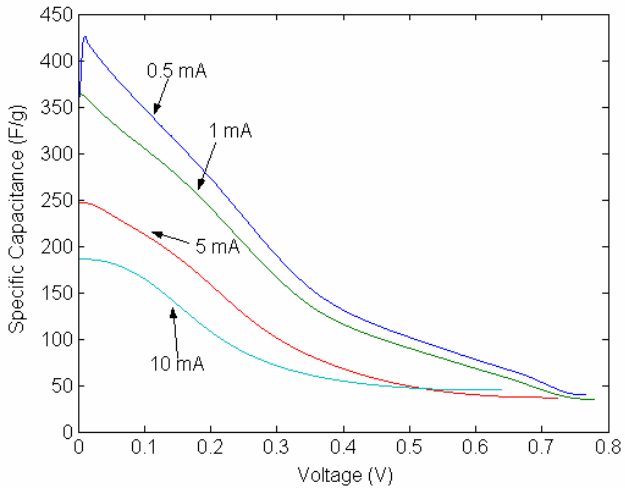

Figure 4.9. The specific capacitance as a function of voltage for sample **4** evaluated at different current.

4.3.4 Correlation of Capacitance with Surface Area and Electrolyte

Figure 4.10 shows the specific capacitance of bucky paper and pyrrole treated functionalized SWNTs as a function of discharge current density. As compared to the bucky paper, all pyrrole treated SWNTs membrane show much improved affinity to the electrolyte because they exhibit lower contact angle than bucky paper (Table 4.4). For sample **1**, it is even completely wetting. This observation can explain why pyrrole treated SWNT membrane electrodes have higher capacitance, although bucky paper shows higher pore volume (0.76 cm^3/g) and surface area (546 m^2/g) than pyrrole treated counterparts. Except for bucky paper, the specific capacitances of the samples decreased rapidly at the relatively low discharge current density, and then tended to level off at higher current density. Sample **1** dropped faster than others from 205 F/g at 0.4 A/g to 50 F/g at 2.5 A/g. The decrease in specific capacitance of pyrrole treated functionalized SWNT samples may be caused by some pores not being

accessible efficiently at higher current density, and perhaps larger internal resistance of the pyrrole moieties in comparison to SWNT.

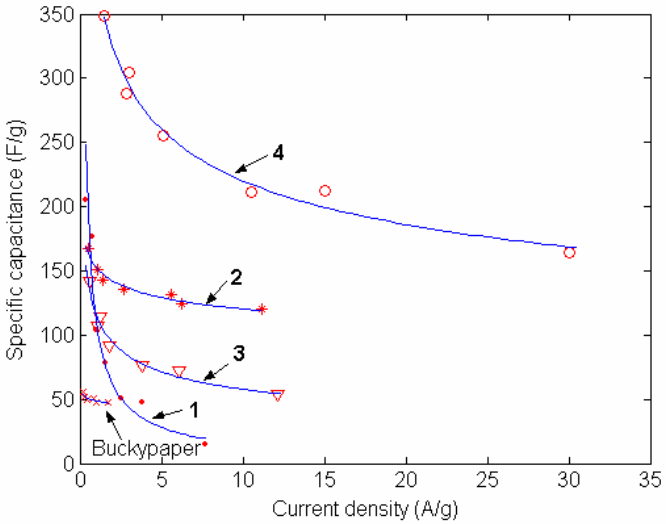

Figure 4.10. Specific capacitance of bucky paper and pyrrole treated SWNT electrodes as a function of discharge current density.

Table 4.4. Contact angles of 6 M KOH on bucky paper and pyrrole treated SWNT electrodes

Bucky paper	**1**	**2**	**3**	**4**
101 ± 3	< 10	22 ± 2	19 ± 2	19 ± 1

Contact angle < 10: completely wetting

Frackowiak et al.[11] reported that micro pores make the main contribution to the specific capacitance because micropores wetted by the electrolyte solution contribute extensively to the adsoption of ions on the electrochemically active surface of the electrodes. Micropores result in high surface area. However, higher surface

area does not always result in higher specific capacitance (Figure 4.11a), as the specific capacitance depends on the pore size and pore size distribution. The capacitance did show proportionality to the macropore surface area contribution to the total surface (Figure 4.11b). All pyrrole treated samples show significant macropore surface area, while macropore surface area in the bucky paper is negligible. It is exciting to note that at 0.1 volt, the capacitances increased from 114 to 305 F/g with the macro surface area increasing from 7 to 76 m^2/g for the pyrrole treated samples. Extrapolation of Figure 4.11b suggests that much higher capacitance value, above 800 F/g, can be expected if the macro surface area can be doubled to about 150 m^2/g.

The double layer storage capacities of the SWNT and pyrrole treated SWNTs electrodes were calculated and are listed in Table 4.2. The double layer capacity of the bucky paper is 10 $\mu F/cm^2$, which is comparable to the value reported for activated carbon materials.[19] The double layer capacity of the pyrrole treated samples is up to 154 $\mu F/cm^2$ based on the BET model, while higher values were obtained based on the DFT model.

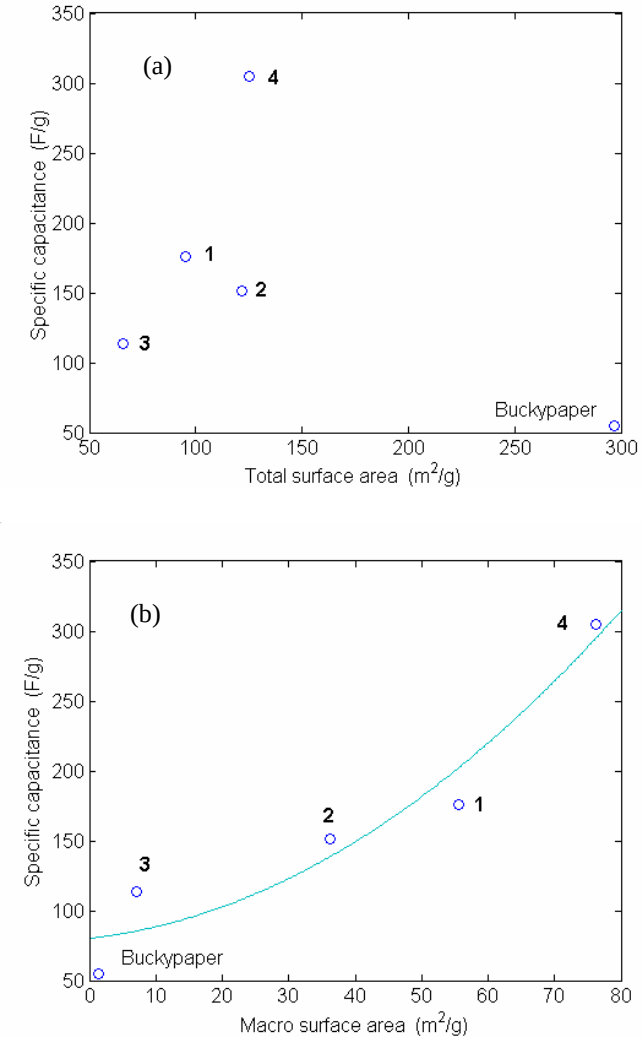

Figure 4.11. Specific capacitance vs. total surface area (a) and macro surface area (b) for SWNT bucky paper and pyrrole treated SWNTs electrodes.

4.3.5 Power Density and Energy Density

The Ragone plot (Figure 4.12) shows that the pyrrole treated samples have higher power (up to 4.8 kW/kg), and energy (3.3 kJ/kg) densities than the bucky paper. At 10 mA discharging current, the power density of **4** is almost 25 times that of the control bucky paper electrode.

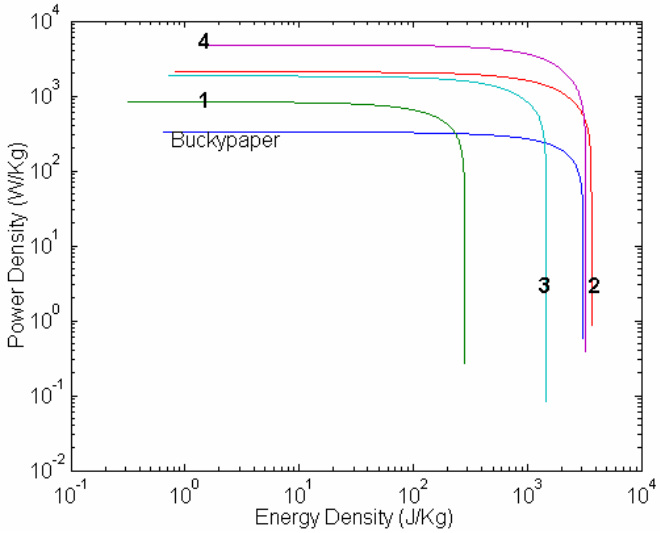

Figure 4.12. Ragone plots for pyrrole treated SWNT electrodes in 6 M KOH which are at a discharge current of 10 mA.

4.4 Conclusions

The SWNTs were functionalized with arylsulfonic acid and treated with pyrrole. The capacitance, power density and energy density were evaluated using galvanostatic constant current charge/discharge and cyclic voltammetry. The capacitance is up to 350 F/g, which is almost seven times that of the untreated bucky paper. The surface area, pore size, and pore size distribution were determined by N_2 isothermal adsorption and desorption. Correlating the capacitance with surface area, pore size, and pore size distribution, it was observed that the macropores make a significant contribution to the capacitance performance of these materials. The double layer storage capacity can be as high as 154 $\mu F/cm^2$ based on the BET model, and even higher based on the DFT model.

4.5 References

1 K. Jurewicz, S. Delpeux, V. Bertagna, F. Beguin, E. Frackowiak. *Chem. Phys. Lett.* **2001**, *347*, 36.

2 K. H. An, K. K. Jeon, J. K. Heo, S. C. Lim, D. J. Bae, Lee, Y. H. *J. Electrochem. Soc.* **2002**, *149 (8)*, A1058.

3 M. Hughes, G. Z. Chen, M. S. P. Shaffer, D. J. Fray, A. H. Windle. *Chem. Mater.* **2002**, *14*, 1610.

4 C. Downs, J. Nugent, P. M. Ajayan, D. J. Duquette, S. V. Santhanam. *Advanced Materials* **1999**, *11(12)*, 1028.

5 G. A. Snook, G. Z. Chen, D. J. Fray, M. Hughes, M. Shaffer, *Journal of Electroanalytical Chemistry*, **2004**, *568*, 135.

6 E. Frackowiak, K. Jurewicz, K. Szostak, S. Delpeux, F. Beguin. *Fuel Processing Technology* **2002**, *77–78*, 213.

7 Q. Xiao, X. Zhou. *Electrochimica Acta* **2003**, *48*, 575.

8 Y. Zhou, B. He, W. Zhou, H. Li. *J. Electrochem. Soc.* **2004**, *151(7)*, A1052.

9 J. L. Hudson, M. J. Casavant, J. M. Tour. *J. Am. Chem. Soc.* **2004**, *126*, 11158.

10 A. Peigney, Ch. Laurent, E. Flahaut, R. R. Bacsa, A. Rousset. *Carbon* **2001**, *39*, 507.

11 E. Frackowiak, S. Delpeux, K. Jurewicz, K. Szostak, D. Cazorla-Amoros, F. Beguin. *Chem. Phys. Lett.* **2002**, *361*, 35.

12 E. Raymundo-Pinero, D. Cazorla-Amoros, A. Linares-Solano, S. Delpeux, E. Frackowiak, K. Szostak, F. Beguin. *Carbon* **2002**, *40*, 1597.

13 X. Zhang, T. V. Sreekumar, T. Liu, S. Kumar. *J. Phys. Chem. B* **2004,** *108(42)*, 16435.

14 M. Zhang, M. Yudasaka, S. Iijima. *J. Phys. Chem. B* **2004**, *108*, 149.

15 K. H. An, W. S. Kim, Y. S. Park, Y. C. Choi, S. M. Lee, D. C. Chung, D. J. Bae, S. C. Lim, Y. H. Lee. *Adv. Mater.* **2001**, *13(7)*, 497.

16 H. Shi. *Electrochimica Acta* **1996**, *41(10)*, 1633.

17 T. Liu, T. V. Sreekumar, S. Kumar, R. H. Hauge, R. E. Smalley. *Carbon* **2003**, *41*, 2427.

18 M. D. Ingram, H. Staesche, K. S. Ryder. *J. Power Sources* **2004**, *129*, 107.

19 B. E. Conway. *Electrochemical Supercapacitors, Scientific Fundamental and Technological Applications*, Plenum Publishers, **1999**.

CHAPTER 5

COMPARISON OF CARBON NANOTUBE BASED ELECTROCHEMICAL SUPERCAPACITOR ELECTRODES USING DIFFERENT ELECTROLYTES

5.1 Introduction

Room temperature ionic liquids, also called molten salts, are compounds that consist solely of ions.[1] They are non-volatile, non-flammable liquids, even up to temperatures as high as 300 ^{o}C.[2] Hence ionic liquids have been widely utilized as clean solvents and catalysts for green chemistry and as electrolytes for batteries,[3,4] supercapacitor, [5,6] photochemistry[7,8] and electrosynthesis.[9,10] Ionic liquids may be used as solvents for special reactions, such as synthesis of n-doped poly(3,4-ethylenedioxythiophene),[11] and functionalization of SWNT in large quantities.[12] It is also reported that electrochemical doping with ionic liquid causes reversible bleaching of the transitions between van hove singularities of carbon nanotubes.[13]

Ionic liquids as electrolyte offer a greater electrochemical stability window, high conductivity and high energy density as compared to aqueous electrolytes. Gale and Osteryoung[14] first investigated a room temperature ionic liquid. The capacitance value of dropping mercury electrodes (DME) at several ionic liquids is in the range of 10.6 to 12.5 μF/cm^2, which is lower than that in H_2SO_4 or KCl aqueous solution (about 14.6 - 15.1 μF/cm^2).[15] A series of ionic liquids, which consist of 1-ethyl-3-methyl imidazolium, 1-butyl-3-methyl imidazolium and 1-methyl-1-propyl

pyrrolidinium cations, as well as of tetrafluoroborate, hexafluorophosphate and bis((trifluoromethyl)- sulfonyl)imide anions, have been prepared for activated carbon based supercapacitors. [16] It is reported that the specific capacitance in 1-ethyl-3-methylimidazolium bis((trifluoromethyl)sulfonyl)imide can be up to 180 F/g for activated carbon with a surface area of about 2600 m^2/g, and high energy density is obtained.[16] Cycling stability of a hybrid activated carbon/poly(3-methylthiophene) supercapacitor with N-butyl-N-methylpyrrolidinium bis(trifluoromethanesulfonyl)imide as electrolyte has been investigated at 60 ^oC. The supercapacitor shows good performance as its power and energy densities can be 40 to 50% of the initial values even after 16000 cycles.[17]

Recently two phosphonium salts, trihexylstetradecyldphosphonium bisstri-fluoromethylsulfonyldimide and trihexylstetradecyld phosphonium dicyanamide were used for activated carbon based supercapacitors. Capacitance of 100 F/g was achieved in the mixture of ionic liquid containing 25 wt% acetonitrile, up to an operating voltage of 3.4 V. Energy density of ~ 40 Wh/kg and good cyclability were reported. [18] A comparative study on the ionic liquid's mixing effect by polypropylene carbonate was also reported.[19] Low-decomposition–voltage (~ 2V) ionic liquid, such as 1-ethyl-3-methylimidazolium fluoride, was also reported recently.[20] Carbon nanotube bucky paper electrodes were investigated in several ionic liquid electrolytes, and lower capacitance was found as compared to the conventional aqueous electrolytes.[21] Similar results have been obtained for other carbon material electrodes and DME in ionic liquid electrolytes.[15,20]

The purpose of this chapter is to compare the performance of control bucky paper, arylsulfonic acid-functionalized SWNTs and PAN/SWNT/SAN(63/7/30) in 6 M KOH and in ionic liquid. These samples represent 3 different types of carbon nanotube based materials, which are prepared by different methods and have different pore structure and surface area. Special affinity between CNT and ionic liquid has been observed.[22,23]

5.2 Materials and Experiment

5.2.1 Materials Preparation

Bucky paper made from HiPCO SWNT was supplied by Carbon Nanotechnologies, Inc. (CNI), with an in-plane electrical conductivity of ~ 2.3×10^4 (S/m). An arylsulfonic acid-functionalized SWNTs (JLH-72) membrane was prepared by Dr James M. Tour's group at Rice University, which was approximately 1 in 58 carbons functionalized as estimated by TGA.[24] Carbonized PAN/SWNT/SAN (63/7/30) films were same as described in Chapter 2.

5.2.2 Characterization Techniques

For capacitance evaluation, 1-butyl-3-methylimidazolium tetrafluoroborate (BMIMBF4) (Merck KGaA, Germany), 1-butyl-3-methylimidazolium hexafluoro-phosphate(BMIMPF6), 1-butyl-3-methylimidazolium chloride(BMIMCl) (BMIMPF6 and BMIMCl were from Professor Lawrence Bottomley, Georgia Tech), a mixture of ionic liquid/acetonitrile (AN), and 6 M KOH were used as the electrolyte. The

conductivity of 6 M KOH and BMIMBF4 were characterized and are reported in Appendix C. All agents were used as received except that BMIMPF6 and BMIMCl were degassed for 48 hours at room temperature. The chemical structure of the ionic liquids (see below) is 1-butyl-3-methylimidazolium X (BMIMX), where X is BF_4^-, PF_6^-, and Cl^-. Other experimental procedures are described in Chapter 2.

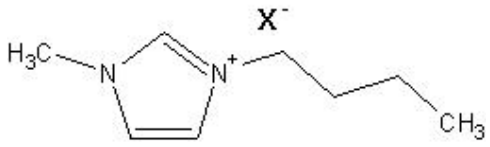

5.3 Results and Discussion

5.3.1 Morphological Structure

The morphological structures of bucky paper and PAN/SWNT/SAN(63/7/30) were discussed in Chapter 2. Arylsulfonic acid functionalized SWNT (JLH-72) membrane appears to be compactly packed and the bundle diameters of greater than 100 nm are frequently observed (Figure 5.1).

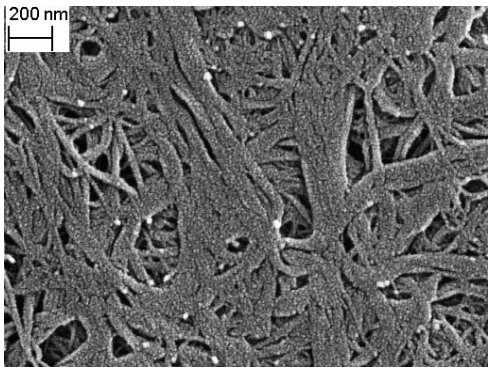

Figure 5.1. Scanning electron micrographs of arylsulfonic acid functionalized SWNT (JLH-72).

5.3.2 Characterization of Porous Structure

Results of nitrogen adsorption and desorption study are given in Figure 5.2. As one can see, bucky paper, PAN/SWNT/SAN(63/7/30), and arylsulfonic acid functionalized SWNT (JLH-72) electrodes exhibited type IV nitrogen adsorption isotherms (Figure 5.2a). All the specimens show broad pore size distribution ranging from 1 to 200 nm (Figure 5.2b). The average pore size in the SWNT bucky paper was 5.6 nm with a pore volume of 0.76 cm^3/g. The average pore size in the PAN/SWNT/SAN was 14.6 nm with a pore volume of 0.12 cm^3/g. The average pore size of arylsulfonic acid functionalized SWNT was about 7.5 nm with the total pore volume of 0.42 cm^3/g. The total surface area of the bucky paper is the highest among the three samples, which at least in part is attributed to the large contribution from micropores.

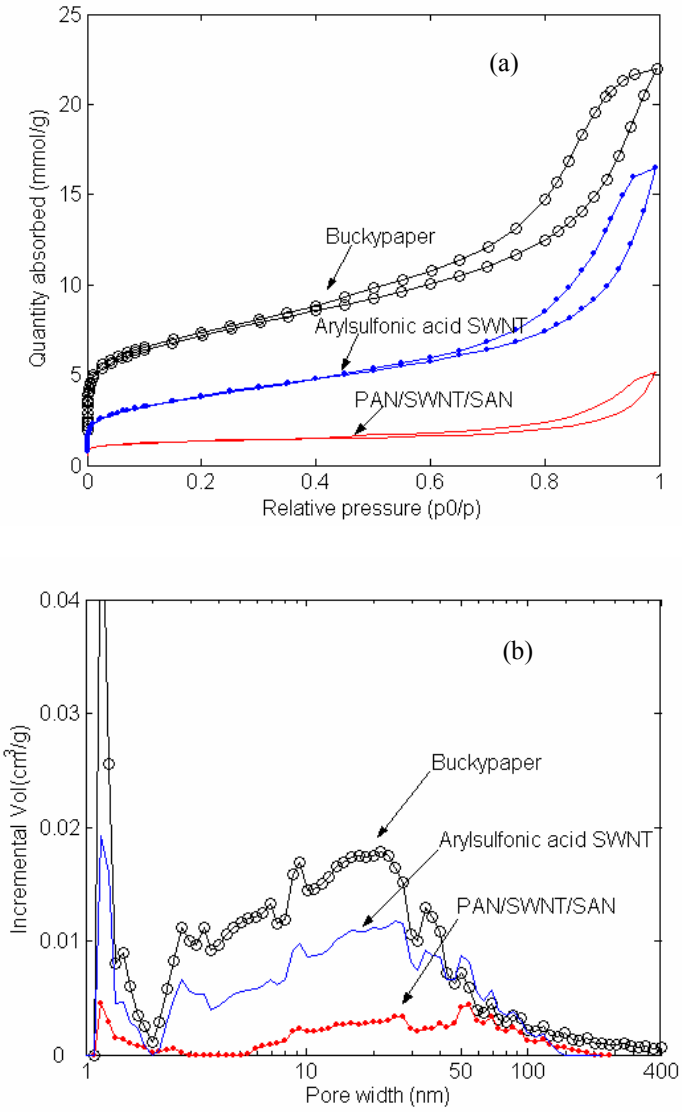

Figure 5.2. Results of isothermal N_2 adsorption (77 K) of various film. a) Adsorbed N_2 quantity vs. relative pressure, b) Pore size distribution determined by the DFT model.

The surface area and pore volume contribution from different pore widths were listed in Table 5.1. Generally speaking, meso or macro pores are preferred, depending on the electrode and the electrolyte used in the electrical double layer capacitors.[24]

Table 5.1. Surface area and pore volume distribution of bucky paper, PAN/SWNT/SAN, and arylsulfonic acid functionalized SWNT (JLH-72)

		Bucky paper	PAN/SWNT/SAN (63/7/30)	arylsulfonic acid SWNT
BET Surface area (m^2/g)		546	97	303
Pore volume (cm^3/g)		0.76	0.18	0.57
DFT Surface area (m^2/g)	total	296	42	186
	micro	167	19	78
	meso	128	9	69
	macro	1	14	39
DFT Pore volume (cm^3/g)	total	0.72	0.12	0.42
	micro	0.11	0.01	0.05
	meso	0.52	0.07	0.32
	macro	0.09	0.04	0.05
Average pore size (nm)		5.6	14.6	7.5

5.3.3 Constant Current Charging/Discharging

The constant current charging/discharging behavior for these electrodes in 6 M KOH and ionic liquids is evaluated at different current densities as shown in Figure 5.3. Comparing these curves in Figure 5.3, a voltage jump is observed for these samples evaluated in ionic liquid, which is due to high resistance of the ionic liquid. The measured constant current discharging curves as a function of reduced time which is the ratio of the actual discharging time, *t*, to the total time of the discharging

process, t_{max}, are shown in Figure 5.4. In 6 M KOH, constant current discharging behaviors of bucky paper and arylsulfonic acid functionalized SWNT are almost linear with time, while for the PAN/SWNT/SAN electrodes the discharging behavior is nonlinear (Figure 5.4a). However, in ionic liquid/acetonitrile or pure ionic liquid electrolyte, all the samples showed nonlinear discharging behavior (Figure 5.4a). The nonlinear behavior may result from the broad pore size distribution of the electrodes or pseudocapacitance induced by the functional groups on the surface of the electrodes.[25]

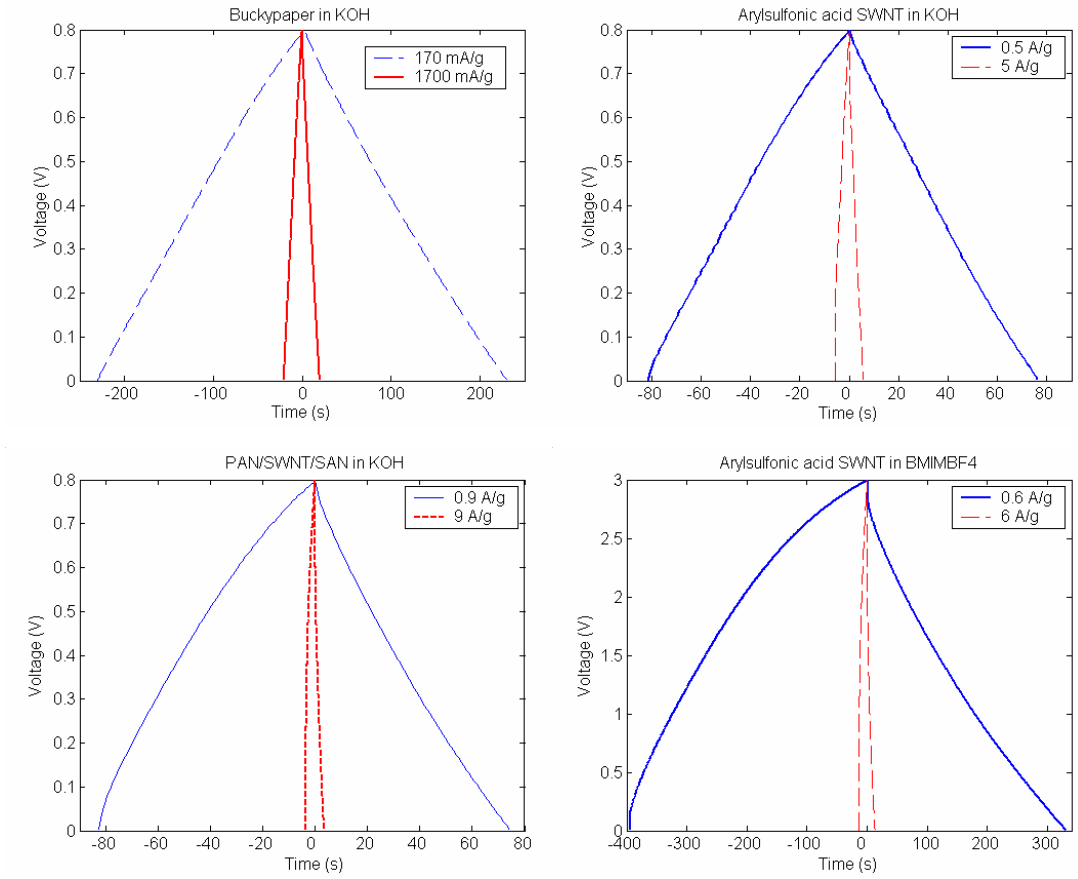

Figure 5.3. Constant current charging/discharging behavior of bucky paper, arylsulfonic acid SWNT membrane (JLH-72), and PAN/SWNT/SAN(63/7/30) ternary composite electrodes at two current densities.

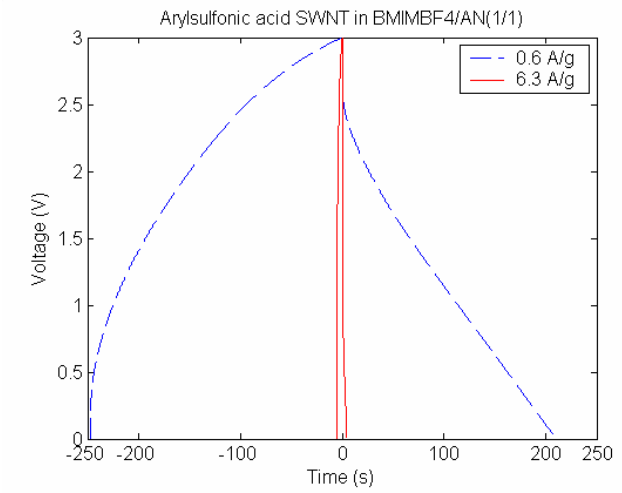

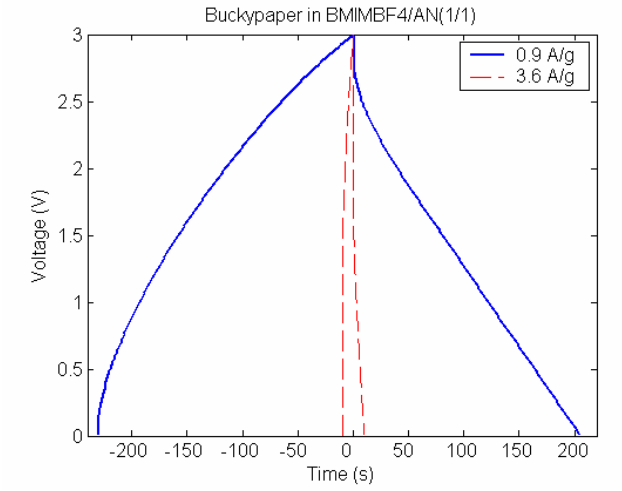

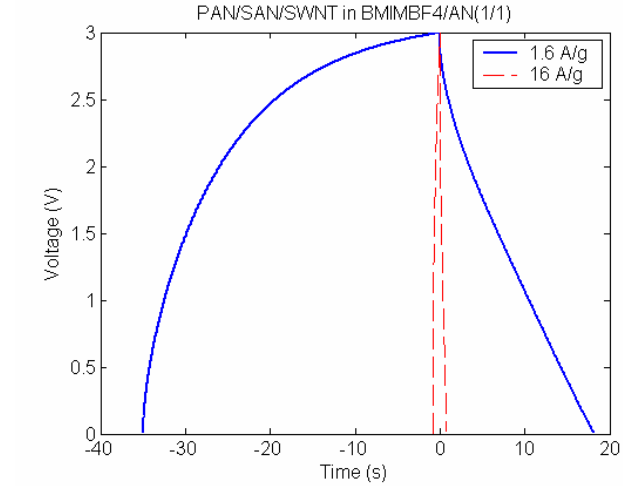

Figure 5.3. continued

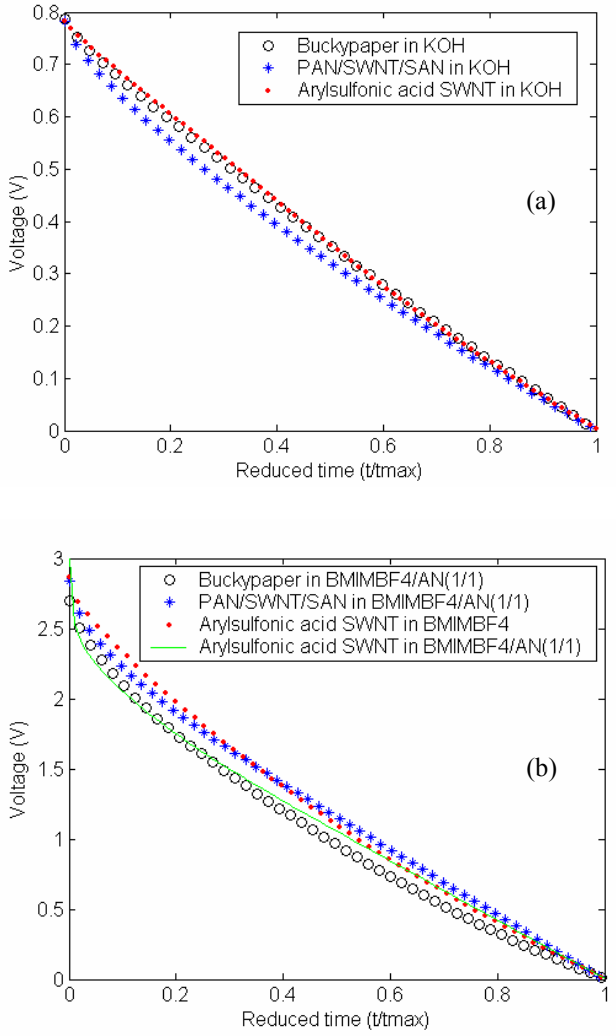

Figure 5.4. Constant current discharging behavior of bucky paper, PAN/SWNT/SAN (63/7/30) and arylsulfonic acid functionalized SWNT(JLH-72) at (a) 6 M KOH, and (b) Ionic liquid. Arylsulfonic acid functionalized SWNT is evaluated in neat BMIMBF4 and BMIMBF4/AN(1/1), and the other two are in BMIMBF4/AN(1/1). The current is 1 mA.

5.3.4 Cyclic Voltammetry

The specific capacitance is also evaluated by cyclic voltammetry with different scan rates. Typical cyclic voltammetric curves are displayed with scan rates of 10, 20, and 50 mV/s in Figure 5.5 and Figure 5.6. In the aqueous electrolyte,

bucky paper and arylsulfonic acid functionalized SWNT (JLH-72) voltammetric curves are closer to the ideal parallelogram shape, in which no pseudocapacitance or very little contribution from redox reaction is observed (Figure 5.5). At a given voltage, PAN/SWNT/SAN shows higher current density than the other two specimens, thus the specific capacitance of PAN/SWNT/SAN electrodes is about 3 times higher than that of bucky paper and arylsulfonic acid functionalized SWNT electrodes in 6 M KOH. However, the voltammetric curve's shape in ionic liquid electrolyte (Figure 5.6) is much different from that in 6 M KOH for all these materials. The redox peak is not observed in ionic liquid, which is also similar to the literature finding.[21] This voltammetric curves change their shapes due to the detrimental of functional groups on the SWNT electrode surface at high voltage window (~3 V) in ionic liquid.[16] Arylsulfonic acid functionalized SWNT in neat BMIMBF4 exhibits the highest specific capacitance among the three materials.

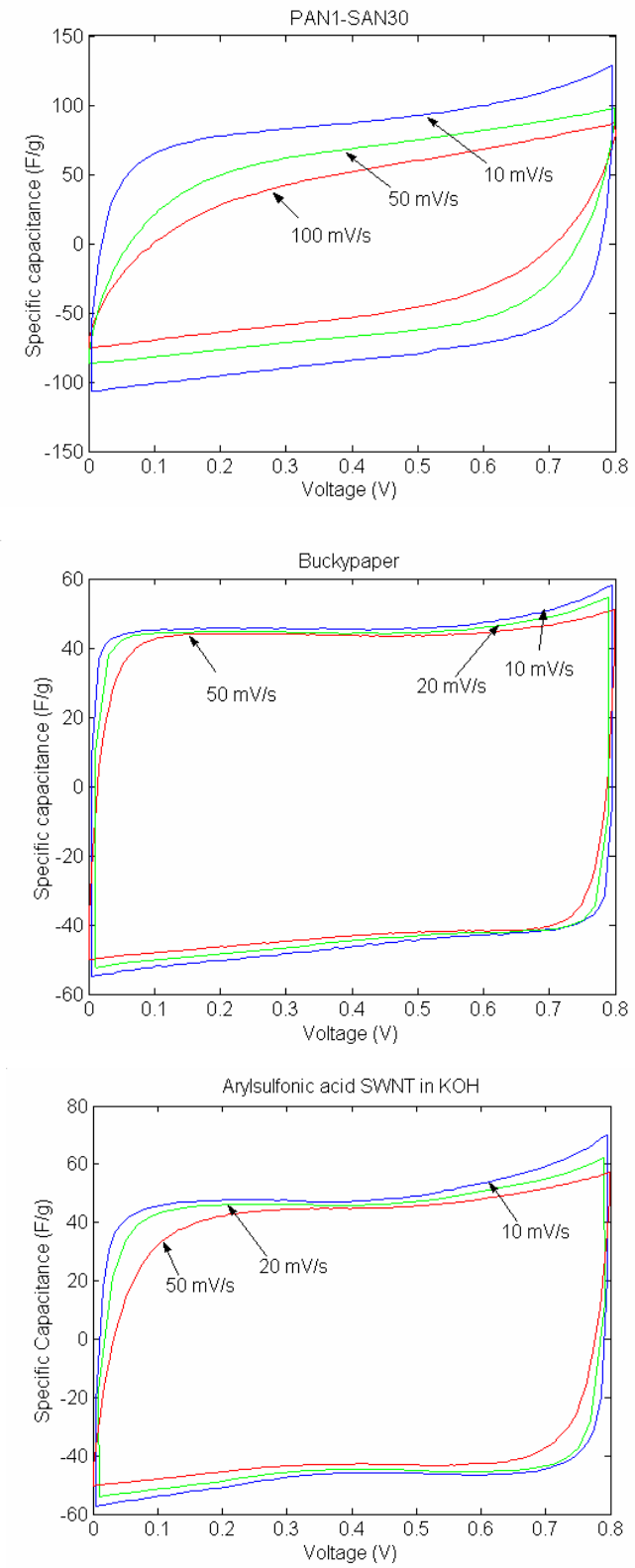

Figure 5.5. Cyclic voltametry of bucky paper, PAN/SWNT/SAN(63/7/30), and arylsulfonic acid functionalized SWNT (JLH-72) with scan rates of 10, 20 and 50 mV/s in 6 M KOH.

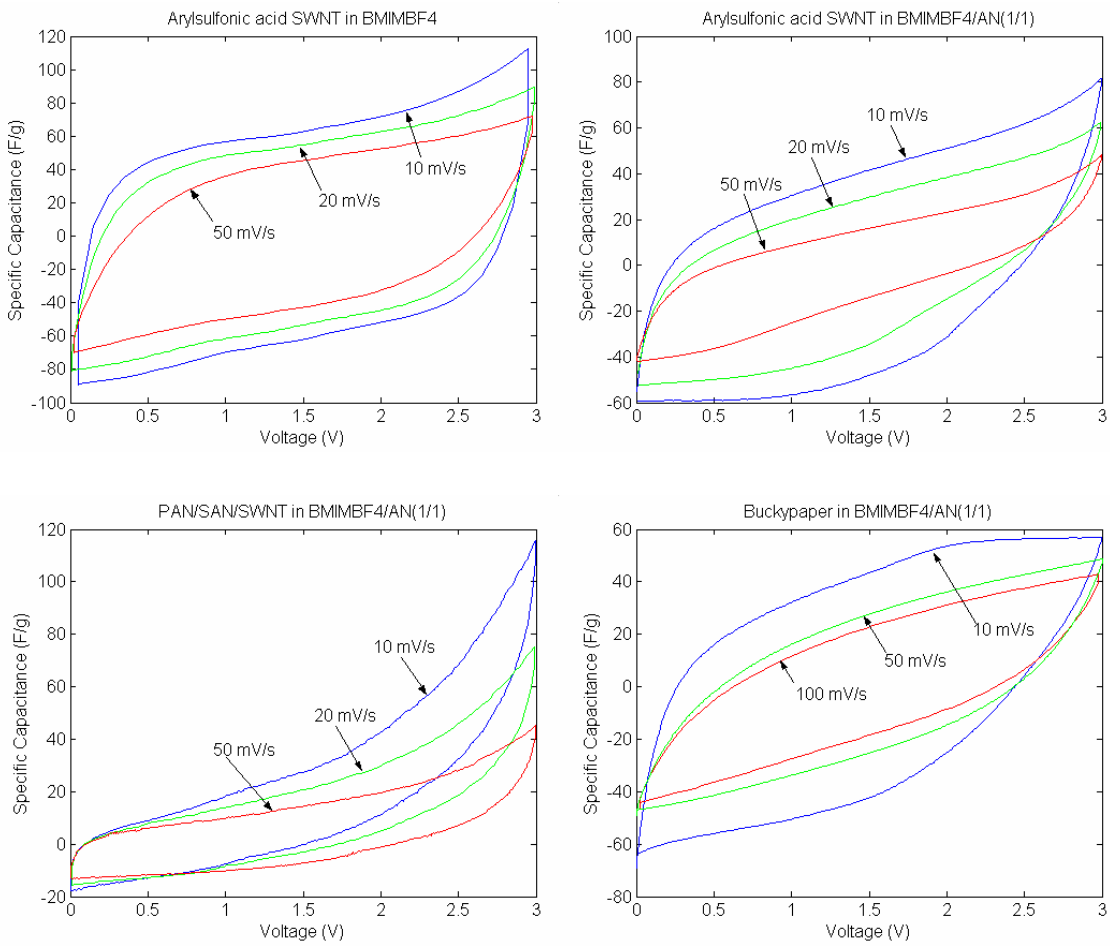

Figure 5.6. Cyclic voltametry of bucky paper, PAN/SWNT/SAN(63/7/30), and arylsulfonic acid functionalized SWNT (JLH-72) with scan rates of 10, 20 and 50 mV/s in ionic liquid.

Current density data obtained at different scan rates at a given voltage (0.1 V) for these ternary composites is plotted as a function of scan rate in Figure 5.7. In 6 M KOH aqueous solution, the linear fitting is very good for each sample. Similar features are observed for bucky paper, carbonized PAN/SWNT/SAN film in BMIMBF4/AN(1/1) and arylsulfonic acid SWNT in neat BMIMBF4. However, nonlinear behavior is observed for arylsulfonic acid SWNT in BMIMBF4/AN(1/1).

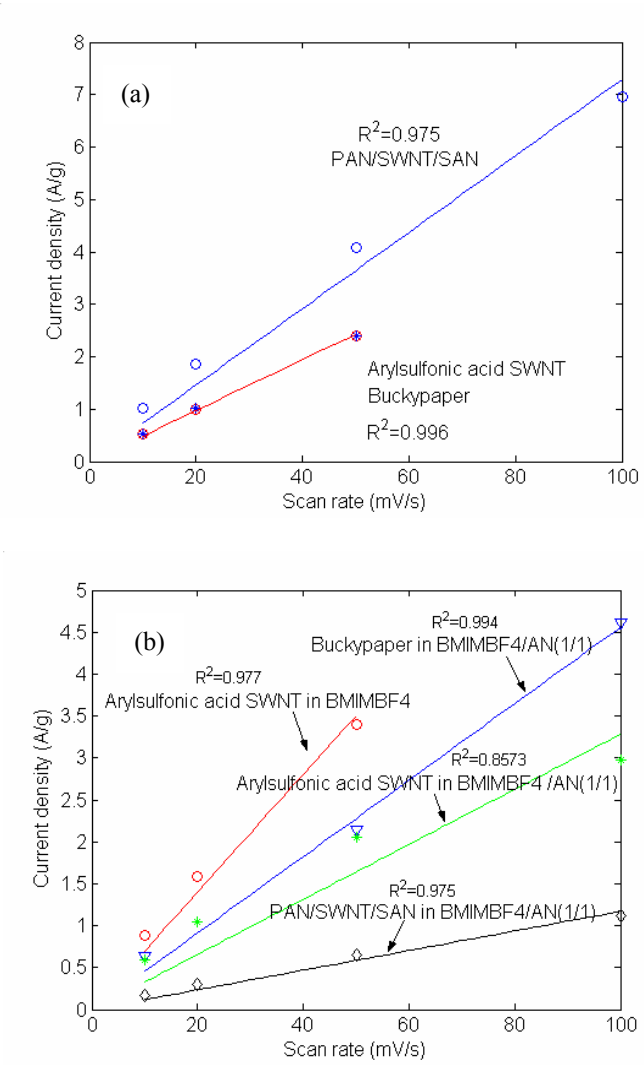

Figure 5.7. Plot of current density as a function of scan rate for PAN/SWNT/SAN (63/7/30) ternary composite film. R^2 is the correlation coefficient. (a) 6 M KOH; (b) BMIMBF4 or BMIMBF4/AN.

5.3.5 Correlation of Capacitance with Surface Area and Electrolyte

The capacitance of these materials as a function of current density is shown in Figure 5.8. The specific capacitance of all the three samples decreases as the current density increases. This is because some of the surface area can not be efficiently accessed at high current density. In high surface area carbon based supercapacitors,

the charging/discharging rate and the accessibility of the electrolyte to the electrodes surface ultimately determine the realizable capacitance.[15] PAN/SWNT/SAN shows much higher capacitance in 6 M KOH aqueous solution than that in ionic liquid/acetonitrile (1:1 volume ratio) (Figure 5.8a). The value in 6 M KOH is about 120 F/g at a current density of 1 A/g, and still greater than 70 F/g at a very high current density of 20 A/g. This behavior is commonly observed for porous carbon electrodes.[15,18] Because the ion size of the ionic liquid is much bigger than that of KOH, the surface area from micropores may not be accessed.[26,27] Extensive studies on the capacitance performance of porous electrodes reveal that, due to the overlapping effect of the electrical double layer, it is more difficult for the electrolytes to access the small sized pores.[28,29,30,31,32,33] The capacitance limits of high surface area activated carbons for double layer capacitors are due to the limit of the space charge capacitance of the solid, and if the pore width is less than 1 nm, the two adjacent space charge regions inside the solid begin to overlap, hence decreasing the capacitance.[34] The relations between ions in the electrolyte and pore dimensions in carbon electrodes have been investigated in detail.[35]

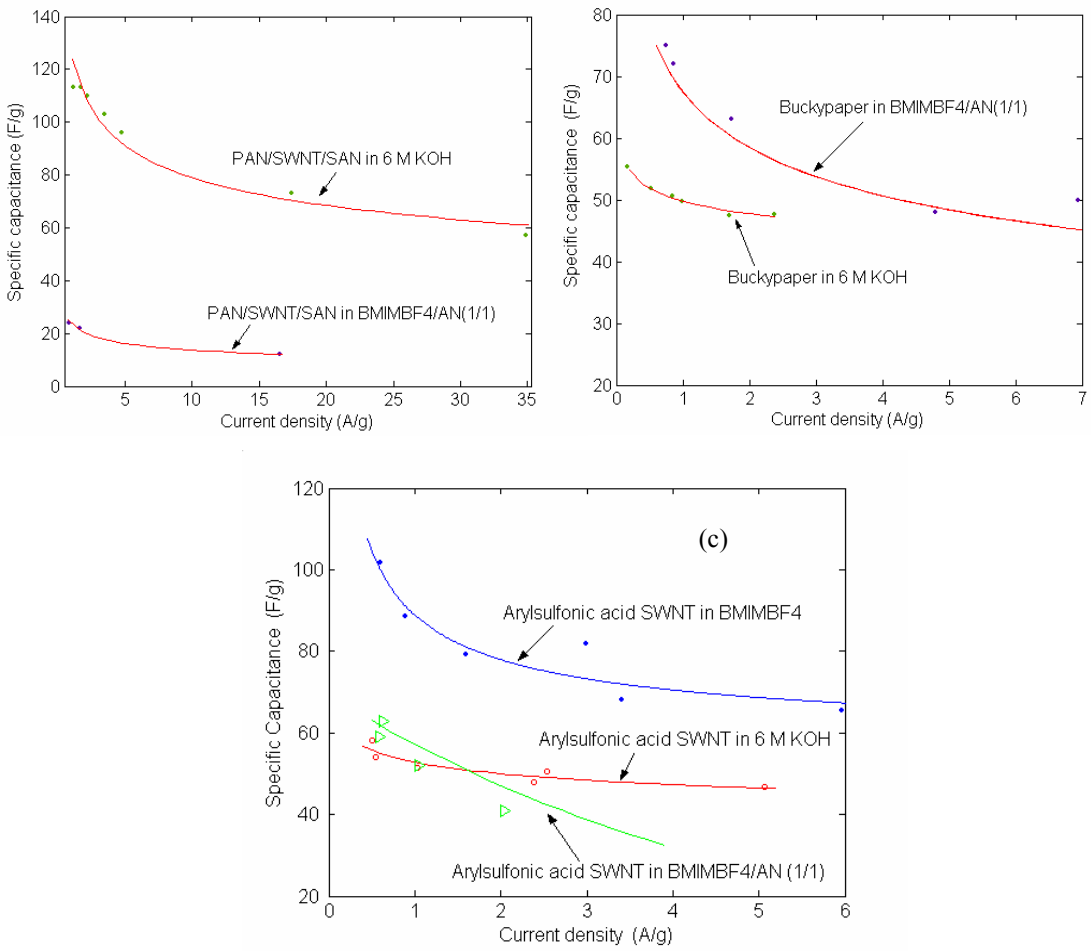

Figure 5.8. Specific capacitance for various samples as a function of current density. (a) PAN/SWNT/SAN(63/7/30), (b) bucky paper, and (c) arylsulfonic acid functionalized SWNT (JLH-72) in different electrolytes.

The contact angle micrographs of bucky paper and carbonized PAN/SWNT/SAN films in BMIMBF4 and 6 M KOH are shown in Figure 5.9. The value of contact angle of PAN/SAN/SWNT in 6 M KOH aqueous solution is about 58 ± 4, while its contact angle value in BMIMBF4/AN (1/1) is less than 10, which is completely wetting (Table 5.2). Therefore, this observation shows that PAN/SWNT/SAN has stronger affinity to ionic liquid than to 6 M KOH aqueous solution. Contact angle data does not support the observed capacitance behavior.

Table 5.2. Contact angle of bucky paper, PAN/SWNT/SAN(63/7/30), and arylsulfonic acid functionalized SWNT (JLH-72) for different electrolytes

	6 M KOH	**BMIMBF4/AN (1/1)**	**BMIMBF4/AN (2/1)**	**BMIMBF4**
Bucky paper	101 ± 3	22 ± 3	< 10	21 ± 4
Arylsulfonic acid SWNT (JLH-72)	56 ± 4	---	----	19 ± 2
PAN/SWNT/SAN (63/7/30)	58 ± 4	< 10	----	---

Contact angle < 10: completely wetting

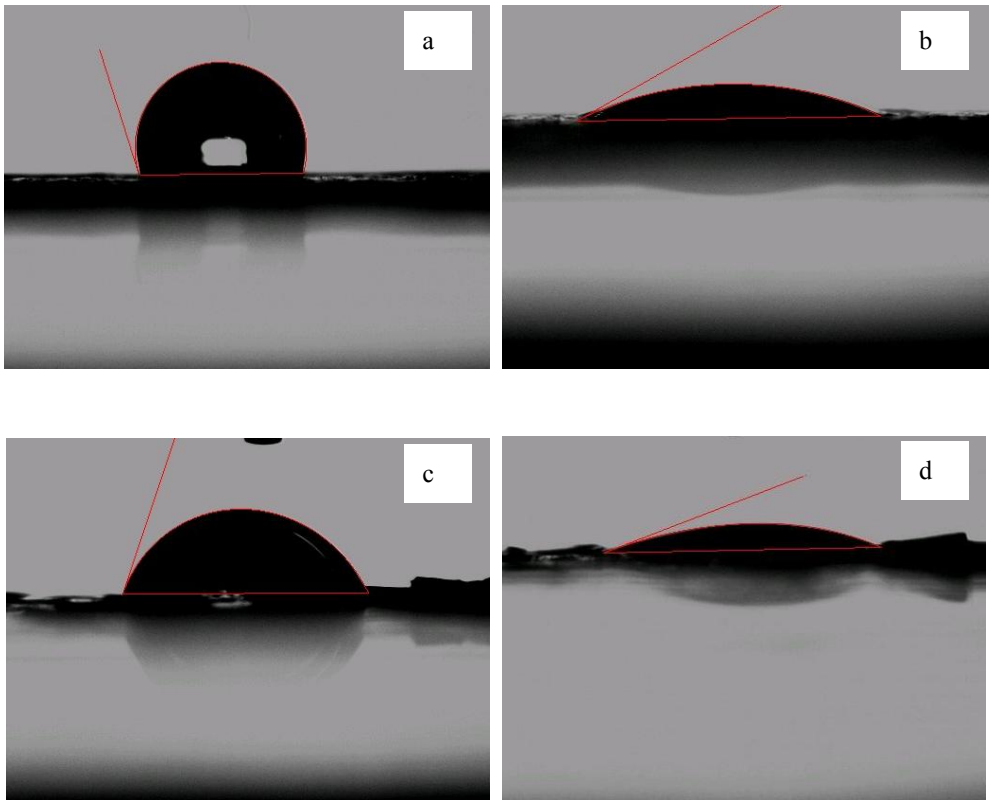

Figure 5.9. Micrographs of contact angle of bucky paper and carbonized PAN/SWNT/SAN for BMIMBF4 and 6 M KOH. (a) 6 M KOH on Bucky paper; (b) BMIMBF4 on Bucky paper; (c) 6 M KOH on carbonized PAN/SWNT/SAN(63/7/30); (d) BMIMBF4 on carbonized PAN/SWNT/SAN(63/7/30).

PAN/SWNT/SAN membranes submerged in BMIMBF4/AN (1/1) for 10 minutes resulted in increased weight by 76%, while PAN/SWNT/SAN membranes submerged in 6 M KOH aqueous solution for the same amount of time increased 133% by weight (Table 5.3). This observation indicates that although the affinity, as measured by contact angle, in 6 M KOH solution is worse than that in BMIMBF4/AN mixture, the swelling of PAN/SWNT/SAN in KOH is much better than that in ionic liquid. The swelling behavior explains the observed capacitance behavior.

Table 5.3. Electrolyte adsorption of different electrodes

	Electrolyte	Original Mass(mg)	Mass After adsorption (mg)	Mass ratio (%)
PAN/SWNT/SAN (63/7/30)	BMIMBF4/AN(1/1)	1.80	3.16	176
	6 M KOH	1.45	3.38	233
Arylsulfonic acid SWNT (JLH-72)	BMIMBF4	3.47	6.48	187
	6 M KOH	2.16	4.09	189
Bucky paper	BMIMBF4/AN(1/1)	4.13	7.95	192
	BMIMBF4	3.17	6.76	213
	6 M KOH	4.09	7.17	175

Although the surface area of arylsulfonic acid functionalized SWNT is much smaller than that of bucky paper as shown in Table 5.1, the two carbon nanotube film based electrodes have comparable specific capacitance values in 6 M KOH aqueous

solution. An interesting finding in these materials is that the capacitance of these two carbon nanotube film electrodes in ionic liquid/acetonitrile is higher than that in 6 M KOH, especially for arylsulfonic acid functionalized SWNT (JLH-72) (Figure 5.8c). The improvement in the specific capacitance of arylsulfonic acid functionalized SWNT in ionic liquid electrolyte is about 50% to 70% even at 5 A/g (Figure 5.8b). However, the capacitance value of arylsulfonic acid functionalized SWNT (JLH-72) in ionic liquid/acetonitrile (1/1) is comparable to that in 6 M KOH. Similar behavior is also observed in pure ionic liquid and ionic liquid/acetonitrile with volume ratio of 2:1 for bucky paper electrodes (Figure 5.10). In the literature, there are several reports about carbon nanotube or other carbon materials based electrodes in ionic liquid.[16,19] However, the fact that a carbon film has higher capacitance in ionic liquid than in 6 M KOH aqueous solution has never been reported. We propose that this phenomenon results from the strong affinity between carbon nanotube and 1-butyl-3-methyl- imidazolium tetrafluoroborate. In order to explain this phenomenon, the contact angle measurement for arylsulfonic acid functionalized SWNT and bucky paper in both 6 M KOH and ionic liquid were conducted. Table 5.2 shows that arylsulfonic acid functionalized SWNT and bucky paper have much lower values of contact angle in ionic liquid than in 6 M KOH, which confirms our hypothesis. The strong interactions make double layer with higher charge density, so that more energy can be stored in the unit space. The weight increases of arylsulfonic acid functionalized SWNT in 6 M KOH and in BMIMBF4 are 87% and 89%, respectively (Table 5.3). This indicates that the swelling behaviors of

arylsulfonic acid functionalized SWNT in 6 M KOH and in BMIMBF4 are comparable. However, bucky paper has higher swelling ability both in BMIMBF4/AN(1/1) and BMIMBF4 than in 6 M KOH (Table 5.3). Arylsulfonic acid functionalized SWNT has higher capacitance as compared to the control bucky paper. This is attributed to good interactions between functionalized carbon nanotube and ionic liquid.

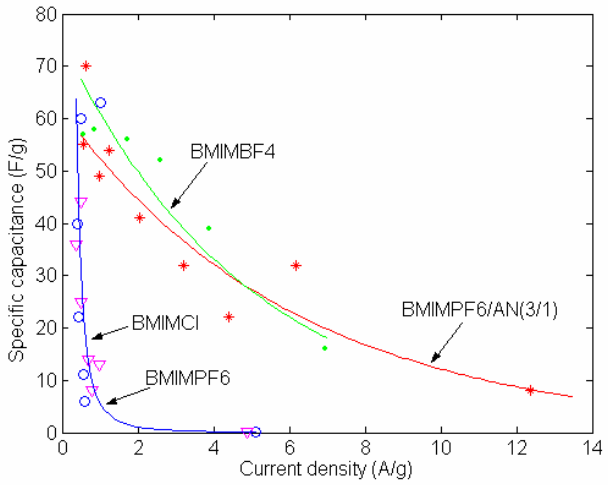

Figure 5.10. Bucky paper electrode evaluated as a function of current density using different ionic liquids.

Higher capacitance in BMIMBF4 than in 6 M KOH has been observed for bucky paper and arylsulfonic acid functionalized SWNT membrane electrodes. It is very interesting to know whether this phenomenon is a general observation for ionic liquid. Therefore two more ionic liquids, BMIMPF6 and BMIMCl were used as electrolyte for the capacitance evaluation. The results show that BMIMCl and BMIMPF6 are not as good as BMIMBF4 because the specific capacitance of the

bucky paper electrodes almost drops from 60 F/g down to a few F/g at a current density of 2 A/g in these two electrolytes (Figure 5.10). However, the contact angles of these electrolytes on bucky paper are similar to each other (Table 5.4). The capacitance performance in BMIMCl and BMIMPF6 is even worse than that in 6 M KOH aqueous solution. However, bucky paper electrode in a mixture of BMIMPF6 and acetonitrile with a volume ratio of 3 to 1 shows comparable performance to that in neat BMIMBF4. It is concluded that the bucky paper electrode performance in other ionic liquids (BMIMCl and BMIMPF6) is not good as in BMIMBF4. Although BMIMBF4 and BMIMPF6 have similar conductivity, around 1.9 – 2.3 mS/cm, and the double layer capacity of activated carbon in these two electrolytes is within the range of 5.2 – 6.1 μF/cm^2.[16]

Table 5.4. Contact angle of different electrolytes on bucky paper

	BMIMCl	BMIMPF6	BMIMPF6/AN(3/1)	BMIMBF4
Bucky paper	22 ± 3	21 ± 6	< 10	21 ± 4

Contact angle < 10: completely wetting

5.3.6 The Effect of Electrolyte Concentration on Capacitance

The concentration of the electrolyte is a critical factor for supercapacitor performance, especially those supercapacitors operating at high current density. The bucky paper electrodes were evaluated in mixtures of BMIMBF4/acetonitrile with different concentration, and the performance behavior as a function of current density

is shown in Figure 5.11a. At low current density, there is no significant difference for the three electrolytes. However, with increasing the current density, the specific capacitance of bucky paper electrodes decreases rapidly in neat ionic liquid, but keeps constant in a mixture of BMIMBF4/acetonitrile with a volume ratio of 2 to 1. Further diluting the ionic liquid is detrimental to the capacitance performance of the electrodes(Figure 5.11b). This observation can be explained by the viscosity variation of pure ionic liquid. On the one hand, incorporation of acetonitrile dilutes the electrolyte and facilitates the ion migration into the electrode pores. On the other hand, too diluted electrolyte can't provide enough ions at high current density, and also increases the internal resistance which deteriorates the power density of the cell. Hence, there is a critical electrolyte concentration for supercapacitors. Among the three electrolytes with different concentration, BMIMBF4/acetonitrile (2/1) shows the best performance. Table 5.2 shows that the BMIMBF4 and BMIMBF4/AN(1/1) on bucky paper have almost the same contact angle values, which are about 22 ± 3, while the value for BMIMBF4/AN(2/1) on bukcypaper is smaller, which is completely wetting. Therefore, bucky paper electrode has stronger affinity with BMIMBF4/AN (2/1) than with BMIMBF4 and BMIMBF4/AN(1/1). The significant influence of ion concentration in the non-aqueous electrolyte on the performance of activated carbon based double layer capacitor has also been reported in the literature, and it was found that the power performance is strongly dependent on the salt concentration in the electrolyte.[36] In 0.16 M tetraethylammonium tetrafluoroborate/propylene carbonate (Et_4NBF_4/PC), the capacitor can be charged to 3 volts without changing its

capacitance significantly, while in 0.053 M Et_4NBF_4/PC, the capacitor can be only charged to less than 1.0 volt.[36] The capacitance of the electrode materials limits the maximum energy stored in the capacitor with high-salt-concentration electrolytes, while the maximum operating voltage as well as the maximum energy increases with increasing salt concentration in the capacitor with low-salt-concentration electrolytes because ion concentration is limited in such electrolytes.[36]

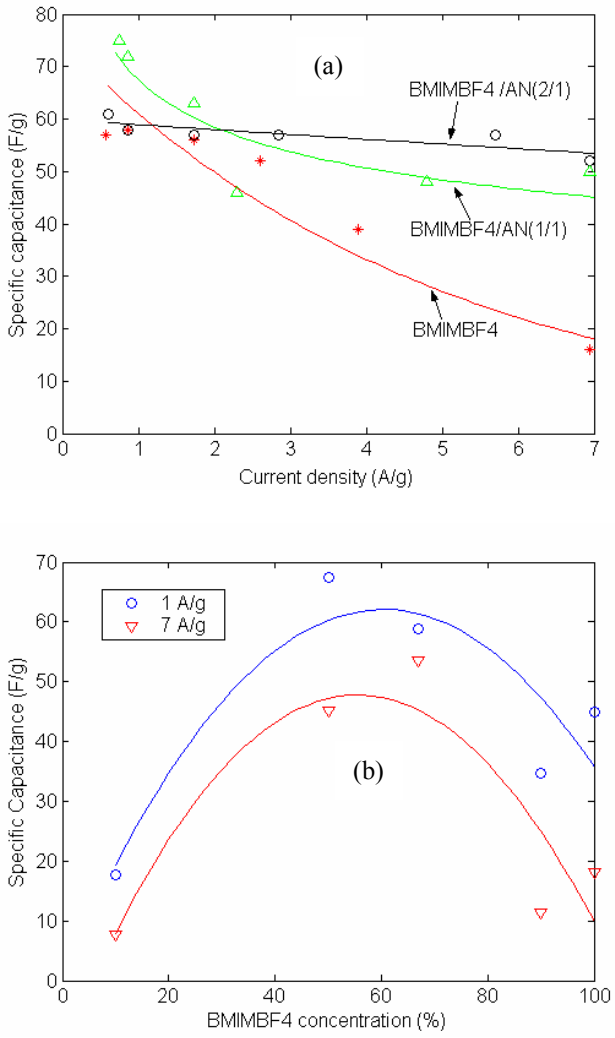

Figure 5.11. The effect of the ionic liquid concentration on the capacitance of bucky paper electrodes.

5.3.7 The Effect of Electrolyte on Cyclability

The capacitance performance of bucky paper electrodes in different ionic liquid electrolytes is evaluated for thousands of cycles (Figure 5.12). In the mixture of BMIMPF6 and acetonitrile (3:1 volume ratio), the capacitance of bucky paper decreased to about 55% after 3500 charging/discharging cycles. While in BMIMBF4/acetonitrle (1:1), the specific capacitance of bucky paper decreases very rapidly in the first 600 cycles, and then tends to a steady value. There is only 25% loss in capacitance value even after 10000 cycles (Figure 5.12). The capacitance performance loss is mainly due to the equivalent series resistance increase, which may be caused by a deterioration of the electrode material/current collector contact at both the positive and negative electrodes. On the other hand, the anion PF_6 is much bigger and is more difficult to diffuse than anion BF_4, so some of the surface area may not be accessed by PF_6, although the anodic electrochemical stability of BF_4 is lower than that of PF_6.[37]

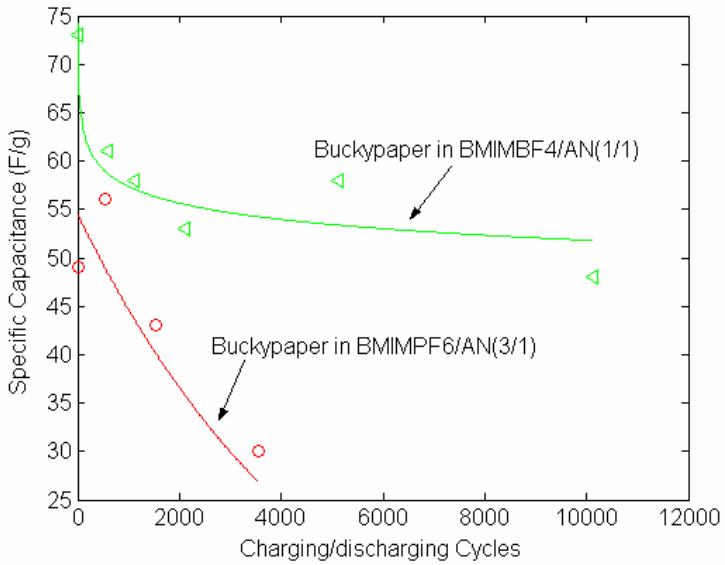

Figure 5.12. The long term performance of the bucky paper electrodes in ionic liquid with a current of 1 mA in BMIMBF4/AN and a scan rate of 20 mV/s in BMBMPF6/AN.

5.3.8 Impedance Spectroscopy

The electrochemical impedance behavior of the three specimens in aqueous and nonaqueous electrolytes is shown in Figure 5.13. In 6 M KOH aqueous solution, PAN/SWNT/SAN(63/7/30), bucky paper, and arylsulfonic acid functionalized SWNT (JLH-72) based supercapacitors show a depressed semicircle in the high frequency region (Figure 5.13a). At intermediate frequencies, there is a straight line with a slope of approximately 45° for bucky paper and PAN/SWNT/SAN(63/7/30) based capacitors, which is a common observation.[25] The slope of arylsulfonic acid functionalized SWNT is much lower. In the ionic liquid electrolytes, PAN/SWNT/SAN(63/7/30) shows depressed semicircle again in the high frequency region, displaying a straight line with 45° at intermediate frequencies (Figure 5.13b).

(a)

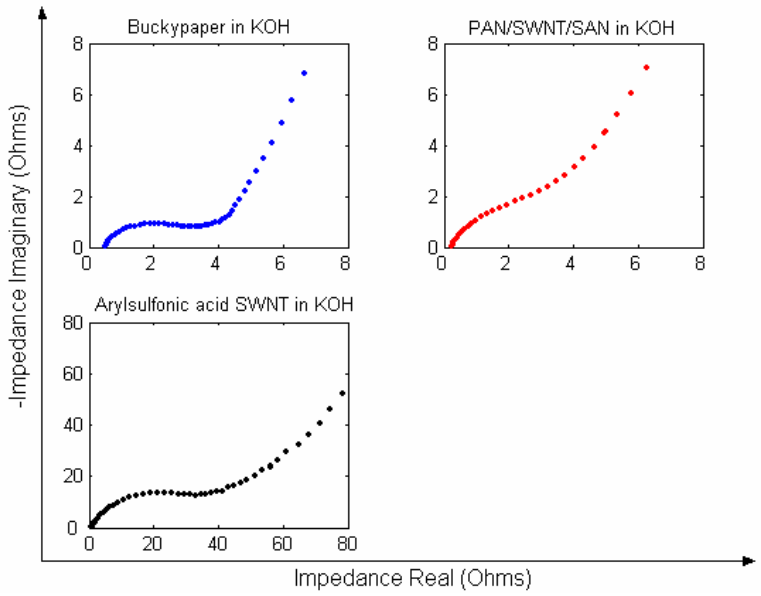

(b)

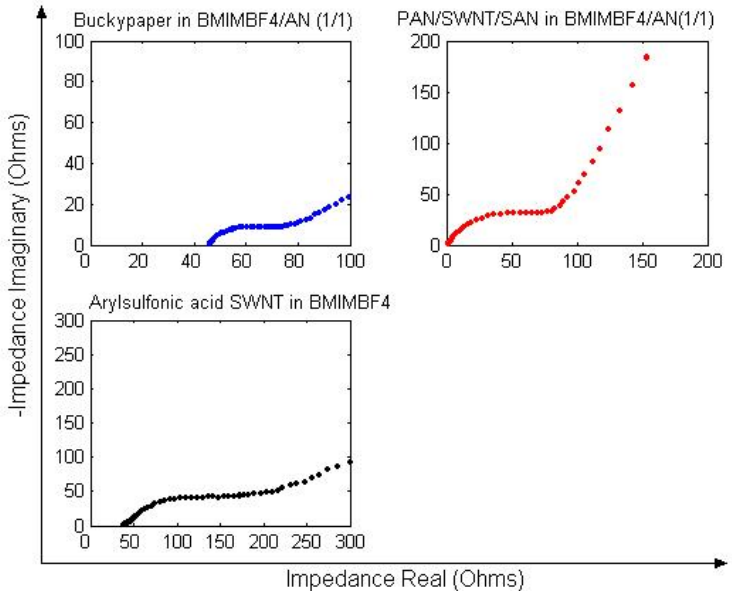

Figure 5.13. Nyquist impedance spectra of the bucky paper, PAN/SWNT/SAN (63/7/30) and arylsulfonic acid functionalized SWNT(JLH-72) electrodes obtained in (a) 6 M KOH, and (b) ionic liquid (BMIMBF4)/AN.

However, bucky paper and arylsulfonic acid functionalized SWNT based supercapcitors exhibit an approximately 45° slope throughout most of their frequency, which is due to the pore resistance of the electrodes and an increase in the resistivity

of the electrolyte. Similar observations are reported regarding to the carbon nanotubes in ionic liquids.[21] In addition, the intercepts on real impedance represent the ionic resistance of the solution in the separator. In 6 M KOH, it can be seen that all these materials show similar equivalent series resistance (ESR), about 0.5 Ω. The internal resistance of the bucky paper and arylsulfonic acid functionalized SWNT based supercapacitors in ionic liquids is about 50 Ω which is higher as compared to the commercial supercapacitor with 1.4 M tetraethylammonium tetrafluoroborate in acetonitrile.[38] It is comparable to Barisci et al's results.[21] However, the ESR of PAN/SWNT/SAN based supercapacitor in BMIMBF4/AN is almost the same as that in 6 M KOH. If the internal resistance of these supercapacitors in ionic liquid can be decreased to a similar level, the power density of the supercapacitor can be much improved.

5.3.9 Elemental Analysis

XPS shows that buckyper, carbonized PAN/SWNT/SAN(63/7/30) film and arylsulfonic acid SWNT membrane all contain oxygen (Table 5.5). Arylsulfonic acid SWNT membrane has about 13% oxygen due to oxidation occurrence during the functionalization.

Table 5.5. Atomic compositions on SWNT and functionalized SWNTs electrode surface obtained from XPS

	C (%)	O (%)	S (%)	N (%)
Bucky paper	96.0	4.0	--	--
PAN/SWNT/SAN(63/7/30)	81.2	17.2	--	1.7
Arylsulfonic acid SWNT(JLH-72)	85.8	13.0	1.3	--

5.4 Conclusions

The capacitance of three different carbon materials has been investigated in 6 M KOH aqueous solution and in ionic liquids. PAN/SWNT/SAN (63/7/30) has almost 6 times higher capacitance in 6 M KOH than in ionic liquid. This can be explained by the electrode's swelling behavior in these two electrolytes. Higher capacitance in ionic liquid than that in 6 M KOH aqueous solution is observed for bucky paper and arylsulfonic acid functionalized bucky paper. Especially for arylsulfonic acid functionalized bucky paper (JLH-72), there is 50% to 70% improvement in capacitance, which is opposite to the general observation. This behavior results from the strong affinity between 1-butyl-3-methylimidazolium tetrafluoroborate and SWNT, which is consistent with contact angle measurements. The effect of ionic liquid concentration on the capacitance performance of bucky paper has been studied. The results show that there is a critical electrolyte concentration for obtaining high capacitance. Stable supercapacitor behavior has been observed for carbon nanotube electrodes. The electrochemical behaviors of these samples are also characterized by impedance spectroscopy.

5.5 References

1 J. G. Huddleston, A. E. Visser, W. M. Reichert, H. D. Willauer, G. A. Broker, R. D. Rogers. *Green Chemistry* **2001**, ***3****(4)*, 156.

2 H. L. Ngo, K. LeCompte, L. Hargens, A. B. McEwen. *Thermochim. Acta* **2000**, *357*, 97.

3 S. Seki, Y. Kobayashi, H. Miyashiro, Y. Ohno, A. Usami, Y. Mita, M. Watanabe, N. Terada. *Chem Commun (Camb)* **2006**, *5*, 544.

4 K. Hayashi, Y. Nemoto, K. Akuto, Y. Sakurai. *NTT Technical Review* **2004**, *2 (9)*, 48.

5 H. Liu, P. He, Z. Li, Y. Liu, J. Li, L. Zheng, J. Li. *Electrochem. Solid-State Lett.* **2005**, *8(7)*, J17.

6 J. D. Stenger-Smith, C. K. Webber, N. Anderson, A. P. Chafin, K. Zong, J. R. Reynolds. *J. Electrochem. Soc.***2002**, *149(8)*, A973.

7 R. D. Rogers, K. R. Seddon. *Ionic Liquids As Green Solvents :Progress and Prospects*, Oxford University Press, **2003**.

8 Á. Mercedes, C. Esther, F. Belen, G. Hermenegildo, H. José R. *Photochemistry and Photobiology* **2005**, *82 (1)*, 185.

9 M. C.-Y. Tang, K.-Y. Wong, T. H. Chan. *Chemical Communications* **2005**, 1345.

10 http://www.merck.de/servlet/PB/menu/1370550/index.html.

11 P. Damlin, C. Kvarnstrom , A. Ivaska. *Journal of Electroanalytical Chemistry* **2004**, *570*, 113.

12 Y. Zhang, Y. Shen, J. Li, L. Niu, S. Dong, and A. Ivaska. *Langmuir* **2005**, *25(11)*, 4797.

13 L. Kavan and L. Dunsch. *Chem. Phys. Chem.* **2003**, *4*, 944.

14 R. J. Gale, R. A. Osteryoung. *Electrochimica Acta* **1980**, *25*, 1527.

15 C. Nanjundiah, S. F. McDevitt, V. R. Koch. *J. Electrochem. Soc.* **1997**, *144(10)*, 3392.

16 A. Lewandowski, M. Galinski. *Journal of Physics and Chemistry of Solids* **2004**, *65*, 281.

17 A. Balducci, W. A. Henderson, M. Mastragostino, S. Passerinic, P. Simon, F. Soavi. *Electrochimica Acta* **2005**, *50*, 2233.

18 E. Frackowiak, G. Lota, J. Pernak. *Appl. Phys. Lett.* **2005**, *86*, 164104.

19 Y. -J. Kim, Y. Matsuzawa, S. Ozaki, K. C. Park, C. Kim, M. Endo, H. Yoshida, G. Masuda, T. Sato, M. S. Dresselhaus. *J. Electrochem. Soc.* **2005**, *152(4)*, A710.

20 M. Ue, M. Takeda, A. Toriumi, A. Kominato, R. Hagiwara, Y. Ito. *J. Electrochem. Soc.* **2003**, *150(4)*, A499.

21 J. N. Barisci, G. G Wallace, D. R. MacFarlane, R. H. Baughman. *Electrochemistry Communications* **2004**, *6*, 22.

22 T. Fukushima, A. Kosaka, Y. Ishimura, T. Yamamoto, T. Takigawa, N. Ishii, T. Aida. *Science* **2003**, *300(5628)*, 2072.

23 P. G. Whitten, G. M. Spinks, G. G. Wallace. *Carbon* **2005**, *43(9)*, 1891-1896.

24 C. Zhou, S. Kumar, C. D. Doyle, J. M. Tour. *Chem. Mater.* **2005**, *17*, 1997.

25 B. E. Conway. *Electrochemical Supercapacitors, Scientific Fundamental and Technological Applications*; Plenum Publishers: New York, **1999.**

26 H. Shi. *Electrochim Acta* **1996**, *40(10)*, 1633.

27 D. Qu, H. Shi. *J. Power Sources* **1998**, *74*, 99.

28 A. Soffer and M. Folman. *Journal of Electroanalytical Chemistry and Interfacial Electrochemistry* **1972**, *38*, 25.

29 Y. Oren, H. Tobias, A. Soffer. *Journal of Electroanalytical Chemistry and Interfacial Electrochemistry* **1984**, *162(1-2)*, 87.

30 Y. Oren, A. Soffer. *Journal of Electroanalytical Chemistry and Interfacial Electrochemistry* **1985**, *186*, 63.

31 Y. Oren, A. Soffer. *Journal of Electroanalytical Chemistry and Interfacial Electrochemistry* **1986**, *206*, 101.

32 D. Golub, Y. Oren, A. Soffer. *Journal of Electroanalytical Chemistry and Interfacial Electrochemistry* **1987**, *227*, 41.

33 D. Golub, A. Soffer, Y. Oren. *Journal of Electroanalytical Chemistry and Interfacial Electrochemistry* **1989**, *260*, 383.

34 O. Barbieri, M. Hahn, A. Herzog, R. Kotz. *Carbon* **2005**, *43*, 1303.

35 G. Salitra, A. Soffer, L. Eliad, Y. Cohen, D. Aurbach. *J. Electrochem. Soc.* **2000**, *147(7)*, 2486.

36 J. P. Zheng, T. R. Jow. *Electrochemical Society Proceedings* **1996**, *96-25*, 280.

37 M. Ue, M. Takeda, M. Takehara, S. Mori. *Electrochemical Society Proceedings* **1996**, *96-25*, 289.

38 C. J. Farahmandi, J. M. Dispennette. *US Patent 5777428, US Patent 5621607*.

CHAPTER 6

THE EFFECT OF HEAT TREATMENT ON THE POROUS STRUCTURE AND ELECTROCHEMICAL PROPERTIES OF SWNT MEMBRANES

6.1 Introduction

Porous structure of CNT has received much attention due to its diverse applications.[1,2] As discussed in Chapter 3, chemical functionalization can increase the surface area of CNTs.[3,4] Heat treatment can also affect the surface area.[5] However, these functionalized tubes can be restored to pre-treatment levels by heat treatment, as functional groups are removed, the tubes repair themselves.[5] The morphology and temperature effects on adsorption of hexane on SWNT have been examined both theoretically and experimentally.[6] In order to obtain highly porous CNT structure, it is necessary to control the interstitial pores as well as internal pores. Due to the change in pore structure and surface functionality caused by heat treatment, the electrochemical properties will also change. The pore and surface structures of carbon nanotubes play an important role in supercapacitor applications.[7] There are few reports about the effect of heat treatment on the electrochemical capacitance of CNT.[8,9,10] Hence, in this chapter, we will focus on the effect of heat treatment on the porous structure of CNT membranes and their electrochemical capacitance. The bucky paper described in previous chapters was provided by Carbon Nanotechnologies Inc. (CNI), and its processing is described in the literatures.[11,12]

This bucky paper was made by vacuum filtration of a NaOH aqueous suspension with some surfactant through a poly(tetrafluoroethylene) (PTFE) filter and then washed with deionized water and methanol. These sheets were dried under continued vacuum purge for 1 hour before being peeled from the filter paper. In this chapter, the bucky paper is prepared from dimethylformamide (DMF) suspension as DMF is a relatively good solvent for CNT. The second type of bucky paper studied in this chapter was functionalized using nitric acid.

6.2 Materials and Experiment

In a typical unfunctionalized bucky paper preparation procedure, 50 mg SWNTs (HiPCO single wall carbon nanotube with 70% purity obtained from CNI) were dispersed into 50 mL DMF. This dispersion was sonicated in a Fisher Scientific bath sonicator (frequency 43 kHz, power 150 W) for 24 hours followed by filtration through PTFE filter paper (1.0 μm pore size, Gelman Laboratory) under water pump pressure and repeatedly washed with distilled water. The resulting bucky paper (thickness ~ 70 μm) was peeled off from the filter paper and vacuum dried at 70 °C for about a week. Similar procedure was applied to prepare thicker bucky paper (thickness ~ 350 μm) by using 350 mg SWNTs and 350 mL DMF.

In the SWNT functionalization procedure, 70 mg SWNTs (HiPCO single wall carbon nanotube with 70% purity obtained from CNI) were dispersed in 70 mL 6 M nitric acid. This dispersion was sonicated for 2 hours in a bath sonicator (frequency 43 kHz, power 150 W, Fisher Scientific) followed by refluxing for about 2

hours at 100 °C. The refluxed dispersion was filtered through PTFE filter paper to form a film and repeatedly washed with distilled water. The resulting functionalized bucky paper was dried in vacuum at 70 °C for about a week.

Both the functionalized and unfunctionalized bucky papers were heated to 650 °C at a heating rate of 50 °C/min and then kept at 650 °C for 2 hours in a tube furnace (Tube furnace 21100, Barnstead /Thermolyne) under nitrogen flow. Various samples and their designations are given in Table 6.1. Other experimental procedures are described in Chapter 2.

Table 6.1. Sample treatments and their designations

Sample	Treatments
B70	Buckypaper processed from DMF (thickness: 70 µm)
B70H	Buckypaper processed from DMF (thickness: 70 µm). Heat Treated at 650 °C in nitrogen
B70F	Nitric acid functionalized buckypaper(thickness: 70 µm)
B70FH	Nitric acid functionalized buckypaper(thickness: 70 µm). Heat treated at 650 °C in nitrogen
B350	Buckypaper processed from DMF (thickness: 350 µm)
B350H	Buckypaper processed from DMF (thickness: 350 µm). Heat treated at 650 °C in nitrogen

6.3 Results and Discussion

In order to determine the porosity parameters, N_2 adsorption and desorption isotherms were measured for these bucky papers as shown in Figure 6.1. The N_2 isotherm curves for these samples are of type V, which indicates that the adsorptive molecules have greater affinity for one another than they do for the bucky paper samples.[13] This type of isotherm curve is also often associated with narrow slit-like pores. [14]

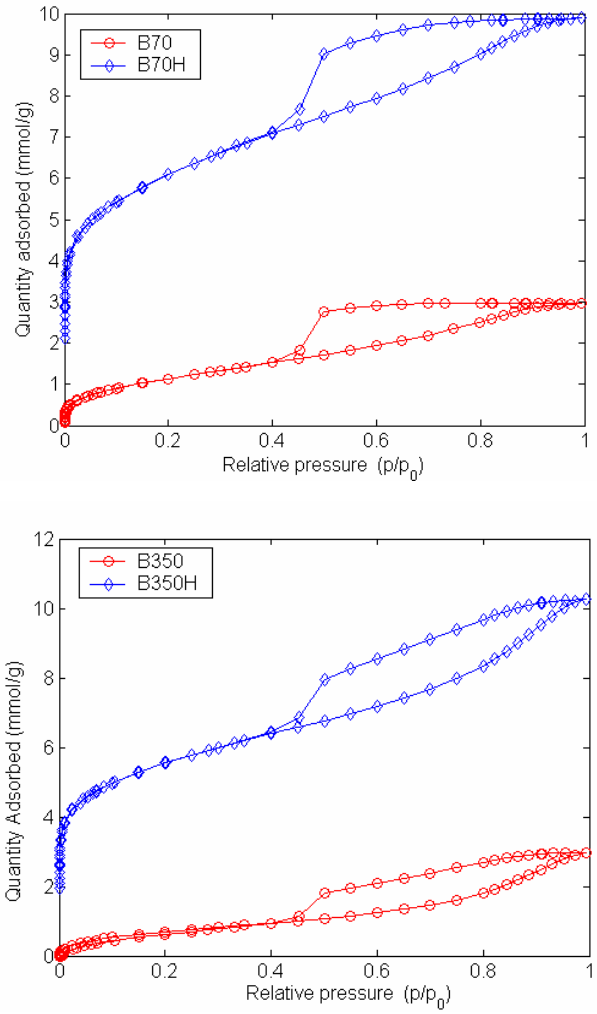

Figure 6.1. Isotherm N_2 adsorption and desorption of samples B70, B70H, B350 and B350H.

Figure 6.1 also shows that N_2 adsorption and desorption uptake increases significantly after heat treatment. This indicates enhanced adsorbent-adsorbate interactions. Comparison between B350 (or B350H) and B70 (or B70H) also suggests that thickness does not affect the isothermal type. In order to determine the pore size distribution of these SWNT membranes, their isotherm curves were analyzed by density function theory (DFT) method. Figure 6.2 shows the pore size distribution of these bucky papers.

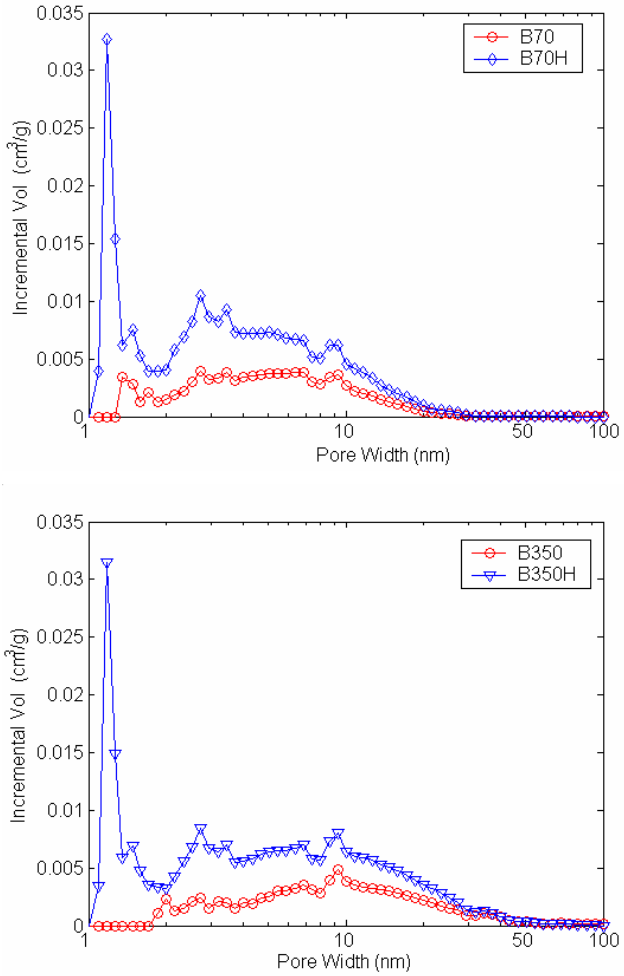

Figure 6.2. Pore size distribution of bucky paper with different thicknesses and heat treatment. Sample designations are given in Table 6.1.

The pore-structural parameters of these samples are summarized in Table 6.2. The results show that heat-treatment remarkably increases the total surface area and pore volume. The surface areas and pore volumes of both the 70 and 350 μm thick samples are comparable within experimental error. The amorphous carbon in SWNT membranes burns out during the heat treatment at 650 °C,[15] resulting in enhanced porosity, pore volume, and surface area accessible for N_2 absorption. Functionalization of bucky paper will also increase the surface area and pore volume after heat treatment due to the elimination of functional groups from blocking interstitial pores.[1,14]

Table 6.2. Pore structure parameters of various bucky papers. Sample designations are given in Table 6.1

		B70	**B70H**	**B350**	**B350H**
BET surface area (m^2/g)		96	457	61	414
Pore volume (cm^3/g)		0.10	0.34	0.10	0.36
DFT	Surface area (m^2/g)	50	204	31	190
	Total pore volume (cm^3/g)	0.10	0.30	0.10	0.32
	Micro volume (cm^3/g)	0.013	0.083	0.003	0.077
	Meso volume (cm^3/g)	0.083	0.173	0.093	0.196
	Macro volume (cm^3/g)	0.005	0.044	0.003	0.046
Average pore size (nm)		4.2	3.0	6.8	3.4

Constant current charge-discharge behavior of nitric acid functionalized SWNT membranes is not linear with time when tested in 6 M KOH, 3 M KCl aqueous solutions (Figure 6.3a) and in ionic liquids (Figure 6.3b). At a current of 1 mA, the voltage jump during discharging is very significant, especially in the mixture of BMIMBF4 and acetonitrile. This is due to high equivalent series resistance of BMIMBF4/AN.

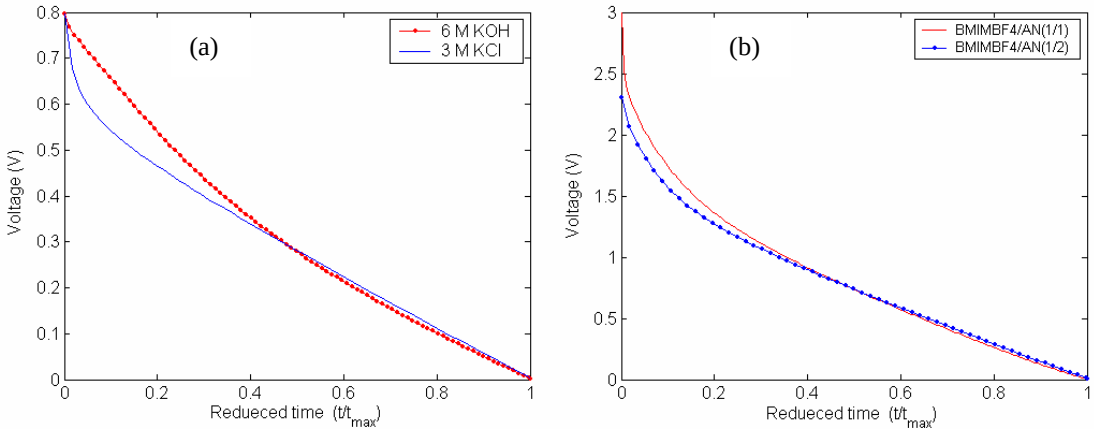

Figure 6.3. Constant current charging/discharging of nitric acid functionalized SWNT membrane (B70F) in different electrolytes. (a) 6 M KOH and 3 M KCl; (b) BMIMBF4/AN. The current is 1 mA.

Figure 6.4a compares a typical CV for nitric acid functionalized SWNT (B70F) membrane electrodes in 3 M KCl and 6 M KOH aqueous solutions at a scan rate of 50 mV/s. The difference of CV rectangular area in these two electrolytes is significant, so it is easy to draw the conclusion that nitric acid functionalized SWNT (B70F) electrodes in 6 M KOH exhibit higher capacitance than that in 3 M KCl. This difference needs further investigation. The typical CV comparison of ionic liquid

electrolyte concentration on the capacitance at a scan rate of 50 mV/s is shown in Figure 6.4b. The capacitance performance of nitric acid functionalized SWNT membrane (B70F) in diluted BMIMBF4 is much better than that in neat BMIMBF4. However, there is only minor difference in capacitance for B70F when evaluated in BMIMBF4/AN (1/1) and BMIMBF4/AN(1/2).

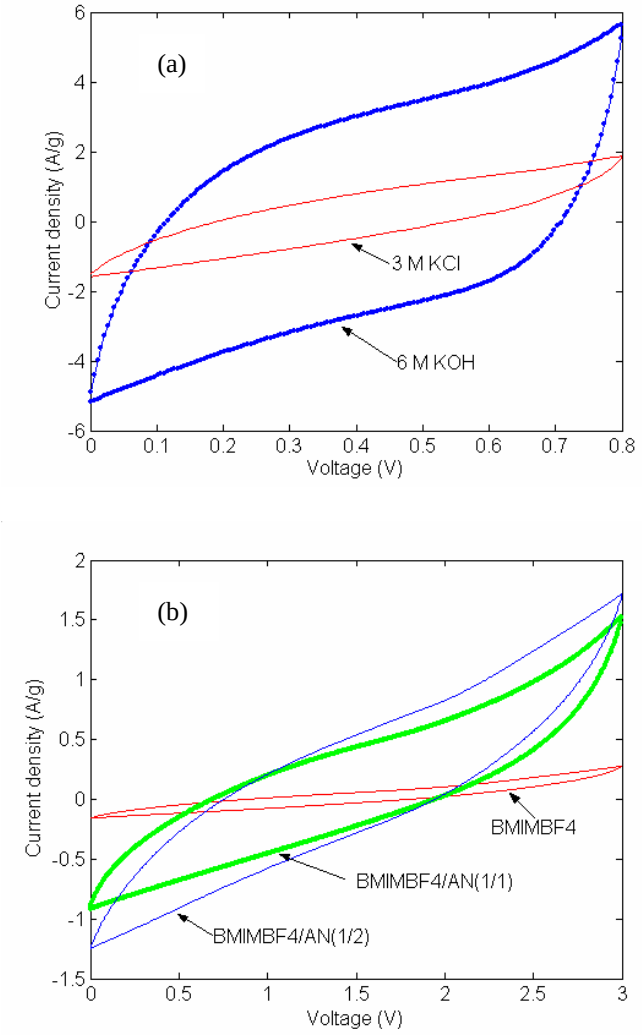

Figure 6.4. Cyclic voltammetry of nitric acid functionalized SWNT membrane (B70F) electrodes in different electrolytes. (a) 6 M KOH and 3 M KCl; (b) BMIMBF4/AN. The scan rate is 50 mV/s.

Figure 6.5a shows the specific capacitance of SWNT membrane electrodes (B70, B70H, B350, and B350H) as a function of current density in 6 M KOH. It is obvious that the bucky papers (B70, B350) have very low capacitance regardless of their thicknesses. This is due to the fact that most of the micropores are probably filled with amorphous carbon, preventing ions to access these pores. Both the heat-treated raw bucky papers show much improved capacitance with comparable values. This study suggests that electrode thickness (at least in the range of 50 to 350 μm) does not affect capacitance performance significantly. Figure 6.5b compares the capacitance of samples B70H, B70F, and B70FH as a function of current density in 6 M KOH. It is obvious that nitric acid functionalized SWNT membrane (B70F) electrode has higher capacitance than B70H and the heat-treated nitric acid functionalized sample (B70FH**)**. The higher capacitance is due to the presence of functional groups resulting from nitric acid treatment.[16] Functional groups are removed after the electrode is annealed at 650 °C for 2 hours under nitrogen.[1,17] It is observed that there is also some difference between samples B70H and B70FH, because B70FH loses functional groups during annealing. At high current density (> 8 A/g), the capacitance of sample B70H is almost two times that of sample B70FH. Due to limited sample quantity, surface area or pore size distribution of B70F and B70FH could not be measured.

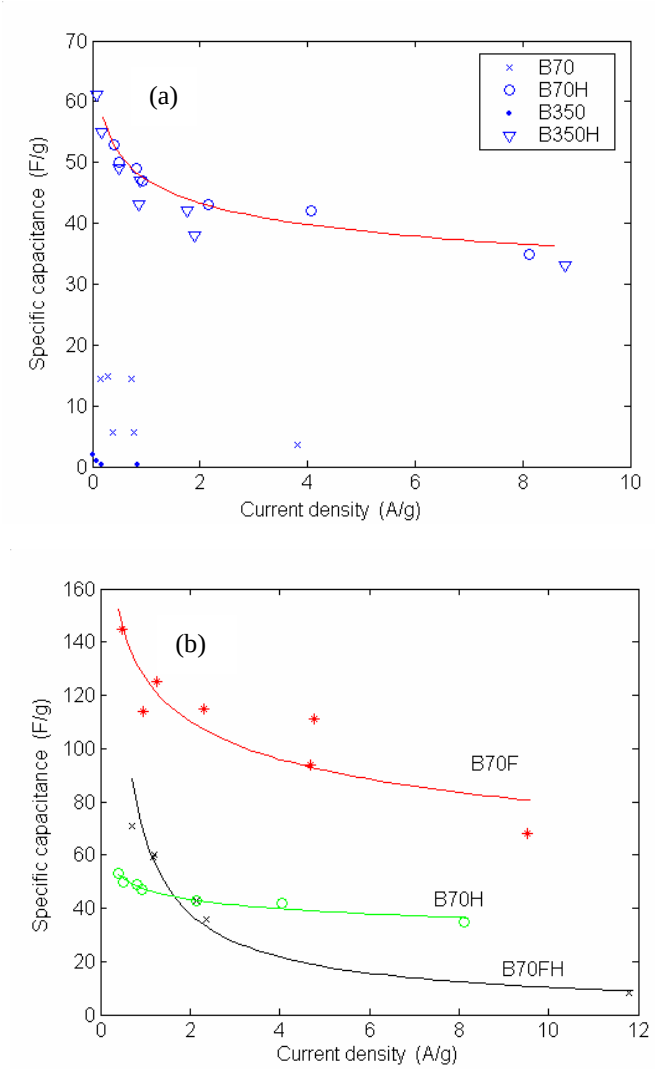

Figure 6.5. Specific capacitance of various samples as a function of current density in 6 M KOH.

Figure 6.6 shows the specific capacitance of nitric acid functionalized SWNT membrane electrodes (B70F) as a function of current density in different electrolytes. The nitric acid functionalized SWNT electrode (B70F) shows the best performance in 6 M KOH, while it shows comparable values in 3 M KCl and diluted BMIMBF4 solution. The better performance of nitric acid functionalized SWNT membrane electrode (B70F) in KOH is in contrast to the contact angle measurements. It has

higher contact angle value in 6 M KOH than that in BMIMBF4 (Table 6.3). The lower contact angle value means better affinity between the bucky papers and the electrolytes. In order to further explain the observed capacitance behavior, the electrolyte absorption test was also conducted. Nitric acid functionalized SWNT electrode (B70F) can absorb 17% BMIMBF4 by weight when submerged in it for 10 minutes, while it can absorb 109% 6 M KOH by weight in the same amount of time. This compensates for contradicting effect of its lower chemical affinity.

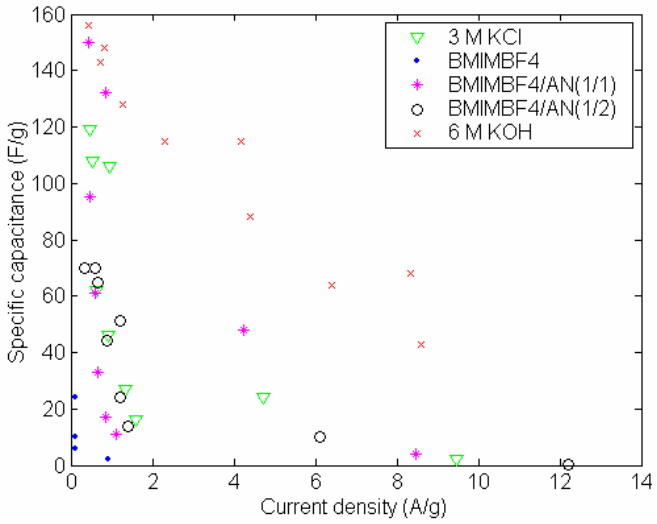

Figure 6.6. Comparison of specific capacitance of B70F as a function of current density in different electrolytes.

Table 6.3. Contact angle between nitric acid functionalized SWNT (B70F) and the electrolytes

	6 M KOH	BMIMBF4
Contact angle	119 ± 13	48 ± 2

Table 6.4. Electrolyte absorption in functionalized SWNT (B70F) electrodes

Electrolyte	Original electrode mass (mg)	Electrode mass after adsorption (mg)	Mass ratio (%)
BMIMBF4	2.48	2.91	117
6 M KOH	2.16	4.52	209

The electrochemical impedance behavior of samples B70, B70H, B70F, and B70FH in aqueous electrolyte 6 M KOH is shown in Figure 6.7. These SWNT based supercapacitors show a depressed semicircle in the high frequency region, which is indicative of a charge-transfer process.[18] At intermediate frequencies, there is a straight line with a slope of approximately 45° for B70F and B70FH, which is a common observation for activated carbon based supercapacitors.[19] The equivalent series resistances of samples B70 and B70H are lower than those of B70F and B70FH.

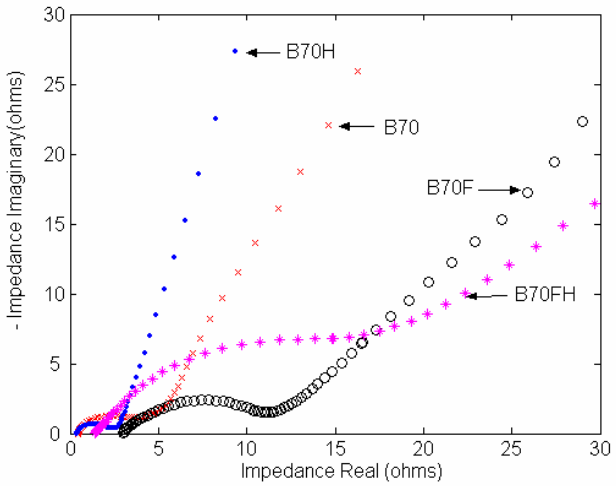

Figure 6.7. Nyquist impedance spectra of various bucky papers in 6 M KOH.

6.4 Conclusions

High capacitance was observed for nitric acid functionalized SWNT membrane over the unfunctionalized membrane. The effect of heat treatment and film thickness on the porous structure and capacitance performance was also discussed. The results show that nitric acid functionalized SWNT performs better in 6 M KOH aqueous solution than in other electrolytes. This behavior can be explained by electrolyte absorption by the electrodes. The heat treatment can change the porous structure and capacitance performance of the control SWNT and nitric acid functionalized SWNT membranes significantly.

6.5 References

1 C. M. Yang, H. Noguchi, K. Murata, M. Yudasaka, A. Hashimoto, S. Iijima, K. Kaneko. *Advanced Materials* **2005**, *17*, 866.

2 S. Agnihotri, M. Rostam-Abadi, M. J. Rood. *Carbon* **2004**, *42*, 2699.

3 C. M. Yang, D. Y. Kim, Y. H. Lee. *Journal of Nanoscience and Nanotechnology* **2005**, *5*, 970.

4 A. Anson, J. Jagiello, J. B. Parra, M. L. Sanjuan, A. M. Benito, W. K. Maser, M. T. Martinez. *J. Phys. Chem. B* **2004,** *108*, 15820.

5 L. Lafi, D. Cossement, R. Chahine. *Carbon* **2005**, *43*, 1347.

6 S. Agnihotri, J. P. B. Mota, M. Rostam-Abadi, M. J. Rood. *J. Phys. Chem. B* **2006,** *110*, 7640.

7 C. Zhou, S. Kumar, C. D. Doyle, J. M. Tour. *Chemistry of Materials* **2005**, *17*, 1997.

8 K. H. An, W. S. Kim, Y. S. Park, J. M. Moon, D. J. Bae, S. C. Lim, Y. S. Lee, Y. H. Lee. *Adv. Mater.* **2001**, *13(7)*, 497.

9 J. Li, A. Cassell, L. Delzeit, J. Han, and M. Meyyappan. *J. Phys. Chem. B* **2002,** *106*, 9299.

10 X.-F. Wang, D.-Z. Wang, D. Liang. *Acta Physico-Chimica Sinica* **2003**, *19 (6)*, 509.

11 R. H. Baughman, C. Cui, A. A. Zakhidov, Z. Iqbal, J. N. Barisci, G. M. Spinks, G. G. Wallace, A. Mazzoldi, D. De Rossi, A. G. Rinzler, O. Jaschinski, S. Roth, and M. Kertesz. *Science* **1999**, *284*, 1340.

12 A. G. Rinzler, J. Liu, H. Dai, P. Nikolaev, C. B. Huffman, F. J. Rodriguesmacias, P. J. Boul, A. H. Lu, D. Heymann, D. T. Colbert, R. S. Lee, J. E. Fisher, A. M. Rao, P. C. Eklund, and R. E. Smalley. *Appl. Phys. A* **1998**, *67*, 29.

13 P. A. Webb, C. Orr. *Analytical Methods in Fine Particle Technology*, Micromeritics Instrument Corp. **1997.**

14 Y. H. Hu, E. Ruckenstein. *Ind. Eng. Chem. Res.* **2004**, *43*, 708.

15 H. Hu, B. Zhao, M. E. Itkis, R. C. Haddon. *J. Phys. Chem. B* **2003**, *107*, 13838.

16 C. Li, D. Wang, X. Wang, J. Liang. *Carbon* **2005**, *43*, 1557-1583.

17 X. Zhang, T. V. Sreekumar, T. Liu, and S. Kumar. *J. Phys. Chem. B* **2004**, *108*, 16435.

18 S. M. Lipka. *Electrochemical Society Proceedings* **1996**, *96-25*, 244.

19 B. E. Conway. *Electrochemical Supercapacitors, Scientific Fundamental and Technological Applications;* Plenum Publishers: New York, **1999.**

CHAPTER 7

CONCLUSIONS AND RECOMMENDATIONS

7.1 Conclusions

The following conclusions can be drawn from the research work presented in this thesis:

1. Stabilization and carbonization of a ternary composite film of PAN, SAN and SWNT is an effective way to produce meso porous SWNT/carbon composites. The presence of single wall carbon nanotubes alters the PAN/SAN blend morphology. The pore size of carbonized PAN/SWNT/SAN membranes is in the 5 ~ 200 nm range, while the pore size in carbonized PAN/SAN blend film is in the range of 2 to 10 μm.
2. The specific capacitance of carbonized PAN/SWNT/SAN composite film electrodes in 6 M KOH is greater than 100 F/g. Extremely high electrical double layer capacity (205 $\mu F/cm^2$) for the carbonized PAN/SWNT/SAN has been achieved and is attributed to the presence of the surface functional groups. For comparison, the double layer capacity of activated carbon is in the range of 10 - 50 $\mu F/cm^2$. Carbonized PAN/SWNT/SAN films have lower capacitance in the ionic liquid than that in aqueous electrolytes, although they exhibit stronger affinity in ionic liquid than in 6 M KOH.
3. Pyrrole treated SWNT membranes give high specific capacitance (350 F/g) and high double layer capacity (154 $\mu F/cm^2$). Specific capacitance of pyrrole treated

SWNT membranes increased monotonically with increasing macro surface area, suggesting that macro pores (pores greater than 50 nm) play an important role for achieving high capacitance.

4. Capacitance of buckypaper and arylsulfonic acid functionalized buckypaper was 50 to 70% higher in ionic liquid than that in 6 M KOH.
5. SWNT bucky paper has higher capacitance in ionic liquid BMIMBF4 than in BMIMCl and BMIMPF6. Suitable dilution of the ionic liquid can increase the specific capacitance.
6. Heat treatment can alter the pore structure and the capacitance performance of both the unfunctionalized and nitric acid functionalized SWNT membranes significantly.

7.2 Recommendations for Future Work

Although a number of important conclusions have been reached in the course of this study, several phenomena reported here need further investigation. Some suggestions for future work are listed below:

1. The high double layer capacity of carbonized PAN/SWNT/SAN is attributed to the presence of functional groups. Carbonization at temperatures higher than the once used in this study will eliminate or reduce the presence of functional group. Therefore, one PAN/SWNT/SAN composition, for example sample PAN3-SAN30, should be chosen for carbonized it at different temperatures. Selected carbonization temperatures may be 500 °C, 700 °C, 900 °C, 1000 °C

and 1100 °C. This would allow for a systematic study on the effect of the presence of non-carbon atoms on capacitance performance. The pseudocapacitance contribution to the total capacitance will change with carbonization temperature.

2. The domain size of the sacrificial component in PAN/SWNT/SAN ternary composite film is important to the pore size control. Effect of SAN molecular weight should be explored for the pore size control.

3. Electrospinning can result in narrow pore size distribution and high surface area. Conducting polymers, such as derivatives of polythiophene, are good electrode materials for superpcapacitor, and have high decomposition voltage (> 3.0 V). These derivatives can dissolve in lower boiling point solvent, such as tetrahydrofuran and chloroform. Suitable surface area and pore size in these materials can be developed through electrospinning. Due to redox reaction in conducting polymers, pseudocapacitance contribution is very high. Electrospinning of conducting polymer/carbon nanotube suspension can combine the advantages of both high surface area and high pseudocapacitance.

APPENDIX A

STUDY OF INTERACTION BETWEEN VARIOUS CARBON NANOTUBES AND POLYMER MATRICES

A.1 Introduction

The property improvements in polymer/carbon nanotube (CNT) composites strongly depend on the homogeneous dispersion of CNTs in the polymer matrix. Two approaches have been used to improve the dispersion: covalent functionalization and use of polymers or surfactants.[1] The solution properties of single wall carbon nanotube (SWNT) were first explored by dissolving SWNT derivatized with thionychloride and octadecylamine in organic solvents.[2] Since then, many other compounds, such as organic diazonium compounds,[3] and poly(styrene-*co*-*p*-(4-(4'-vinylphenyl)-3-oxabutanol))[4] have been used to functionalize CNTs to facilitate incorporation into polystyrene (PS) matrix. The improved compatibility between PS and functionalized SWNTs results in formation of SWNT network structure for composites.[3] Since covalent functionalization of CNT may deteriorate its mechanical and electronic properties to some extent,[5,6] it is advantageous to use polymers and surfactants to accomplish dispersion through van der Waals interactions between alkyl chain of a surfactant or a polymer and the aromatic surface of the CNT.[7,8,9] It was found that the stability of SWNTs in water was enhanced by anionic surfactant sodium dodecylbenzenesulfonate (NaDDBS) by a factor of 10 to 100 compared to other commonly used surfactants, such as sodium dodecyl sulfate (SDS)

and Triton X-100. This was attributed to the presence of a benzene ring, a charged group, and an alkyl chain in NaDDBS.[8] In NaDDBS assisted dispersion, coulombic forces are overcome by the hydrophobic interactions between the surfactant tail and the nanotube walls, and hence these coulombic forces do not play a central role during adsorption of NaDDBS on SWNT.[7] However, small angle neutron scattering (SANS) suggested that there was no cylindrical micelles in aqueous dispersions of SDS, and the stabilization of the dispersion of SWNT-SDS was due to the structureless random adsorption with no preferential arrangement of the head and tail of the surfactants.[1] In addition to solution dispersion, multi wall carbon nanotube (MWNT) can also be directly dispersed uniformly in the PS matrix without significant agglomeration by melt extrusion.[10] High quality polystyrene (PS) nanocomposites were prepared by using trialkylimidazolium salt-compatibilized MWNTs via melt extrusion due to π-cation interaction between the nanotubes and imidazolium.[9] In a separate study, it was found that carbon nanotubes were densely adsorbed on the surface of the PS and poly(methyl methacrylate)(PMMA) microspheres due to the hydrophobic interactions between the surfactant molecules and the nanotube surface.[11] Not only melting process[12] but also a combination of solvent casting and melt mixing were used to disperse SWNT in PMMA.[13] Well-dispersed and aligned nanotube/PMMA films were fabricated by infiltrating pre-aligned MWNT arrays with methyl methacrylate (MMA) followed by polymerization.[14] The in-situ polymerization was induced either by heat, ultraviolet (UV) light, or ionizing (gamma) radiation.[15] A strong interface between the CNTs and the PMMA matrix has been obtained.[16]

It is well known that good interfacial bonding is necessary for successful load-transfer across the interface between CNTs and the polymer matrix.[17] 1 wt% nanotube loading in PS/MWNT composite results in 36 – 42% increase in elastic modulus and 25% increase in breaking stress, which indicates significant load transfer across the nanotube-matrix interface.[18] MWNTs were observed to bridge cracks propagating through the PS matrix, providing closure stresses across the crack.[19] Enhanced mechanical properties of polyacrylonitrile (PAN)/carbon nanotube composite fiber were also reported.[20,21] The composite with 10 wt% SWNT loading exhibits a 100% improvement in tensile modulus and 40 °C increase in glass transition temperature.[21] These property improvements in PAN/SWNT composite films were attributed to good interaction between PAN and SWNT.[22] Interfacial characteristics have been quantified with molecular dynamics simulations.[1,23,24] In the absence of bonding in polymer/CNT system, interfacial stress transfer ability strongly depends on electrostatic and van der Waals interactions.[23] It is suggested that the interfacial shear stress of polymer-CNT systems is at least one order of magnitude higher than that of the conventional microfiber-reinforced composites.[24] Van der Waals' force is the sole factor responsible for the polymer-CNT interaction, so the strength of the interfacial binding in this case depends on the geometrical conformation of the polymer with respect to the CNTs, which was confirmed by investigating the interactions between carbon materials and polymer matrix for poly(m-phenylenevinylene-co-2,5-dioctyoxy-p-phenylenevinylene) (PmPV), PS, poly(phenylacetylene) (PPA), and poly(p-phenylenevinylene) (PPV).[17]

Above studies suggest that polymers with a backbone containing aromatic rings are promising candidates for the noncovalent binding of carbon nanotubes to the polymer matrix. However, there are only a few papers in the literature dealing with the comparison of the interactions of CNTs with different polymers.[17,25] In this appendix, we present a qualitative comparison of the interactions of carbon materials (SWNT, MWNT, vapor grown carbon nanofiber (VGCNF) and activated carbon) with PS, PAN, SAN and PMMA.

A.2 Materials and Experiment

Solution of PAN (containing less than 5 % itaconic acid and methacrylate copolymer, Enichem Solution Corp) and SAN (25 wt% acrylonitrile 75 wt% styrene random copolymer, M_w = 165,000 g/mol, ACROS Organics), PS (Styron 678C-W, M_w =100,000 g/mol, Dow Chemical Co.), PMMA (M_w = 15,000 g/mol, Aldrich) in dimethylformamide (DMF, Fisher Scientific) were prepared in the desired ratios. PAN/polymer X solutions were directly cast on the glass substrate by DMF evaporation in vacuum at 85 °C, so PAN/polymer X (where X is SAN, PS or PMMA) blend film can be formed. About 40 mg of as prepared unpurified HiPCO SWNTs (about 35 wt% impurity, Carbon Nanotechnologies, Inc.) was dispersed in 25 g DMF via sonication for 24 hours in a bath sonicator (3510R-MT Sonicator, power 100 W, frequency 42 kHz, Branson). The SWNT suspension was added to the PAN/polymer X/DMF polymer solution to make a SWNT/PAN/polymer X suspension and was stirred for 2 hours. The suspension was used for film casting on a glass substrate by

DMF evaporation in vacuum at 85 °C. Similar process was also applied to MWNT (approximately 2.5% impurity, Iljin Nanotech Co., Korea), VGCNF (PR-24-HT, about 0.3% impurity, Applied Sciences Inc., OH), and activated carbon (AC, M-30 activated mesocarbon beads with a surface area of 3000 m^2/g, Spectracorp). All materials were used as received.

The composite films were heated in air to 250 °C at a heating rate of 1 °C/min and stabilized for 2 hours at that temperature, and then further heated in argon to 700 ºC at a heating rate of 5 °C/min and kept for 30 minutes during the carbonization process in a box furnace (Lindberg, 51668-HR Box Furnace 1200C, Blue M Electric). Fracture surfaces of all films were coated with gold before being examined with scanning electron microscopy (SEM) LEO 1530. The isothermal N_2 gas adsorption study was carried out on ASAP 2020 (Micromeritics Inc.) at 77 K. Thermogravimetric analysis of PAN, PMMA, PS, SAN, SWNT, MWNT, VGCNF and AC were carried out on TGA 2950 (TA Instruments, Inc.) by heating to 900 °C in nitrogen at 5 °C/min.

A.3 Results and Discussion

TGA measurements (Figure A.1a) show that SAN, PS, and PMMA burn out below 700 °C without leaving any residue, while PAN is a carbonizing polymer, and has about 40 wt% residue when carbonized to 700 °C without oxidative stabilization. Phase separation occurs in blends of PAN/PS, PAN/SAN, and PAN/PMMA. By pyrolysis of blend films of PAN/PMMA, PAN/SAN, and PAN/PS in inert

environment, pores are formed due to the decomposition of the sacrificial component (PS, PMMA, or SAN). These pores are in the 1-10 μm range (Figure A.2b, A.2c and A.2d). However, there is no porosity in PAN under the same processing conditions (Figure A.2a).

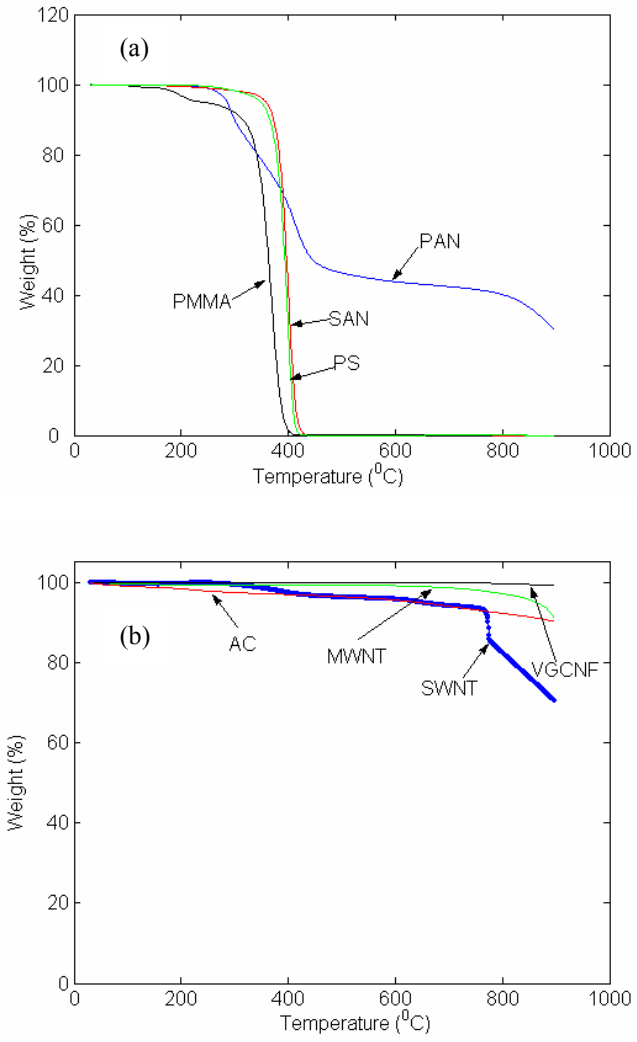

Figure A.1. Thermogravimetric analyses of (a) PAN, PMMA, PS and SAN, (b) SWNT, MWNT, VGCNF and AC when heated to 900 ºC in nitrogen at 5 °C/min.

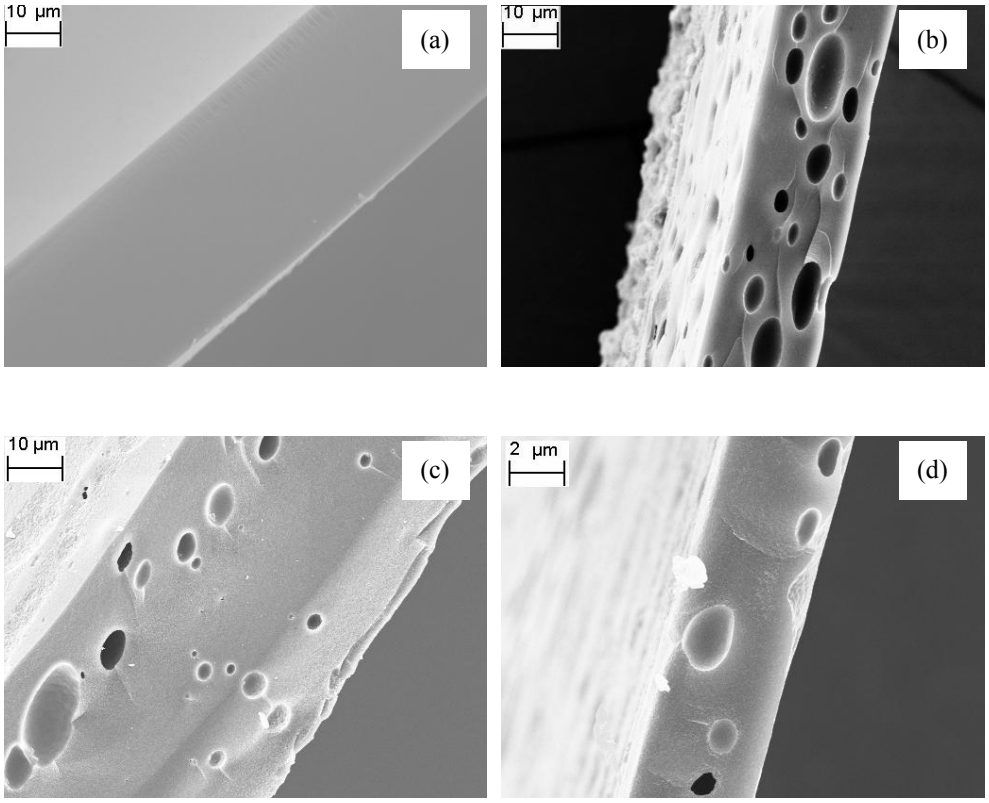

Figure A.2. Scanning electron micrographs of (a) PAN/SAN (100/0), (b) PAN/SAN (80/20), (c) PAN/PS (90/10), and (d) PAN/PMMA (90/10) blends after stabilization in air at 250 °C and carbonization in nitrogen at 700 °C.

In an inert environment, there is less than 10% weight loss for SWNT, MWNT, VGCNF and AC at 700 ºC (Figure A.1b). SEM images show that MWNT can be homogeneously dispersed in PAN matrix (Figure A.3a) as well as in PAN/PMMA (Figure A.3b) by solution casting. The pores in these ternary composites are much different from PAN/polymer X binary composite observed in Figure A.2. The pore width in carbonized PAN/MWNT/SAN film as quantified by the nitrogen gas adsorption analysis is much smaller than that in PAN/SAN film (Figure A.4 and Table A.1). This observation suggests that MWNTs act as a compatabilizer for PAN/PMMA. However, MWNTs are observed to aggregate together in SAN and PS

domains in PAN/SAN/MWNT and PAN/PS/MWNT ternary composites, respectively (Figure A.3c and A.3d). This suggests that MWNTs have better interaction with SAN and PS than with PAN matrix and PMMA.

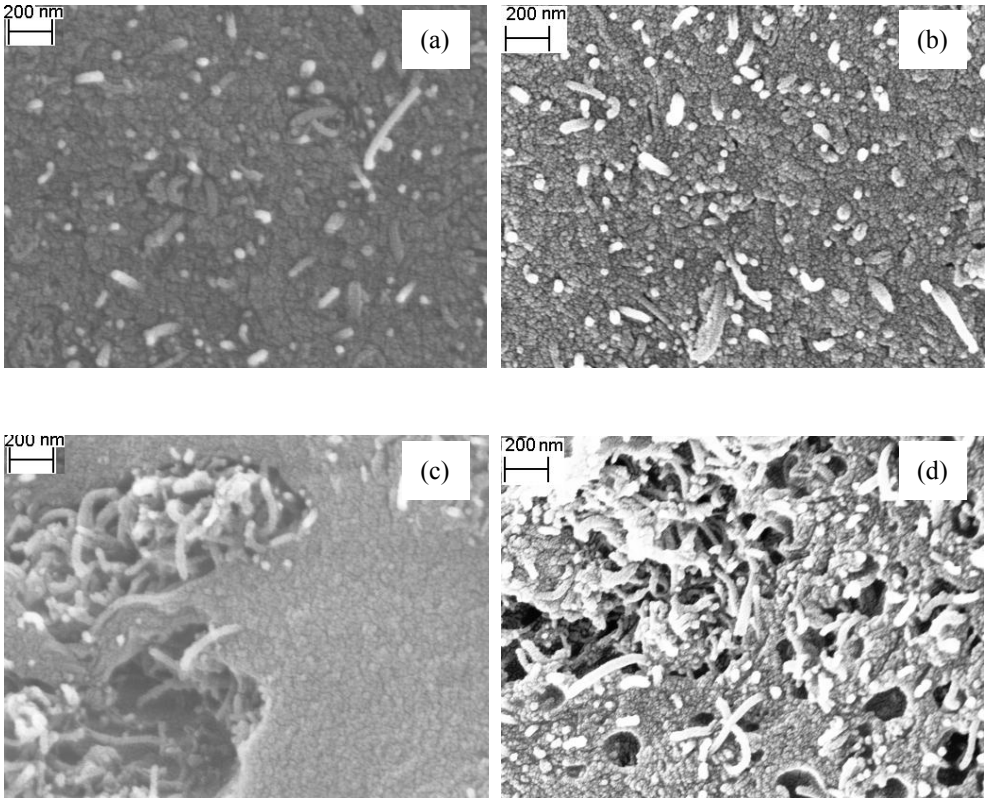

Figure A.3. Scanning electron micrographs of PAN/MWNT/polymer X composites. (a) PAN/MWNT(90/10), (b) PAN/MWNT/PMMA (90/10/10), (c) PAN/MWNT/SAN (90/10/20), and (d) PAN/MWNT/PS (90/10/10) after stabilization in air at 250 °C and carbonization in nitrogen at 700 °C.

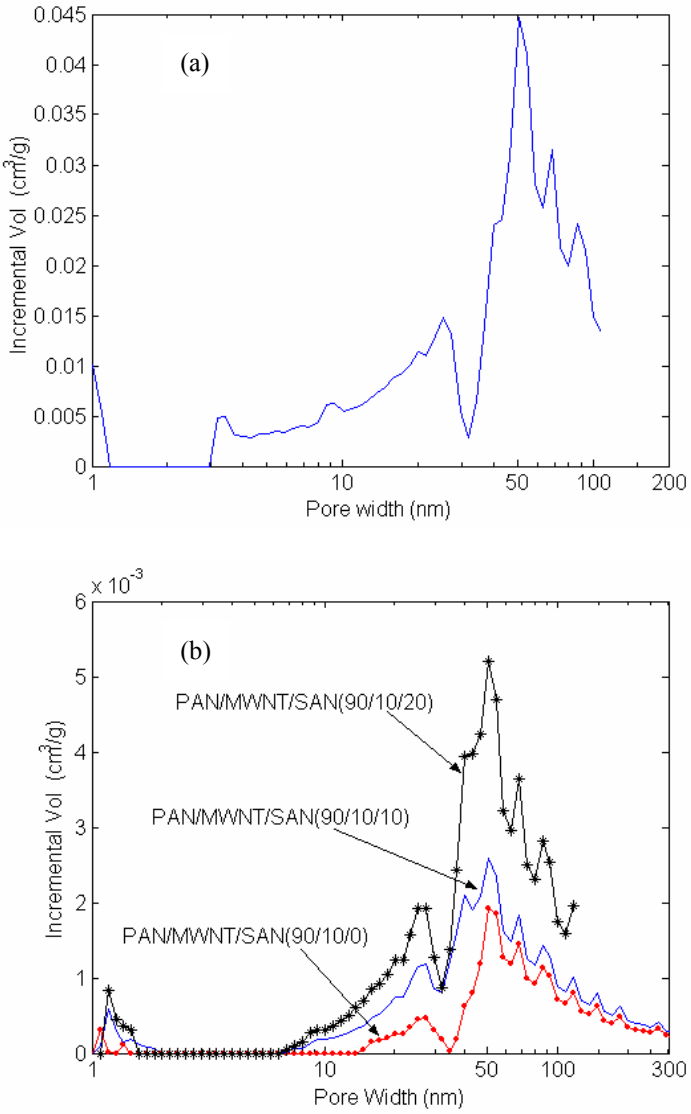

Figure A.4. Pore size distribution in (a) MWNT powder, (b) carbonized PAN/MWNT/SAN films.

Table A.1. Pore volume, pore size and surface area of MWNT and carbonized PAN/MWNT/SAN films

	BET surface area (m^2/g)	**Pore volume (cm^3/g)**	**Pore width (nm)**
PAN/MWNT/SAN (90/10/0)	3	0.03	34
PAN/MWNT/SAN (90/10/10)	8	0.05	24
PAN/MWNT/SAN (90/10/20)	13	0.08	23
MWNT powder	161	0.71	18

Morphological features similar to Figure A.3 are observed in PAN/VGCNF/polymer X composites (Figure A.5). VGCNF shows good dispersion in PAN and PAN/PMMA (Figure A.5a and A.5b), while VGCNF aggregates are observed in PAN/PS and PAN/SAN (Figure A.5c and A.5d). This suggests that VGCNF has better interaction with SAN and PS than with PAN and PMMA matrices.

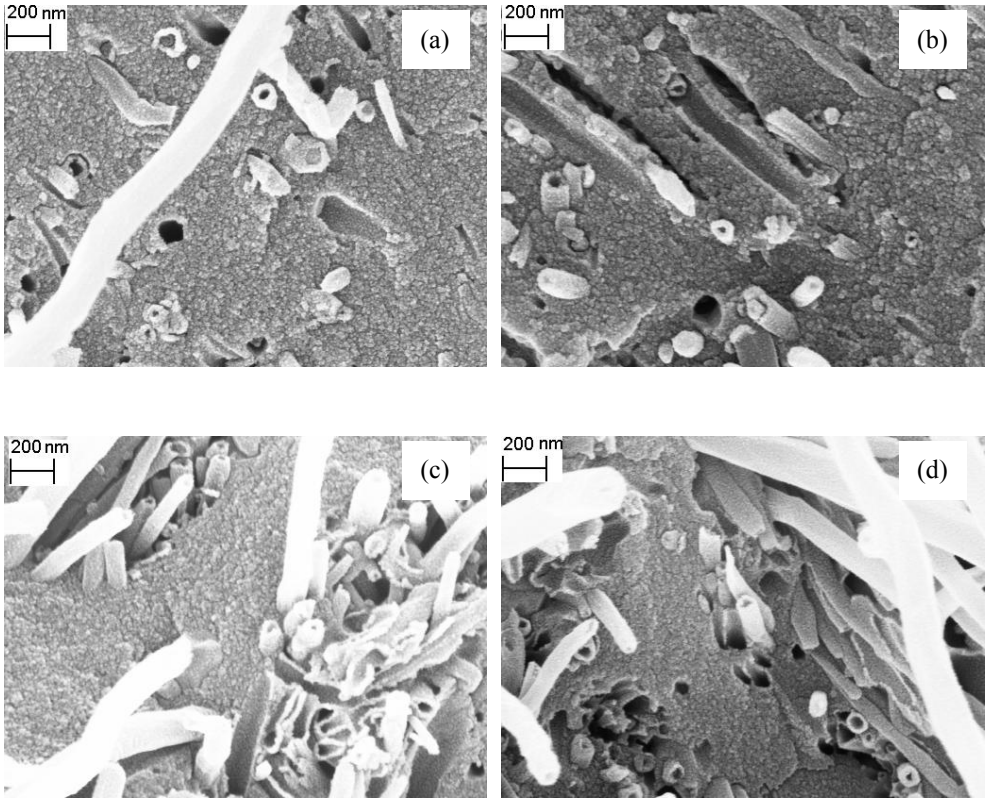

Figure A.5. Scanning electron micrographs of PAN/VGCNF/polymer X composites. (a) PAN/VGCNF (90/10), (b)PAN/VGCNF/PMMA(90/10/10), (c) PAN/VGCNF/PS (90/10/10), and (d) PAN/VGCNF/SAN (90/10/10) after stabilization in air at 250 °C and carbonization in nitrogen at 700 °C.

AC shows good dispersion in PAN (Figure A.6a), while AC aggregates are observed in PAN/SAN (Figure A.6b). This suggests that AC has better interaction with SAN than with PAN matrix. However, SWNTs are uniformly dispersed in PAN, PAN/SAN, PAN/PS and PAN/PMMA as shown in Figure A.7.

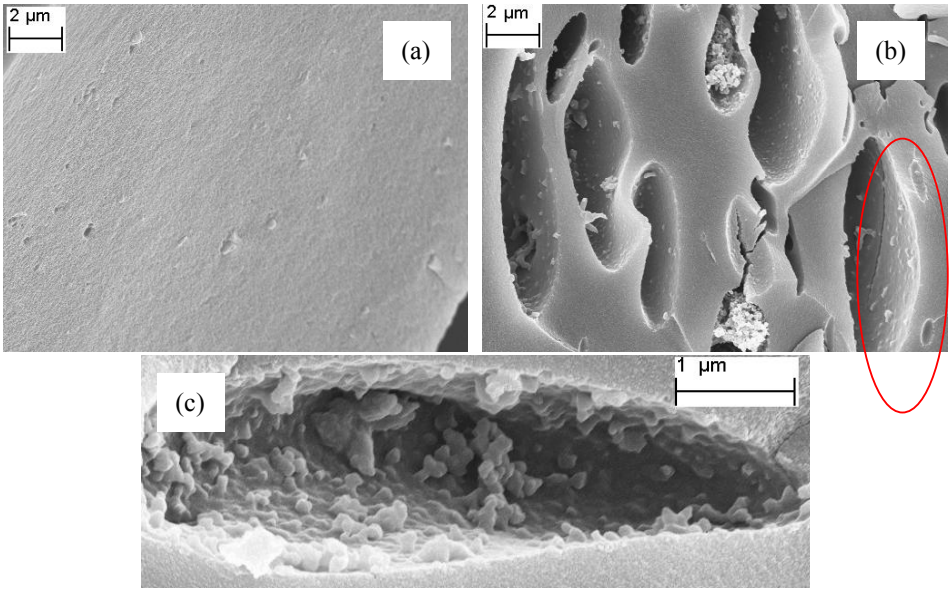

Figure A.6. Scanning electron micrographs of PAN/activated carbon/SAN composites. (a) PAN/AC (90/10); (b) PAN/AC/SAN (90/10/10), and (c) magnified image of (b) after stabilization in air at 250 °C and carbonization in nitrogen at 700 °C.

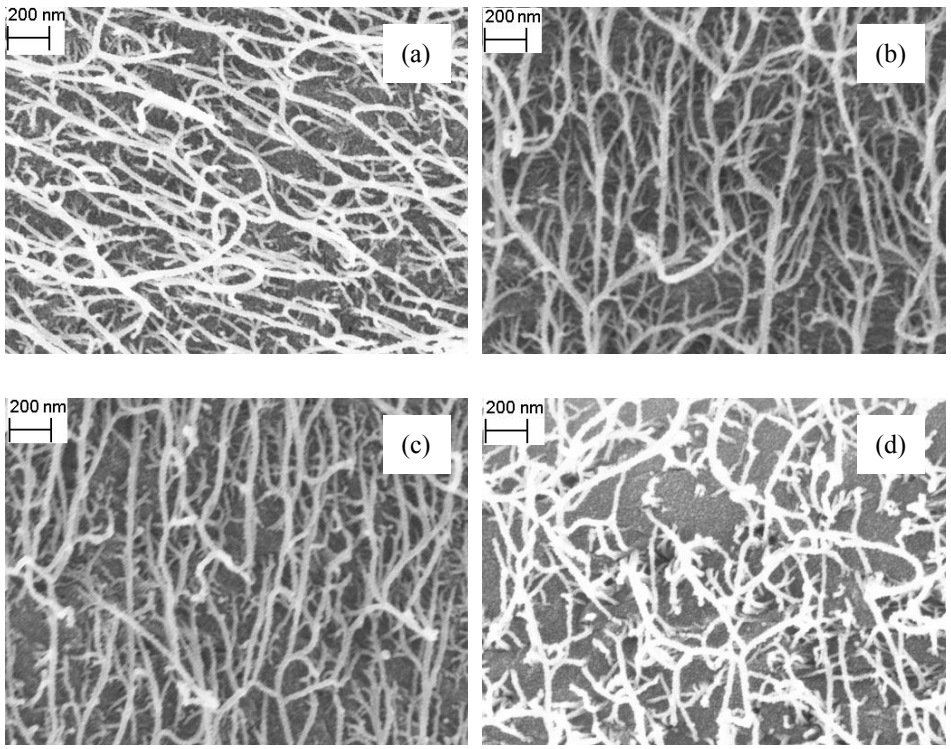

Figure A.7. Scanning electron micrographs of PAN/SWNT/polymer X composites. (a) PAN/SWNT (90/10), (b) PAN/SWNT/PS (90/10/10), (c) PAN/SWNT/PMMA (90/10/10), and (d) PAN/SWNT /SAN (80/10/10) after stabilization in air at 250 °C and carbonization in nitrogen at 700 °C.

All these observations show that MWNT, VGCNF and AC have better interaction with SAN and PS than with PAN and PMMA, which can be explained as follows. MWNT, VGCNF, AC and SWNT consist of mainly sp^2 bonded carbon atoms,[26] although sp^3 orbital hybridization happens due to curvature of the small diameter SWNTs.[27,28] The carbon atoms in the benzene rings in SAN and PS also have a kind of sp^2 structure. It is revealed that atomic arrangement of carbon atoms in aromatic rings is isomorphic to the hexagonal arrangement in graphitic sheets.[17] Therefore, it is easy for SAN and PS to form π-π stacking structure with MWNT, VGCNF, AC, and SWNT. Therefore aromatic rings are expected to play an important role in providing effective adhesion with the surface of the CNTs.[17] The interaction between PS (SAN) and MWNT (VGCNF, AC) are strong enough to keep them together. While in PAN and PMMA, there is no sp^2 structure, so MWNT, VGCNF, AC and SWNT can disperse evenly without a π-π stacking structure. Molecular dynamics simulations show that intermolecular interaction between PS and SWNTs monotonically increases toward an asymptotic value given by the interaction of PS with a flat graphitic surface as the diameter of nanotube increases.[17] It is obvious that the diameters of MWNT, VGCNF and AC are much bigger than that of SWNT, so SWNT has a weaker interaction toward PS and SAN than MWNT, VGCNF and AC. Furthermore the curvature of the graphitic sheets constituting the CNTs diminishes polymer adhesion.[17] The effect of curvature of SWNT on interaction between polymer/CNTs is probably bigger than that of π-π stacking structure due to its biggest curvature among these carbon materials. Therefore, no

SWNT aggregations in PAN/PS and PAN/SAN are observed.

A.4 Conclusions

SWNT, MWNT, VGCNF, and activated carbon can be dispersed homogeneously in PAN and PAN/PMMA blends. However, MWNT, VGCNF, and activated carbon aggregation is observed in PAN/PS, and PAN/SAN matrix, while SWNTs were uniformly dispersed. This observation indicates that MWNT, VGCNF, and activated carbon have stronger interaction with SAN and PS than with PAN and PMMA.

A.5 References

1 K. Yurekli, C. A. Mitchell, R. Krishnamoorti. *Journal of the American Chemical Society* **2004**, *126 (32)*, 9902-9903.

2 J. Chen, M. A. Hamon, H. Hu, Y. S. Chen, A. M. Rao, P. C. Eklund, R. C. Haddon. *Science* **1998**, *282 (5386)*, 95-98.

3 C. A. Mitchell, J. L. Bahr, S. Arepalli, J. M. Tour, R. Krishnamoorti. *Macromolecules* **2002**, *35 (23)*, 8825-8830.

4 D. E. Hill, Y. Lin, A. M. Rao, L. F. Allard, Y. P. Sun. *Macromolecules* **2002**, *35 (25)*, 9466-9471.

5 A. Garg, S. B. Sinnott. *Chemical Physics Letters* **1998**, *295*, 273-278.

6 S. Shenogin, A. Bodapati, L. Xue, R. Ozisik, P. Keblinski. *Applied Physics Letters* **2004**, *85*, 2229-2231.

7 O. Matarredona, H. Rhoads, Z. R. Li, J. H. Harwell, L. Balzano, D. E. Resasco. *Journal of Physical Chemistry B* **2003**, *107 (48)*, 13357-13367.

8 M. F. Islam, E. Rojas, D. M. Bergey, A. T. Johnson, A. G. Yodh. *Nano Letters* **2003**, *3 (2)*, 269-273.

9 S. Bellayer, J. W. Gilman, N. Eidelman, S. Bourbigot, X. Flambard, D. M. Fox, H. C. De Long, P. C. Trulove. *Advanced Functional Materials* **2005**, *15(6)*, 910-916.

10 Y. J. Choi, S. H. Hwang, Y. S. Hong, J. Y. Kim, C. Y. Ok, W. Huh, S. W. Lee. *Polymer Bulletin* **2005**, *53 (5-6)*, 393-400.

11 H. J. Jin, H. J. Choi, S. H. Yoon, S. J. Myung, S. E. Shim. *Chemistry of Materials* **2005**, *17(16)*, 4034-4037.

12 Z. Jin, K. P. Pramoda, G. Xu, S. H. Goh. *Chemical Physics Letters* **2001**, *337 (1-3)*, 43-47.

13 R. Haggenmueller, H. H. Gommans, A. G. Rinzler, J. E. Fischer, K. I. Winey. *Chemical Physics Letters* **2000**, *330(3-4)*, 219-225.

14 N. R. Raravikar, L. S. Schadler, A.Vijayaraghavan, Y. P. Zhao, B. Q. Wei, P. M.

Ajayan. *Chemistry of Materials* **2005**, *17 (5)*, 974-983.

15 L. M. Clayton, A. K. Sikder, A. Kumar, M. Cinke, M. Meyyappan, T. G. Gerasimov, J. P. Harmon. *Advanced Functional Materials* **2005**, *15 (1)*, 101-106.

16 Z. J. Jia, Z. Y. Wang, C. L. Xu, J. Liang, B. Q. Wei, D. H. Wu, S. W. Zhu. *Materials Science and Engineering A* **1999**, *271 (1-2)*, 395-400.

17 M. Yang, V. Koutsos, M. Zaiser. *Journal of Physical Chemistry B* **2005**, *109 (20)*, 10009-10014.

18 D. Qian, E. C. Dickey, R. Andrews, T. Rantell. *Applied Physics Letters* **2000**, *76(20)*, 2868-2870.

19 D. Qian, E. C. Dickey. *Journal of Microscopy-Oxford* **2001**, *204*, 39-45.

20 M. C. Weisenberger, E. A. Grulke, D. Jacques, T. Rantell, R. Andrews. *Journal of Nanoscience and Nanotechnology* **2003**, *3 (6)*, 535-539.

21 T. V. Sreekumar, T. Liu, B. G. Min, H. Guo, S. Kumar, R. H. Hauge, R. E. Smalley. *Advanced Materials* **2004**, *16 (1)*, 58.

22 H. Guo, T. V. Sreekumar, T. Liu, M. Minus, S. Kumar. *Polymer* **2005**, *46 (9)*, 3001-3005.

23 K. Liao, S. Li. *Applied Physics Letters* **2001**, *79 (25)*, 4225-4227.

24 M. Wong, M. Paramsothy, X. J. Xu, Y. Ren, S. Li, K. Liao. *Polymer* **2003**, *44 (25)*, 7757-7764.

25 D. W. Steuerman, A. Star, R. Narizzano, H. Choi, R.S. Ries, C. Nicolini, J. F. Stoddart, J. R. Heath. *Journal of Physical Chemistry B* **2002**, *106*, 3124.

26 T. D. Burchell. *Carbon Materials for Advanced Technologies*, Pergamon **1999**, p14.

27 X. Blasé, L. X. Benedict, E. L. Shirley, S. G. Louie. *Physical Review Letters* **1994**, *72*, 1878-1881.

28 A. Kleiner, S. Eggert. *Physical Review B* **2001**, *64*, 113402-113405.

APPENDIX B

STRUCTURAL CHARACTERIZATION OF CARBON NANOTUBE BASED ELECTRODES BY WIDE ANGLE X-RAY DIFFRACTION (WAXD)

B.1 Introduction

High surface area is very important to obtain high capacitance. However, based on our results in the previous chapters, the electrical double layer capacities are much different and strongly depend on the electrode preparation methods and precursors. Hence high double layer capacities and high surface area are very necessary to obtain high capacitance performance. It is said that the double layer capacity of carbon materials is proportional to the ratio of edge orientation to basal orientation, which can be determined from the crystal size. [1] In this appendix, the electrode material is characterized with wide angle X-ray diffraction (WAXD). The crystal size of the basal and edge plane has been determined. The relationship between the ratio of basal to edge plane and capacity of the electrode is discussed.

B.2 Materials and Experiment

The preparation methods and properties of all materials used here have been discussed in previous chapters. X-ray diffraction studies on the electrodes were done on Rigaku R-AXIS IV2+ equipped with an image plate. The data analysis was done by using Jade software.

B.3 Results and Discussion

Various carbon nanotube electrodes discussed and presented in this thesis were characterized by WAXD using Cu Kα (wavelength 0.154 nm) radiation. WAXD plots are given in Figure B.1, and the observed d-spacing and crystal size determined using Scherrer equation[2] are listed in Table B.1. d-spacings in the 0.6 to 0.8 nm range are due to SWNT lattice, while the 0.35 to 0.38 nm values are most likely the interplanar tubostratic carbon spacing. d_{100} graphite spacing is observed at 0.213 nm. The presence of 7.5 nm crystal width perpendicular to the graphite plane in the bucky paper suggests the presence of turbostratic carbon in this sample. Crystal width perpendicular to this plane in all other samples was less than 2 nm. SWNT spacing (0.6 to 0.8 nm) was not observed in PAN/SWNT/SAN samples, as the SWNT content in all these samples was rather low. Crystal size perpendicular to the SWNT pacing (0.6 to 0.8 nm) in various functionalized tubes was in the range of 2 to 4 nm, except for sample CDD-I-59, where crystal size was only about 1 nm. This suggests that sample CDD-I-59 may be highly exfoliated. There was no correlation between the WAXD data and the capacitance performance. The purpose of this appendix is to document the WAXD results of these various electrode materials.

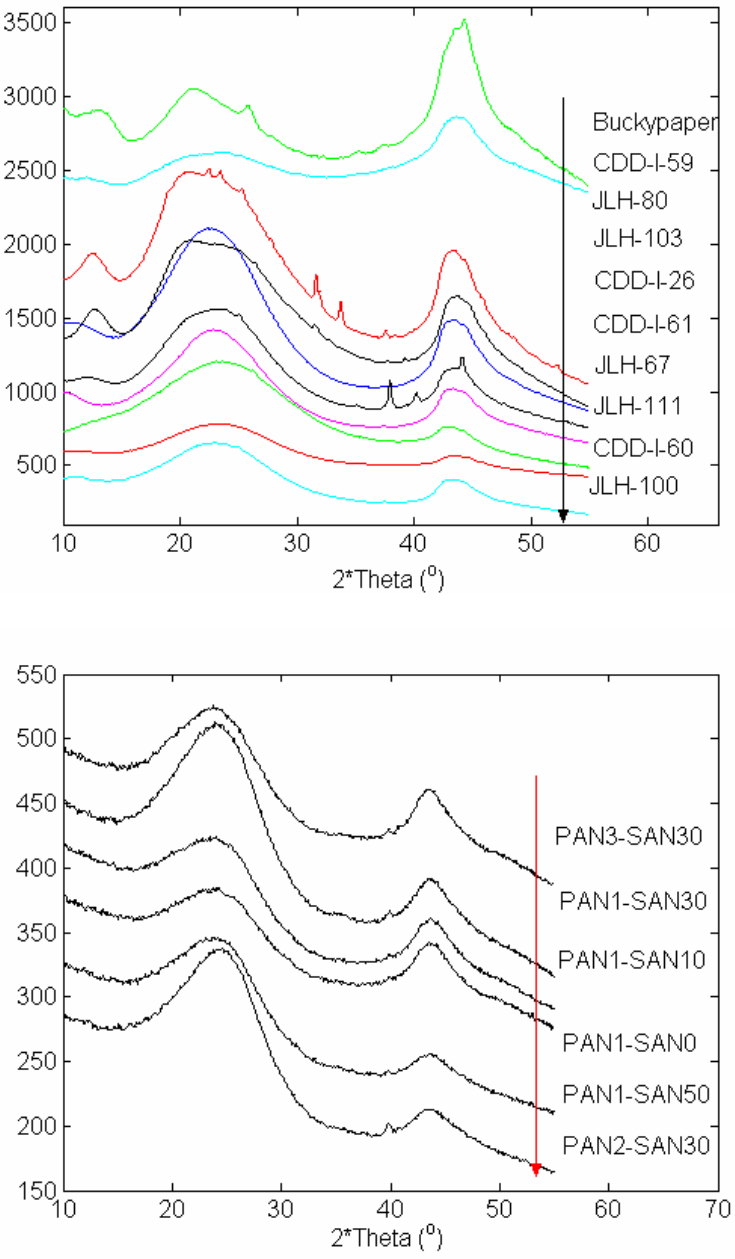

Figure B.1. X-ray diffraction profiles of different carbon materials. The definitions of these materials can be found in the context of previous chapters.

Table B.1. Bragg angle, d-spacing, FWHM and crystal size of various carbon materials

Bucky paper				**JLH-II-67**			
2θ(°)	d(Å)	FWHM(°)	L(Å)	2θ(°)	d(Å)	FWHM(°)	L(Å)
13.3	6.7	6.2	13.0	10.4	8.5	2.8	28.3
21.3	4.2	6.4	12.6	22.9	3.9	9.1	8.9
25.8	3.5	1.1	74.7	23.4	3.8	4.5	18.2
43.9	2.1	4.5	18.9	43.2	2.1	4.7	18.2
48.8	1.9	5.4	16.2	49.0	1.9	3.8	22.9
JLH-II-72				**JLH-II-80**			
12.3	7.2	3.1	25.5	12.6	7.0	2.2	36.3
21.5	4.1	10.2	7.9	20.8	4.3	9.0	8.9
23.9	3.7	5.1	15.8	25.3	3.5	6.8	11.9
43.2	2.1	3.3	25.7	43.1	2.1	4.7	18.3
45.1	2.0	10.2	8.4				
JLH-II-100				**JLH-II-103**			
11.3	7.8	2.3	35.1	12.7	7.0	2.3	34.8
23.3	3.8	9.5	8.6	19.8	4.5	3.6	22.6
43.1	2.1	4.5	19.1	23.5	3.8	9.4	8.6
				43.5	2.1	4.5	18.8
				49.2	1.9	4.0	22.0

* L is the crystal size, θ is the Bragg angle, d is d-spacing, and FWHM is the full width at half maximum.

Table B.1. (continued)

JLH-II-111				**CDD-I-26**			
2θ(°)	d(Å)	FWHM(°)	L(Å)	2θ(°)	d(Å)	FWHM(°)	L(Å)
13.3	6.7	7.7	10.4	11.4	7.8	2.4	33.7
18.5	4.8	5.9	13.7	20.9	4.3	7.1	11.4
23.8	3.7	10.5	7.7	23.8	3.7	8.5	9.6
43.2	2.1	4.0	21.1	43.2	2.1	4.1	20.6
				47.8	1.9	10.0	8.7
CDD-I-59				**CDD-I-60**			
11.5	7.7	8.4	9.5	19.8	4.5	5.5	14.7
19.7	4.5	6.2	13.1	24.1	3.7	7.8	10.4
23.9	3.7	7.9	10.3	43.5	2.1	4.4	19.5
43.7	2.1	5.4	16.0				
49.7	1.8	4.7	18.6				
CDD-I-61				**PAN1-SAN0**			
12.3	7.2	2.5	32.5	24.6	3.6	8.1	10.0
19.7	4.5	3.5	22.8	43.7	2.1	4.5	19.2
3.4	3.8	8.7	9.3	49.8	1.8	10.4	8.5
43.8	2.1	3.7	23.3				
47.3	1.9	7.9	11.0				

Table B.1. (continued)

PAN1-SAN10				**PAN2-SAN30**			
2θ(°)	d(Å)	FWHM(°)	L(Å)	2θ(°)	d(Å)	FWHM(°)	L(Å)
24.7	3.6	8.9	9.1	25.1	3.5	8.7	9.4
43.7	2.1	4.9	17.4	44.2	2.0	5.3	16.3
49.8	1.8	10.1	8.7	47.8	1.9	5.9	14.8
PAN3-SAN30				**PAN1-SAN50**			
24.4	3.7	8.4	9.7	24.6	3.6	8.6	9.4
43.5	2.1	5.2	16.5	43.5	2.1	4.8	17.8
51.0	1.8	6.5	13.5	48.0	1.9	10.9	8.0
PAN1-SAN30							
24.7	3.6	8.6	9.5				
43.7	2.1	5.5	15.5				
50.8	1.8	7.3	12.1				

B.4 References

1 D. Qu. *Journal of Power Sources* **2002**, *109*, 403.

2 B. D. Cullity. *Elements of X-ray Diffraction* (2nd edition), Addison-Wesley Publishing Company, **1978**.

APPENDIX C
CHARACTERIZATION OF ELECTROLYTE CONDUCTIVITY

C.1 Introduction

In most cases, the capacitance performance of supercapacitors is strongly dependent on the electrode/electrolyte interface. [1] Aqueous solution and non-aqueous solution electrolytes have different limitations.[1, 2] Generally a supercapacitor in a non-aqueous electrolyte can have higher energy density than in aqueous electrolyte because non-aqueous electrolyte has a larger voltage window.[3] However, non-aqueous electrolyte has higher ionic resistance as compared to the aqueous electrolyte, resulting in lower power density.[1,3] It is necessary to find an electrolyte with high voltage window and high conductivity. Therefore in this appendix, the conductivities of 6 M KOH aqueous solution and 1-butyl-3-methyl-imidazolium tetrafluoroborate (BMIMBF4) ionic liquid are investigated.

C.2 Materials and Experiment

6 M KOH aqueous solution and ionic liquid BMIMBF4 (Merck) were used as electrolyte in previous chapters. The conductivity test of the 6 M KOH aqueous solution and BMIMBF4/acetonitrile was carried out in a testing cell using a Keithley 220 current source. The electrolyte is held in the testing cell and current values from 2 μA to 10 μA are applied. The distance between the positive and negative

electrodes is about 1 mm. Once the voltage value is read at a given current, then the positive and negative electrodes are switched. The electrolytes were tested at the same current after switching the electrodes. This procedure has been repeated several times.

C.3 Results and Discussion

The voltage is plotted as a function of current for 6 M KOH aqueous solution in Figure C.1. The resistance values of 6 M KOH aqueous solution can be determined from the slopes of these plots and are listed in Table C.1. After switching the positive and negative electrodes, there is only about less than 30% difference in resistance values between before and after switching the positive and negative electrodes.

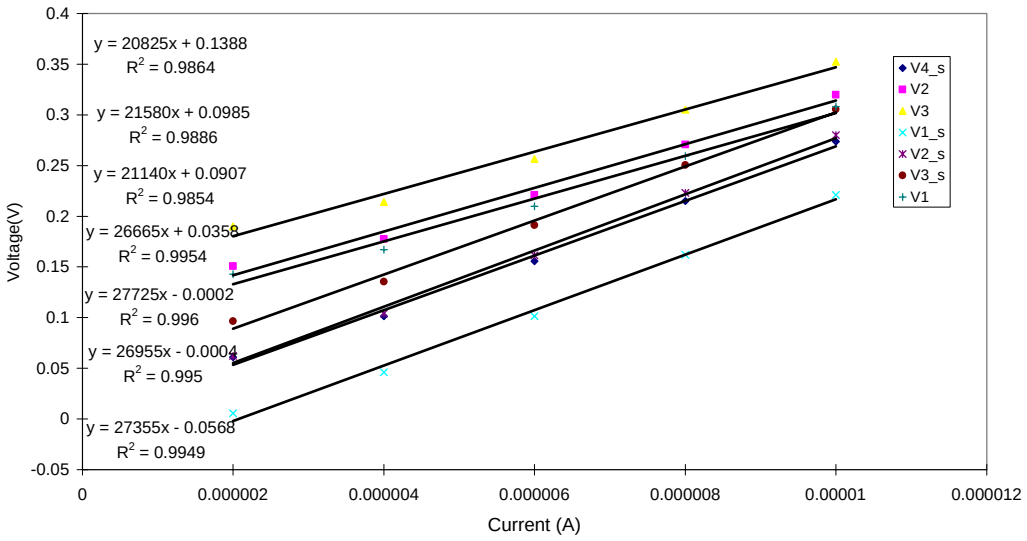

Figure C.1. Plots of voltage as a function of current for 6 M KOH aqueous solution.

Table C.1. The given currents and resulting voltages for 6 M KOH aqueous solution

	V1 (V)	V2 (V)	V3 (V)	V1_s (V)	V2_s (V)	V3_s (V)	V4_s (V)
Resistance (Ω)	21140	21580	20825	27355	27725	26665	26955

The voltage plot as a function of current for BMIMBF4/acetonitrile (3/1) is shown in Figure C.2, and the resistance values are given in Table C.2. After switching the positive and negative electrodes, there are about 3 times differences in resistance values between before and after switching the positive and negative electrodes.

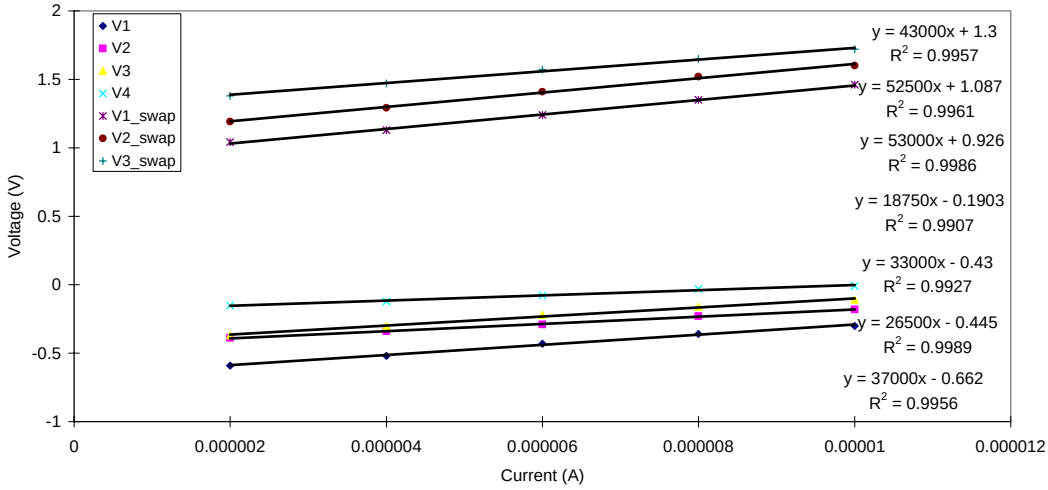

Figure C.2. Plots of voltage as a function of current for BMIMBF4/acetonitrile (3/1).

Table C.2. The given currents and resulting voltages for BMIMBF4/acetonitrile (3/1)

	V1 (V)	V2 (V)	V3 (V)	V4 (V)	V1_s (V)	V2_s (V)	V3_s (V)
Resistance (Ω)	37000	26500	33000	18750	53000	52500	43000

These observations show that there is a significant change in resistance for BMIMBF4/acetonitrile (3/1), when the electrodes are switched, such a drastic change is not observed for 6 M KOH aqueous solution. This behavior can be explained as follows. The two electrodes are made of stainless steel sheet which is immersed in the electrolyte. When applying a current source to 6 M KOH electrolyte to measure its resistance, a circuit is formed, which includes two double layers and a resistor. The two double layers and the resistor are connected in series. After the potential is off, the double layer disappears immediately due to low viscosity of 6 M KOH, thus there is no big difference after switching the negative and positive electrodes. While for BMIMBF4/acetonitrile, when the potential is off, the double layer will also relax back to its initial state. However, the relaxation process is very slow due to high viscosity of BMIMBF4/acetonitrile. Hence these two double layers still exist even after switching the negative and positive electrodes. The resistance of the circuit (two double layers and one resistor) supposed to be infinity for direct current source. However, this is not ideal double layer capacitor, because it relaxes along with time. That is why negative voltage values were observed after switching the electrodes. And these resistance values are not constant along with time. Using alternating current (AC) may be a better way to measure the resistance of these ionic liquids.

C.4 References

1 B. E. Conway. *Electrochemical Supercapacitors, Scientific Fundamental and Technological Applications*, Plenum Publishers, **1999**.

2 A. J. Bard, L. R. Faukner. *Electrochemical Methods: Fundamentals and Applications* (2^{nd} edition). John Wiley & Sons, Inc. **2001**.

3 F. Lufrano, P. Staiti. *Electrochemical and Solid –State Letters* **2004**, *7(11)*, A447.